

# Chapter 1

## 2D Carbon-Based Nanoelectronics

**Abstract** This chapter is dealing with the physics and applications of graphene in nanoelectronics, sensors and optoelectronics. Therefore, the physical properties of graphene presented in this chapter, as well as the specific phenomena encountered in this material, are directly linked to the electronic or optoelectronic devices.

### 1.1 Physical Properties of 2D Carbon-Based Materials

More than 10 years after the discovery of graphene (Novoselov et al. 2004), which is a single sheet of carbon atoms with a thickness of 0.34 nm arranged into a hexagonal structure, the main physical phenomena in this material seem to be well understood, although some debates are still present even today.

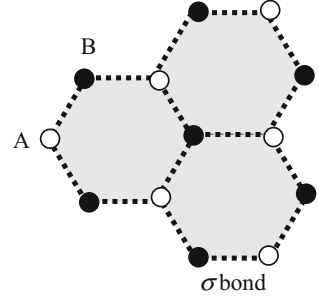
Graphene distinguishes itself by its uncommon physical properties, which are at the origin of unprecedented mechanical or electrical physical parameters that surpass similar characteristics of any other materials, including semiconductors. Why? The answer to this question is the subject of this section.

Graphene is formed from carbon atoms in the  $sp^2$  hybridization state, each atom being covalently bonded to three others. Thus, graphene crystallizes in a honeycomb lattice consisting of two interpenetrated triangular sublattices, which can be visualised in Fig. 1.1. In this figure, one triangular sublattice is formed by “white” carbon atoms denoted by A, while the other consists of “black” carbon atoms denoted by B. Needless to say, the “white” and “black” carbon atoms in Fig. 1.1 are identical, the labels A and B being introduced only for visualisation purposes and for understanding the sublattices’ interplay.

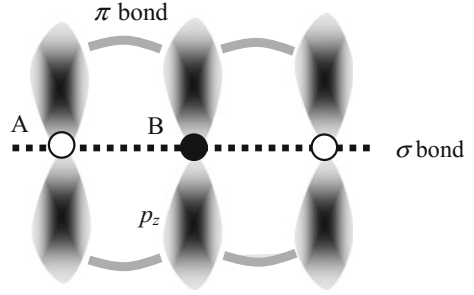
Graphene is at the origin of other carbon-based materials. For instance, graphite is formed from many graphene monolayers stacked as a pile, while carbon buckyballs are produced when graphene is wrapped as a sphere. On the other hand, when rolled-up, graphene forms the carbon nanotube, which is a key material for nanoelectronic devices working from few hundred of megahertz up to X rays.

Figure 1.2, which represents a side-view of the orbitals in graphene, tells us a lot about the physical properties of this material. The strong and rigid  $\sigma$  bonds resulted

**Fig. 1.1** Atomic honeycomb structure of graphene and its interpenetrated triangular sublattices



**Fig. 1.2** The conduction in graphene via hybridization of  $p_z$  atomic orbitals



from the hybridization of the nearest planar  $sp^2$  hybrid orbitals in graphene, are the source of the extraordinary strength and flexibility of this material, characterized by an exceptionally high breaking strength and Young modulus (Lee et al. 2008). However, the  $\sigma$  bonds are localized, and thus there are no free electrons to participate at conduction. The conduction properties of graphene are dictated only by the  $\pi$  and  $\pi^*$  bonds produced via hybridization of the remaining  $p_z$  atomic orbitals of nearest carbon atoms, denoted by A and B, as in Fig. 1.1.

Because each of the two interpenetrating triangular sublattices of the honeycomb lattice contributes to the wavefunction of charge carriers in graphene, the wavefunction is in this case a spinor rather than a scalar, as in common semiconductor materials.

The tight-binding approximation, considering only interactions between nearest neighbors, gives an energy dispersion relation of the form (Castro-Neto et al. 2009):

$$E(\mathbf{k}) = \pm t \sqrt{3 + 2 \cos(\sqrt{3}k_y a) + 4 \cos(\sqrt{3}k_y a/2) \cos(3k_x a/2)} \quad (1.1)$$

where  $a = 0.142$  nm represents the distance between two C atoms and  $t = 2.75$  eV is the nearest-neighbor hopping energy. A rigorous deduction of (1.1) starting from the tight-binding Hamiltonian is found in (Katsnelson 2012). The plus and minus signs in (1.1) refer to the upper ( $\pi^*$ ) and lower ( $\pi$ ) energy bands, the charge carriers in these bands being considered as electron and hole states. The dispersion relation of graphene is depicted in Fig. 1.3. From this figure it can be seen that at the

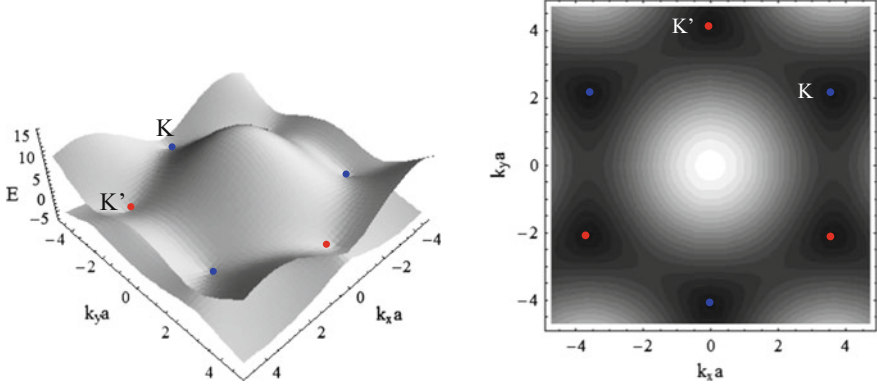


**Fig. 1.3** Dispersion relation in graphene (*left*), and its contour plot (*right*)

inequivalent points K and K' in the first Brillouin zone, called also Dirac points, the energy bandgap vanishes. From Fig. 1.3 it follows that graphene monolayer is a zero-bandgap semiconductor.

Near the Dirac points, i.e. at low energy values, the dispersion relation is:

$$E = \pm \hbar |\mathbf{k}| v_F, \quad (1.2)$$

where  $v_F = 3ta/2\hbar \cong c/300$  is the Fermi velocity and  $|\mathbf{k}| = \sqrt{k_x^2 + k_y^2}$ , with  $\mathbf{k} = (k_x, k_y)$  the wavevector of charge carriers relative to Dirac points. This linear dispersion relation is the hallmark of graphene monolayer and implies that the effective mass of charge carriers vanishes near Dirac points, unlike in common semiconductors. Another difference from common semiconductors is that the transport properties in graphene are the same for electron or hole states, since the dispersion relation is completely symmetric around the Dirac point.

In the  $\mathbf{k} \cdot \mathbf{p}$  approximation, the Dirac equation for the graphene monolayer is written as (Wu et al. 2010a):

$$-i\hbar v_F \boldsymbol{\sigma} \cdot \nabla \psi = (E - U) \psi \quad (\text{around the } K \text{ point}) \quad (1.3a)$$

$$-i\hbar v_F \boldsymbol{\sigma}^* \cdot \nabla \psi' = (E - U) \psi' \quad (\text{around the } K' \text{ point}) \quad (1.3b)$$

where  $\boldsymbol{\sigma} = (\sigma_x, \sigma_y)$ ,  $\boldsymbol{\sigma}^* = (\sigma_x, -\sigma_y)$ , with

$$\sigma_x = \begin{bmatrix} 0 & 1 \\ 1 & 0 \end{bmatrix}, \quad \sigma_y = \begin{bmatrix} 0 & -i \\ i & 0 \end{bmatrix}, \quad (1.4)$$

and  $\psi = (\psi_A, \psi_B)$  and  $\psi' = (\psi'_A, \psi'_B)$  represent the spinorial wavefunctions around the K and K' points, respectively.

The eigenvalues and eigenvectors are obtained from (1.3a, 1.3b) (considering the potential energy  $U = 0$ ) as

$$E_\alpha = \alpha \hbar v_F (k_x^2 + k_y^2)^{1/2} \quad (1.5)$$

and

$$\psi_{\alpha\beta}(\mathbf{k}) = \frac{1}{\sqrt{2}} \begin{pmatrix} \exp(-i\beta\theta/2) \\ \alpha \exp(-i\theta/2) \end{pmatrix}, \quad (1.6a)$$

respectively, where  $\alpha = \pm 1$  corresponds to the conduction and valence band, and  $\beta = \pm 1$  corresponds to K and K' valley regions. The angle  $\theta$  is given by

$$\theta = \tan^{-1}(k_y/k_x) \quad (1.6b)$$

The relation above implies that for both K and K' valleys a rotation in the  $(k_x, k_y)$  plane by  $2\pi$  produces a shift of the wavefunction with  $\pi$ , phase shift called Berry phase.

An extended version of the Dirac equation, of the form

$$\{v_F[\boldsymbol{\sigma}, \mathbf{p}] + mv_F^2 \sigma_z\} \boldsymbol{\psi} = (E - U) \boldsymbol{\psi} \quad (1.7a)$$

where  $\boldsymbol{\psi} = (\psi_A, \psi_B)^T$  is the spinor wavefunction and  $\mathbf{p} = (p_x, p_y)$  is the momentum operator, can include interactions with the substrate via the term  $\propto mv_F^2$ . In this case, expressing the wavefunction components as  $\psi_A = \phi_A \exp(ik_y y)$  and  $\psi_B = i\phi_B \exp(ik_y y)$ , we obtain the following differential equation (see Dragoman and Dragoman (2009) and the references therein):

$$d^2 \phi / d\xi^2 + (\Omega^2 - \beta^2) \phi - u' / \Omega_\pm (\pm d\phi / d\xi - \beta \phi) = 0, \quad (1.7b)$$

where the positive and negative signs correspond to  $\phi = \phi_A$  and  $\phi = \phi_B$ , respectively. In (1.7b) we used the notations:  $\xi = x/L$ ,  $\Omega_\pm = \varepsilon - u \pm \Delta$ ,  $\Omega = (\Omega_+ \Omega_-)^{1/2}$ ,  $\varepsilon = EL/\hbar v_F$ ,  $u = UL/\hbar v_F$ ,  $u' = du/d\xi$ ,  $\Delta = mv_F L/\hbar$ , and  $\beta = k_y L$ . The shape of the potential  $U$  dictates different numerical solutions.

The linear dispersion relation in (1.2), which is a specific characteristic of graphene monolayers, is retrieved in physics in only one other case: that of photons propagating in vacuum. However, the linearity of the dispersion relation has radically different meanings in these cases. In graphene, it signifies that the effective mass of charge carriers, which are fermions, is zero, and hence the interaction between electrons or holes and the crystalline lattice is very weak. As a result, the charge carriers in graphene propagate without collisions, i.e. ballistically, with the velocity  $v_F = 3ta/2 = 10^6$  m/s  $\cong c/300$ , where  $c$  is the speed of light. Thus, graphene can be modelled as a 2D gas of massless fermions. In the case of photons, which are bosons, the linear dispersion relation in vacuum  $E = \hbar\omega = hc/\lambda$  tells us that photons propagate with the speed of light. Therefore, the graphene monolayer

can be viewed as a slow-wave structure, in which the charge carriers propagate with a velocity much slower than  $c$ .

One of the most important properties of graphene is the electrical doping. If we transfer or deposit a graphene monolayer on a  $\text{SiO}_2$  layer with a thickness  $t = 300$  nm, grown thermally over a doped silicon substrate, the doped Si substrate, which has a metal-like behaviour and acts as backgate, modulates the density of charge carriers  $n$  (see Fig. 1.4) via the relation (Novoselov et al. 2004).

$$n = \epsilon_0 \epsilon_d V_G / te, \quad (1.8)$$

where  $V_G$  is the gate voltage and  $\epsilon_0$  and  $\epsilon_d$  are the dielectric permittivities of air and  $\text{SiO}_2$ , respectively.

Graphene was discovered well before 2004 (see in this respect Geim (2012)), but Novoselov and Geim (Novoselov et al. 2004) evidenced experimentally the amazing transport properties of this material. Their work was motivated by the quest of proving the electrical field effect in a metallic transistor (Geim 2011). The graphene transistor is, however, not a metallic one since  $n$  is orders of magnitude smaller than the electron density in metals. Note that the first experimental metallic transistor was found later (Dragoman et al. 2012a), and behaves similarly to the graphene field-effect-transistor (FET) depicted in Fig. 1.4.

The backgate modulation moves up and down the Fermi energy level in graphene, which is initially situated at the Dirac point, where  $n = 0$ . The Fermi energy shift is displayed in Fig. 1.5, which shows that electrical doping is able to actually select the transport carrier type ( $n$  or  $p$ ) in graphene devices. Electrical doping is similar to chemical doping, and is commonly used for changing the transport type in semiconductor devices. Depending on the position of the Fermi energy/gate voltage, the transport in graphene is ambipolar, i.e. it is performed by either electrons or holes. Moreover, unlike in other materials, the transport properties of graphene monolayers are the same for electrons and holes due to the linear dispersion relation and its symmetry with respect to the Dirac points (Dragoman and Dragoman 2014), as suggested by Fig. 1.5. Therefore, electrons and holes in

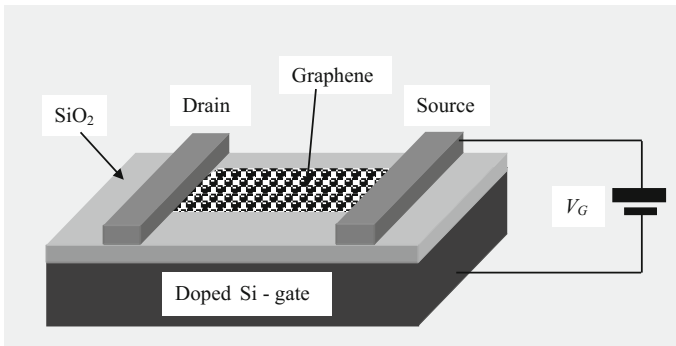
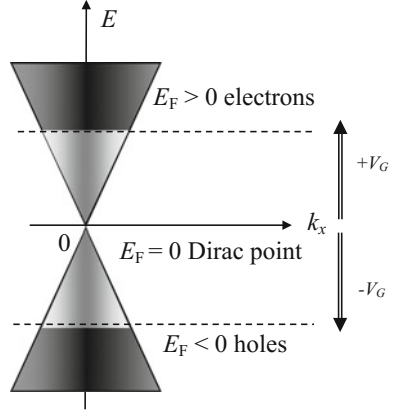


**Fig. 1.4** Typical configuration of a graphene FET

**Fig. 1.5** Electrical doping in graphene



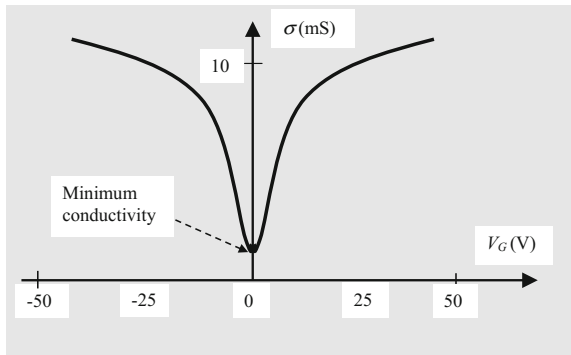
graphene are analogous to matter and antimatter particles, such as electrons and positrons, which are another groundbreaking consequence of the Dirac equations, this time for massive particles.

The conductivity dependence on the gate voltage, shown in Fig. 1.6, illustrates the similar transport properties of electrons and holes in an ambipolar monolayer graphene flake. Moreover, by modifying the gate voltage, graphene conductivity  $\sigma$  can be changed significantly; this behavior is similar to conductivity changes in a reversible metal-insulator transition in a large range of temperatures, including room temperature, since the conductivity in graphene depends only weakly on temperature. The dependence  $\sigma(V_G)$  is essential in any graphene-based applications, and can be used to determine other parameters (Tan et al. 2006).

For instance, the mobility of charge carriers can be deduced from resistivity  $\rho$  or conductivity as:

$$\mu = (en\rho)^{-1} = \sigma/en. \quad (1.9)$$

**Fig. 1.6** Typical gate-voltage dependence of conductivity in graphene



In this Drude model

$$n = C_G(V_G - V_{Dirac})/e = C_G V_G/e + n_{imp} \quad (1.10)$$

where  $C_G$  is the experimentally deduced or calculated gate capacitance and  $n_{imp}$  is the carrier density associated to impurities. In other words, expression (1.10) implies that impurities induce an offset voltage, given by  $V_{Dirac} = -en_{imp}/C_G$ ; in the absence of impurities,  $V_{Dirac} = 0$  V. The impurity concentration can be determined from  $V_{Dirac}$ , which is the voltage where the conductivity is minimum. Typical impurity concentrations in graphene samples are around  $1\text{--}3 \times 10^{11} \text{ cm}^{-2}$ . From (1.9) and (1.10) it follows that the mobility in graphene is divergent near  $V_G = V_{Dirac}$ .

Other parameters linked to graphene conductivity are the scattering rate, given by

$$\tau = \mu E_F / (e^2 v_F) = \hbar \sigma(V_G) (\pi/n)^{1/2} / (e^2 v_F) \quad (1.11a)$$

and the mean-free-path, defined as

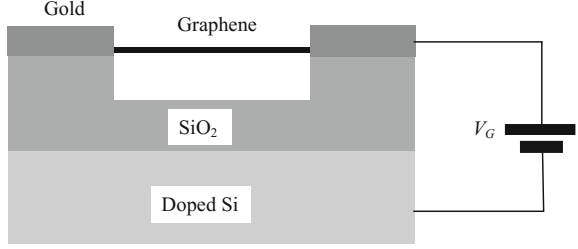
$$l = v_F \tau = (\hbar/2e) \mu (n/\pi)^{1/2} \quad (1.11b)$$

Both mobility and mean-free-path have impressive values in graphene, supporting the extensive research for graphene-based nanoelectronic devices. Even in the first published paper about this material (Novoselov et al. 2004) the mobility was as high as  $10,000 \text{ cm}^2/\text{V s}$  for  $n = 5 \times 10^{12} \text{ cm}^{-2}$  with a room-temperature mean-free-path value of 400 nm. Two years later, it was reported that mobility values vary very much for the same carrier concentration, depending on the sample quality (Tan et al. 2006). For example, at  $n = 2 \times 10^{12} \text{ cm}^{-2}$  the mobility on five samples took values from 2,000 up to 20,000  $\text{cm}^2/\text{V s}$  at low temperatures. The corresponding variation of the scattering time, from 50 to 500 fs, indicated that sample quality, i.e. a low or large defect concentration, dictates the mobility value.

In addition, the mobility in graphene is strongly dependent also on the substrate on which graphene is deposited. In the above mentioned first paper on electrical properties of graphene (Novoselov et al. 2004), the substrate was  $\text{SiO}_2$  with a thickness of about 300 nm grown over doped Si, which plays the role of a backgate. However, the suspension of graphene at 150 nm above  $\text{SiO}_2$  deposited over Si, as shown in Fig. 1.7, drives the mobility up to 200,000  $\text{cm}^2/\text{V s}$  in vacuum and at low temperatures of 5 K, for graphene samples annealed at 400 K (Bolotin et al. 2008). The gate voltage in this case was maintained within the range (−5 V, 5 V) to avoid the generation of too much strain in the sample.

Note that, although very large mobilities in suspended graphene, of about 100,000–200,000  $\text{cm}^2/\text{V s}$ , are obtained only in vacuum and at low temperatures, such values are considered as a hallmark for graphene, without any specification regarding measurement conditions and temperature. The last parameter affects much more the conductivity of suspended graphene than that of graphene on

**Fig. 1.7** Suspended graphene configuration



various substrates (Du et al. 2008). Moreover, suspended graphene is extremely fragile in ambient conditions and very difficult to anneal. Room-temperature ballistic transport over  $1\ \mu\text{m}$  and a mobility of  $100,000\ \text{cm}^2/\text{V s}$  at  $n \cong 10^{11}\ \text{cm}^{-2}$  was obtained, nevertheless, in a graphene monolayer sandwiched between two hexagonal boron nitride (h-BN) layers with thicknesses of about  $10\ \text{nm}$  (Mayorov et al. 2011). In addition, exceptional ballistic transport, i.e. a mean-free-path of  $10\ \mu\text{m}$ , and a mobility exceeding  $100,000\ \text{cm}^2/\text{V s}$  was reported at room temperature in graphene nanoribbons grown epitaxially on SiC and having a width of  $40\ \text{nm}$  (Baringhaus et al. 2014). Exceptional charge transport properties of graphene transferred on (100) Ge were also demonstrated (Cavallo et al. 2014), the mobility attaining  $5 \times 10^5\ \text{cm}^2/\text{V s}$  at  $20\ \text{K}$  and  $10^3\ \text{cm}^2/\text{V s}$  at room temperature at a carrier density of  $10^{14}\ \text{cm}^{-2}$ .

Very often, the mobility of graphene is measured from electrical characteristics of a graphene FET-like configuration, whether in the form of backgate configuration, top gate configuration, or side gate geometry (see Fig. 1.8). The mobility is then extracted from the relation

$$\mu = (W/L)(\partial I_D / \partial V_D) / (en) \quad (1.12a)$$

or

$$\mu = (L/C_G W)(\partial G / \partial V_G) \quad (1.12b)$$

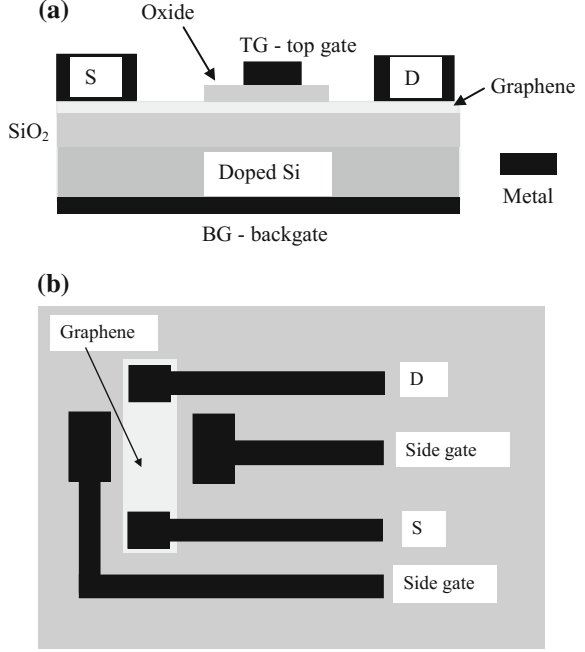
where  $W$ , and  $L$  are the width and the length of the channel, respectively,  $V_D$  and  $V_G$  are the drain and gate voltages,  $I_D$  is the drain current and  $G$  the channel conductance. DC measurements of a graphene FET and its geometry can be used to determine not only the mobility of graphene (Sabri et al. 2009) but of any type of channel, either organic or 2D material, such as black phosphorous (Koenig et al. 2014).

As discussed above, the mobility is dependent on the intrinsic carrier density  $n$ , which in turn is determined by the density of states (DOS) in graphene  $D_{gr}$  as follows

$$n = \int_0^\infty dE D_{gr}(E) f(E) \quad (1.13)$$



**Fig. 1.8** Graphene FET with  
**a** backgate and top gate, and  
**b** side gates



where

$$f(E) = \frac{1}{1 + \exp[(E - E_F)/k_B T]} \quad (1.14)$$

is the Fermi-Dirac distribution function. In the neighbourhood of the Dirac points, the DOS can be approximated as (Castro Neto et al. 2009)

$$D_{gr} = \frac{3\sqrt{3}a^2}{\pi} \frac{|E|}{v_F^2}. \quad (1.15)$$

At thermal equilibrium, the Fermi level is located at the Dirac point and corresponds to  $E_F = 0$  eV. The intrinsic carrier concentration in graphene is then:

$$n = p = n_i = (\pi/6)(k_B T / \hbar v_F)^2 \quad (1.16)$$

the corresponding value of this parameter at room temperature being  $9 \times 10^{10} \text{ cm}^{-2}$ .

Although the DOS of graphene vanishes at the Dirac point, the conductivity has a minimum finite value at this point, as shown in Fig. 1.6. The nature of the minimum conductivity in graphene has no unique explanation, several theories

attempting to elucidate this phenomenon. Among these, it is believed that the minimum conductivity  $\sigma_{\min} = 4e^2/h$  originates in the quantum mechanical uncertainty principle (Dragoman 2010).

The conductivity in graphene, which consists of two components: intraband and interband conductivities:

$$\sigma = \sigma_{\text{intra}} + \sigma_{\text{inter}} \quad (1.17)$$

depends on frequency (Hanson 2008). The frequency (and temperature,  $T$ ) dependence of the intraband term is given by

$$\sigma_{\text{intra}} = -i \frac{e^2 k_B T}{\pi \hbar^2 (\omega - i2\Gamma)} \left( \frac{\mu_c}{k_B T} + 2 \ln[\exp(-\mu_c/k_B T) + 1] \right) \quad (1.18a)$$

where  $\mu_c$  is the chemical potential and  $\Gamma$  is the scattering rate, which is typically 0.11 meV. The intraband term dominates the graphene conductivity over an ultrawideband of frequencies, from DC up to 1 THz (Sensale-Rodríguez et al. 2013), the real part of  $\sigma_{\text{intra}}$  being much larger than the imaginary part in this frequency range.

On the contrary, in the range 1–30 THz the interband conductivity

$$\sigma_{\text{inter}} = -i(e^2/4\pi\hbar) \ln \left( \frac{2|\mu_c| - \hbar(\omega - i2\Gamma)}{2|\mu_c| + \hbar(\omega - 2i\Gamma)} \right) \quad (1.18b)$$

is predominant, its real part being much smaller than the imaginary part.

Graphene exhibits unusual properties when subject to a magnetic field. These properties are studied using a graphene Hall bar configuration, depicted in Fig. 1.9. For example, despite the vanishing effective mass of electrons and holes in graphene, a finite cyclotron mass of carriers can be defined as (Novoselov et al. 2005)

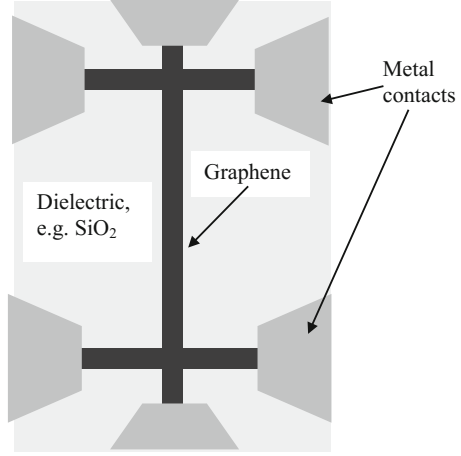
$$m_c = E/v_F^2 = \hbar\sqrt{\pi n}/v_F. \quad (1.19)$$

If a magnetic field  $B$  is applied normally to the graphene plane, the linear dispersion relation is modified due to the emergence of Landau levels. This is the only known method to discretize the energy spectrum in 2D graphene, the energy levels being given by (Castro-Neto et al. 2009)

$$E_n - V = \pm v_F \sqrt{2eB\hbar|n|} \quad (1.20)$$

with  $n$  an integer. The Landau levels in (1.20) are different from those for charge carriers with effective mass  $m_{\text{eff}}$  obeying the Schrödinger equation:  $E_n = \hbar(eB/m_{\text{eff}})(n + 1/2)$ , and result in quantized values of the Hall conductivity:

**Fig. 1.9** Graphene Hall bar configuration



$$\sigma_{xy} = (n + 1/2)(4e^2/h). \quad (1.21)$$

The above quantized conductance is dependent also on the gate voltage, which changes  $n$ . The discretized energy levels in magnetic fields can be used in various applications, such as electron spectrometers (Zubarev and Dragoman 2012).

Graphene nanoribbons (GNRs) are graphene stripes with widths that do not exceed 100 nm. This spatial confinement of charge carriers in graphene changes their properties. Considering the  $x$  axis as the longitudinal axis of the GNR, the wave vector is quantized in the transverse direction,  $y$ , so that

$$k_y = n\pi/W \quad (1.22)$$

where  $n = \pm 1, \pm 2, \dots$  are integers. Thus, the dispersion relation becomes (Fang et al. 2007)

$$E_s(n, k_x) = s\hbar v_F [k_x^2 + (n\pi/W)^2]^{1/2} \quad (1.23)$$

where  $s = +1$  for electrons, and  $s = -1$  for holes. From (1.23) it follows that the conduction and valence bands of graphene are broken into a series of 1D subbands. More importantly, a band gap is opened with a width

$$E_g = E_{+1}(1, 0) - E_{-1}(1, 0) = 2\pi\hbar v_F/W, \quad (1.24)$$

which depends only on the width of the GNR. The equation above is similar to the bandgap of semiconducting carbon nanotubes (CNTs), which is inversely proportional to the nanotube diameter. The bandgap vanishes when the GNR becomes wider than 90 nm. The Table 1.1 shows some values of the bandgap extracted from experimental results (Han et al. 2007).

**Table 1.1** The bandgap of GNR

Width (nm)	$E_g$ (meV)
15	100
30	20
60	5
90	3

The DOS of the  $n$ th subband is given by

$$D_{GNR}(n, E) = \frac{4}{\pi \hbar v_F} \frac{E}{\sqrt{E^2 - E_n^2}} H(E - E_n) \quad (1.25)$$

where  $H(E - E_n)$  is the Heaviside step function, and

$$E_n = n\pi \hbar v_F / W = nE_g / 2. \quad (1.26)$$

The DOS of the GNR is then obtained as

$$D_{GNR}(E) = \sum_n D_{GNR}(n, E) \quad (1.27)$$

Similarly as in graphene, where the carrier density can be tuned via an applied gate voltage  $V_G$ , the carrier density in a GNR,

$$n_{GNR} = \frac{4k_B T}{\pi \hbar v_F} \sum_n \int_{E_n/k_B T}^{\infty} \frac{u}{\sqrt{u^2 - (E_n/k_B T)^2}} \frac{du}{1 + \exp(u - \eta)}, \quad (1.28)$$

where  $\eta = E_F/k_B T$ , is also dependent on  $V_G$  through the relation  $E_F = eV_G$ . Then, by denoting with  $n_i$  the intrinsic carrier concentration corresponding to  $\eta = E_F = 0$  in (1.28), for an arbitrary Fermi level we have

$$n \cong n_i \exp(\eta), \quad p \cong n_i \exp(-\eta) \quad (1.29)$$

The total charge, defined as  $Q = e(p - n)$ , determines the quantum capacitance  $C_q = \partial Q / \partial V_G$  as

$$C_q = [2e^2 k_B T / \pi (\hbar v_F)^2] \ln[2(1 + \cosh(eV_G/k_B T))] \quad (1.30)$$

which, when  $eV_G \gg k_B T$ , becomes

$$C_q \cong e^2 D_{GNR}(eV_G). \quad (1.31)$$

Because the massless charge carriers in graphene are described by a Dirac-like equation, similar to that describing ultrarelativistic spin-1/2 massive particles, we can test in graphene effects predicted by quantum field theories. One of them is the

Klein paradox, which in graphene predicts that potential barriers, as those forming at an interface between regions with potential energies  $V_1 > 0$  and  $V_2 < 0$  (see Fig. 1.10), do not impede charge carrier transport. More precisely, charge carriers propagate through such potential barriers by (successive) transformations of electron states into hole states and vice versa (Katsnelson et al. 2006). However, the Klein paradox at a step-like barrier is more controversial since it predicts higher than 1 reflection and negative transmission coefficients, associated to the creation of electron-positron pairs at the potential discontinuity. Thus, transport experiments in  $n$ - $p$  junctions in graphene are able to test these predictions, which cannot be verified up to now for relativistic massive particles. In particular, the Klein paradox at a step-like barrier with the above-mentioned meaning is invalidated in graphene, both by theory (Dragoman 2009) and experiments (Young and Kim 2009; Stander et al. 2009) demonstrating that even at a step-like barrier, i.e. at an  $n$ - $p$  junction, the reflection and transmission coefficients of charge carriers are less than 1.

The Dirac spinors  $\Psi_1$  and  $\Psi_2$ , which satisfy the Dirac-like equation for an electron wavefunction incident at an angle  $\varphi_1$  with respect to the  $x$  axis from region 1 on a barrier of height  $V_0 = V_2 - V_1$  and width  $D$  (see Fig. 1.11), are given by

$$\Psi_1(x, y) = \begin{cases} [\exp(ik_1x) + r \exp(-ik_1x)] \exp(ik_y y), & x \leq 0 \\ [a \exp(ik_2x) + b \exp(-ik_2x)] \exp(ik_y y), & 0 < x < D \\ t \exp(ik_3x) \exp(ik_y y), & x \geq D \end{cases} \quad (1.32a)$$

$$\Psi_2(x, y) = \begin{cases} s_1 [\exp(ik_1x + i\varphi_1) - r \exp(-ik_1x - i\varphi_1)] \exp(ik_y y), & x \leq 0 \\ s_2 [a \exp(ik_2x + i\varphi_2) - b \exp(-ik_2x - i\varphi_2)] \exp(ik_y y), & 0 < x < D \\ s_3 t \exp(ik_3x + i\varphi_3) \exp(ik_y y), & x \geq D \end{cases} \quad (1.32b)$$

In the above equations, the  $x$  wavevector components in the three regions can be approximated by:

$$k_1 = k_F \cos \varphi_1 = [(E - V_1)^2 / \hbar^2 v_F^2 - k_y^2]^{1/2}, \quad (1.33a)$$

**Fig. 1.10** Klein paradox in graphene

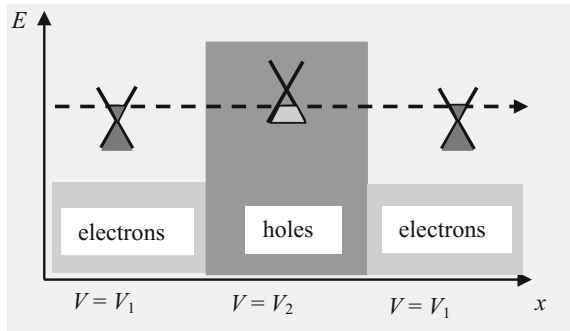
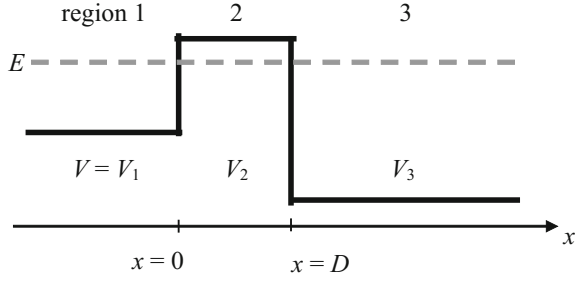


**Fig. 1.11** Tunneling of Dirac fermions through a rectangular barrier



$$k_{2,3} = [(E - V_{2,3})^2 / \hbar^2 v_F^2 - k_y^2]^{1/2}, \quad (1.33b)$$

where  $k_F$  is the Fermi wavenumber,  $k_y = k_F \sin \varphi_1$ , the propagation angles in the second and third regions are  $\varphi_{2,3} = \tan^{-1}(k_y/k_{2,3})$ ,  $s_i = \text{sgn}(E - V_i)$ ,  $i = 1, 2, 3$ , with  $E$  the electron energy. Note that (1.32a, 1.32b) and (1.33a, 1.33b) can describe propagation of electrons through a gated region, which induces a potential  $V_0$ , in the presence of a bias  $V$  applied on the structure, such that the potential energy can be modelled as having a step-like variation (Dragoman and Dragoman 2007a). In the last case  $V_1 = 0$ ,  $V_2 = V_0 - eV/2$ , and  $V_3 = -eV$ .

Then, the transmission coefficient through the barrier, defined as

$$T = s_3 \cos(\varphi_3) |t|^2 / s_1 \cos(\varphi_1), \quad (1.34)$$

is computed using the wavefunction continuity requirement at the  $x = 0$  and  $x = D$  interfaces. The results show that, when the electron energy  $E$  is higher than the potential energy, as is the case in the first and third regions in Fig. 1.11, electrons are involved in the transport, but in the barrier region, where the electron energy is smaller than the potential energy, holes take over the charge transport role. The term “barrier” in graphene does not refer to a region of evanescent propagation as in common semiconductors, at least for normal incidence, but a region in which an abrupt change in charge carrier concentration and/or type (holes or electrons) takes place.

In particular, in a gated region in the absence of an applied bias, i.e. when  $V_3 = V_1 = 0$  and  $V_2 = V_0$ , the reflection coefficient has a simple analytic formula (Katsnelson et al. 2006):

$$r = \frac{2i \exp(i\varphi_1) \sin(k_2 D) [\sin \varphi_1 - s_1 s_2 \sin \varphi_2]}{s_1 s_2 [\exp(-ik_2 D) \cos(\varphi_1 + \varphi_2) + \exp(ik_2 D) \cos(\varphi_1 - \varphi_2)] - 2i \sin(k_x D)} \quad (1.35)$$

If  $|V_0| \gg |E|$ , the transmission coefficient  $T = |t|^2 = 1 - |r|^2$  is

$$T \cong \cos^2 \varphi_1 / [1 - \cos^2(k_2 D) \sin^2 \varphi_1] \quad (1.36)$$

and there are resonances, i.e.  $T = 1$ , when

$$k_2 D = \pi N, \quad (1.37)$$

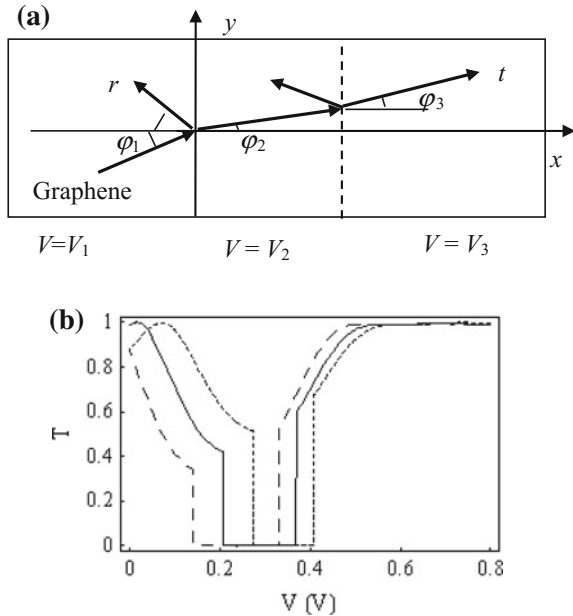
with  $N$  an integer.

The fact that the transmission  $T$  is angle dependent was experimentally demonstrated in (Sutar et al. 2012). More importantly, the barrier becomes transparent, i.e.  $T = 1$ , at normal incidence, for  $\varphi_1 = 0$ , which is a specific manifestation of the Klein paradox, or Klein effect, in monolayer graphene. On the contrary, in bilayer graphene, in which charge carriers have a finite mass,  $T = 0$  at normal incidence (Katsnelson et al. 2006).

The Klein paradox in graphene is an interesting effect from a physical point of view, but a detrimental effect for graphene ballistic devices, since the modulation of the transmission coefficient  $T$  using electrostatic gates at normal incidence is not possible because always  $T = 1$ . This situation, encountered only in graphene devices, is solved by using oblique incidence, i.e. oblique gates (Katsnelson et al. 2006), or magnetic fields.

In the case of an oblique electrostatic gate, as the one depicted in Fig. 1.12a, the transmission coefficient can be tuned by varying either the applied gate voltage  $V_2 = eV_G$  or the applied drain voltage  $V_D$ , as can be seen from Fig. 1.12b, where the three curves correspond to different Fermi levels/gate voltages. The voltage region where  $T = 0$  in this figure corresponds to the range of parameter values for which the wavenumber in the gated region is imaginary. As a result, the device displays a negative differential resistance (NDR) region, the current decreasing dramatically in the region with  $T = 0$  while the voltage increases (Dragoman and Dragoman 2007a).

**Fig. 1.12** **a** Carrier transport through an obliquely gated graphene region and **b** voltage dependence of the transmission coefficient for different gate values (from Dragoman and Dragoman 2007a)



Low transmission regions can be obtained also in periodically gated structures due to the formation of minibands (Dragoman and Dragoman 2008a).

A ballistic graphene FET with an oblique gate was recently fabricated and the NDR effect due to the modulation of the transmission was experimentally evidenced (Dragoman et al. 2014a) and is displayed in Fig. 1.13. A room-temperature peak-to-valley ratio of 9 was obtained in the NDR region of this graphene FET with a top gate having a tilting angle of  $45^\circ$  and a drain-source distance of 400 nm. Tens of such devices were fabricated on a chip cut from a 4-in. graphene wafer grown by CVD.

The Klein tunneling was experimentally evidenced in graphene  $p$ - $n$  junctions (Young and Kim 2009; Stander et al. 2009) by tuning the top gate and backgates of devices fabricated on doped Si/SiO<sub>2</sub> structures. More precisely, in (Young and Kim 2009) the Klein tunneling effect is evidenced by conductance measurements under the hypothesis that the application of a magnetic field on ballistic heterostructures bends the trajectories of carriers, so that the resulting Aharonov-Bohm phase modifies the angle of incidence on the  $p$ - $n$  junction. In this case, the conductance is given by

$$G \cong (8e^2/h) \sum_{k_y} |T_+|^2 |T_-|^2 |R_+|^2 |R_-|^2 \cos \varphi \exp(-2L/l) \quad (1.38)$$

where  $T_{\pm}$  and  $R_{\pm}$  are the transmitted and reflected wavefunction amplitudes for the forbidden regions located at  $x = \pm L/2$ ,  $\varphi$  is a sum of the semiclassical phase due to interfering trajectories and the backreflection phase,  $L$  is the gate length of the Klein device depicted in Fig. 1.14, and  $l$  is the mean-free path. In magnetic fields, the conductance oscillates as a function of the carrier density, showing phase shifts that

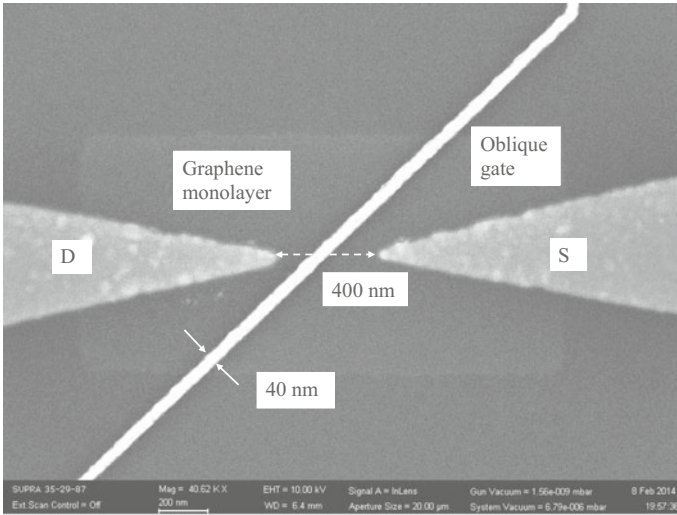
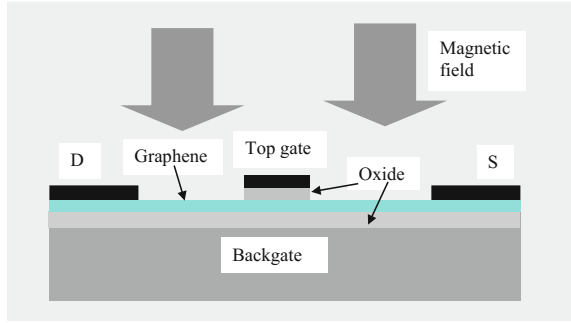


**Fig. 1.13** Ballistic graphene FET with oblique gate (from Dragoman et al. 2014a)



**Fig. 1.14** Ballistic device for Klein tunneling measurements



indicate perfect transmission. When  $T = 1$ , i.e. when Klein tunneling occurs, a phase jump of  $\pi$  is observed. The measurements are made at low temperature. In (Stander et al. 2009) Klein tunnelling was evidenced by resistance measurements in top-gated graphene structures with abrupt gate-induced potential steps, using a four-probe measurement setup.

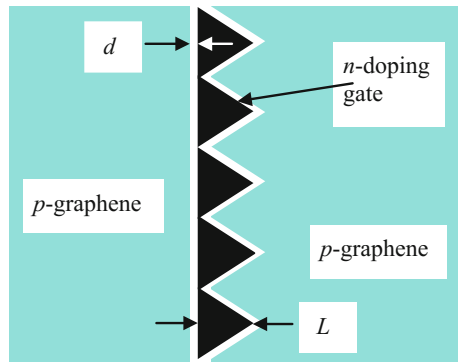
A graphene Klein tunneling transistor based on a gate having a prism chain configuration was recently proposed (Wilmart et al. 2014) and is illustrated schematically in Fig. 1.15. Total reflection can be induced in this  $n$ -doped prism surrounded by  $p$ -doped regions, depending on the gate voltage. The reflection angle and the angle-dependent transmission of carriers are determined by the refractive index-like parameter

$$v = -(n/p)^{1/2} \quad (1.39)$$

Denoting by  $\alpha_i$  and  $\alpha_r$  the angles of incidence and transmission of ballistic carriers at the tunnelling prism, respectively, the Snell law applied to the prism is expressed as

$$\sin \alpha_i = v \sin \alpha_r \quad (1.40)$$

**Fig. 1.15** Klein tunneling transistor



The transistor is in the off state (small conductance) when  $n \gg p$  and in the on state (large conductance) when  $n \cong p$ . The gate length  $L$  is around 100 nm and the distance  $d$  between two different doped regions is around 10 nm.

Besides Klein paradox, another quantum effect that can be tested in graphene is the atomic collapse. An atomic collapse state due to strong Coulomb interactions is predicted by the quantum field theory if the charge of a superheavy atomic nucleus exceeds a certain threshold. At the threshold condition, i.e. at resonance, the electron wavefunction plunges towards the nucleus and, simultaneously, a positron escapes to infinity. Because the charge carriers in graphene are analogous to massless relativistic particles, highly charged impurities could display resonances mimicking the atomic collapse. Such an experiment was recently performed (Wang et al. 2013) using artificial nuclei consisting of clusters of charged Ca dimmers placed on gated graphene devices and manipulated by a scanning tunneling microscope (STM). The atomic collapse-like states, observed in larger clusters, are distinguished by a peak in the  $dI/dV$  dependence on voltage situated below the Dirac point.

The thermal properties of graphene are also impressive, and are reviewed in (Balandin 2011). The Fourier equation for the heat flux  $q$  is  $q = -K\nabla T$ , where  $K$  is the thermal conductivity and  $\nabla T$  is the temperature gradient. The thermal conductivity  $K = K_p + K_e$  has two contributions: one from phonons,  $K_p$ , and the other from electrons,  $K_e$ . In metals, the electrons' contribution to thermal conductivity is dominant, while in carbon-based materials the phonons' contribution prevails.

Carbon nanotubes and graphene have thermal conductivities with about one order of magnitude larger than that of copper. In copper, which is used for interconnections in very large scale integrated circuits, partly because of its high thermal conductivity,  $K = 400 \text{ W mK}^{-1}$ . Multiwalled CNTs have thermal conductivities  $>3000 \text{ W mK}^{-1}$ , while in graphene this parameter takes values in the range  $2000\text{--}5000 \text{ W mK}^{-1}$ .

Graphene has also important thermoelectric properties. Although experiments have shown thermoelectric power values of  $100 \mu\text{V/K}$  and the Seebeck coefficient  $S$  is high and tunable by the gate voltage, the figure of merit of graphene is around 1 due to a high phonon thermal conductivity  $K_p$ . The figure of merit, defined as  $ZT = S^2GT/(K_e + K_p)$ , with  $G$  the electronic conductance, can be enhanced in GNRs up to 4, since edge disorder can reduce  $K_p$  (Sevinçli and Cuniberti 2010). Alternatively, a periodic electrode structure patterned on graphene (Dragoman and Dragoman 2007b) can maximize the Seebeck coefficient, which is given by

$$S = \Delta V / \Delta T = (\pi^2 k_B^2 T / 3e) \partial \ln T_q(E) / \partial E|_{E=E_F} \quad (1.41)$$

where  $T_q(E)$  is the energy-dependent quantum transmission coefficient of ballistic electrons through the structure represented in Fig. 1.16. For maximum  $S$  values, the transmission  $T_q(E)$  must consist of a series of sharp peaks, which can develop at the edges of the minibands induced in this periodic structure. At these edges, the thermoelectric effect is giant, a typical dependence of the Seebeck coefficient on the gate voltage being displayed in Fig. 1.17.

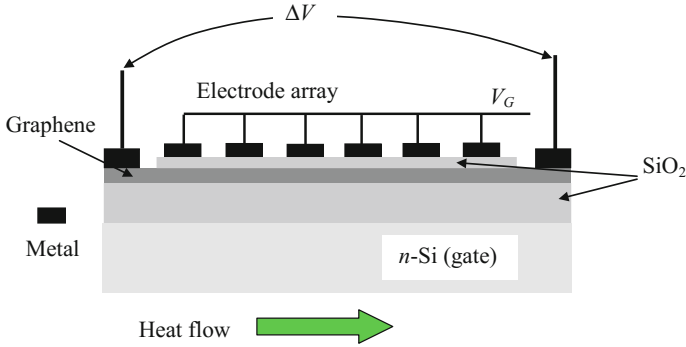
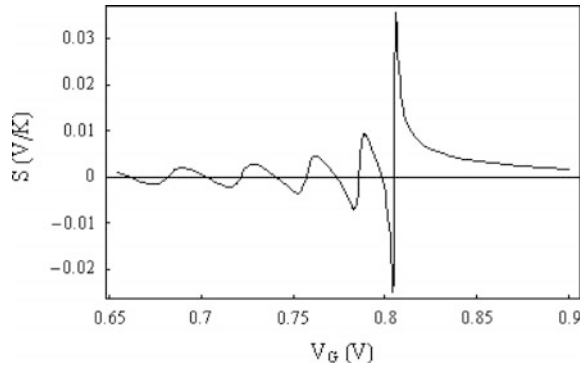


**Fig. 1.16** Thermoelectric graphene structure periodically loaded with metallic electrodes

**Fig. 1.17** The Seebeck coefficient of the structure represented in Fig. 1.16 (from Dragoman and Dragoman 2007b)



Finally, we summarize in Table 1.2 the main physical properties of graphene; other properties will be revealed during the next sections, which deal with graphene applications in nanoelectronics, sensors, and photonics.

The physical properties of graphene are strongly dependent on the growth methods. There are many review papers and several books about this subject (see, for instance Whitener Jr and Sheehan (2014)), the main growth methods and the yield of each of them being indicated in Table 1.3. Nowadays, two methods are intensively used. The first one, in which graphene is grown via CVD on Cu substrates, is most intensively used because it is able to produce graphene on 4-in. and even 6-in. Si wafers by transfer methods, but the quality of graphene still needs to be improved. The second method, of epitaxial graphene growth starting from SiC is also very promising, but implies very expensive equipments and high working temperatures. The quality of graphene is comparable with the CVD method, but large graphene areas are still expensive to be produced.

**Table 1.2** The main physical parameters of graphene

Parameter	Value at room temperature	Applications
Mean-free-path	400 nm, even 1 $\mu\text{m}$ or greater for graphene deposited on h-BN	ballistic devices: transistors and diodes for microwave, THz or photonics
Mobility	40,000 $\text{cm}^2/\text{V s}$ (intrinsic) 100,000 $\text{cm}^2/\text{V s}$ in suspended graphene or in graphene deposited on h-BN	transistors, high-frequency applications
Effective mass of carriers	0 close to the Dirac point	ballistic devices
Thermal conductivity	5000 W/mK, higher than in many metals	thermal interfaces, interconnects
Young modulus	1.5 TPa, ten times greater than in steel	NEMS, sensors

**Table 1.3** Graphene growth methods properties

Material	Method	Yield	Graphene surface
Graphite	Repetitive peeling of HOPG	Low	Small
SiC	Desorption of Si atoms at high temperature	Moderate	Moderate (3–4 in. wafers)
GO	GO dispersion into hydrazine	High	Large
CVD	Gas mixture ( $\text{CH}_4$ and $\text{H}_2$ )	Very high	Very large (30 in.)

## 1.2 Nanoelectronics on 2D Carbon-Based Materials

### 1.2.1 The Graphene FET

The most studied graphene-based device is the graphene FET. All graphene physical properties recommend graphene as channel for FET applications (Dragoman and Dragoman 2009). We have presented above the top gate (TG) and backgate (BG) configurations of the graphene FET, which directly revealed the physical properties of graphene.

For a more detailed discussion of the graphene FET let us consider the TG configuration in the quantum capacitance limit regime, where the gate capacitance is much higher than the quantum capacitance:  $C_G \gg C_q$ . We follow further this model since it is able to provide the basic characteristics of graphene FETs. In the quantum capacitance limit regime, the drain current has the expression (Parrish and Akinwande 2012):

$$I_D = eW/L \int_0^L n(x) v_{\text{drift}} dx \quad (1.42)$$

where  $L$  is the gate/channel length,  $W$  is the gate width, and  $x$  is the position along the channel. The drift velocity is given by

$$v_{drift} = \mu E / [1 + (\mu E / v_{sat})^\alpha]^{1/\alpha} \quad (1.43)$$

where  $\alpha = 2$  for graphene transistors, and the saturation velocity  $v_{sat} = v_F/2$  is constant.

If the channel voltage increases linearly with  $x$ :

$$V_{ch} = (x/L)V_D, \quad (1.44)$$

the surface potential is given by

$$\varphi_s(x) = V_G - V_{ch}(x). \quad (1.45)$$

Considering that

$$n = n_0 + [e\varphi_s(x)]^2 / \pi \hbar^2 v_F^2 \quad (1.46)$$

where  $n_0$  is the concentration of impurities and intrinsic carriers, we obtain the following analytic expression for the main DC characteristics  $I_D(V_D, V_G)$  of the graphene FET, where  $V_G$  is the gate voltage:

$$I_D(V_D, V_G) = e(W/L)\mu^* V_D [n_0 + \gamma(V_G^2 + V_D^2/3 - V_D V_G)]. \quad (1.47)$$

In (1.47),  $n_0 \cong 10^{11} \text{ cm}^{-2}$ ,  $\mu^* = \mu[1 + (\mu V_D / v_{sat} L)]$  and  $\gamma = e^2 / \pi \hbar^2 v_F^2$  is a constant.

Inversely, if the mobility is not known, it can be extracted from DC measurements of  $I_D(V_D, V_G)$  according to the formula

$$\mu = \frac{1}{en} \frac{\partial I_D / W}{\partial V_D / L} \quad (1.48)$$

We consider further some examples (Dragoman and Dragoman 2014). The  $I_D - V_D$  curve consists of three regions, as shown in Fig. 1.18: (I) the sublinear region, (II) the saturation region, where the Dirac point is retrieved at  $V_D = V_G$ , and (III) the superlinear region, which originate in the lack of a graphene monolayer bandgap.

The  $I_D - V_G$  dependence is represented in Fig. 1.19. Note that the drain current does not vanish when the gate voltage is zero, due to the finite minimum conductivity of graphene. The minimum value of the  $I_D(V_G)$  curve is obtained at the Dirac point,  $V_{G,Dirac}$ . If  $V_G > V_{G,Dirac}$ , the conductivity is of  $n$ -type, whereas  $p$ -type conductivity is obtained for  $V_G < V_{G,Dirac}$ . The  $I_D - V_G$  curve has a typical “V-like”-shape for any graphene FET. The ambipolar transport, which is the imprint of 2D materials, is at the origin of this V-shaped dependence.

**Fig. 1.18** Typical  $I_D - V_D$  dependence of graphene FETs at a certain gate voltage

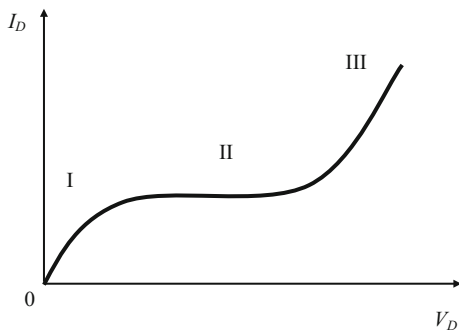
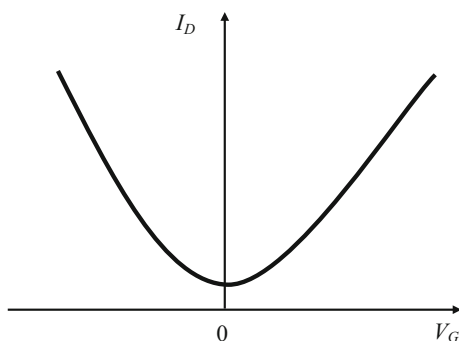


**Fig. 1.19** Typical  $I_D - V_G$  dependence of graphene FETs at a certain drain voltage



The large graphene/metal contact resistance is a serious problem of graphene transistors, downgrading significantly the graphene FET performances. This issue is an intensive subject of research, and a large amount of information on this subject has been gained in recent years. In particular, metals with high workfunctions, more precisely with workfunctions near that of graphene ( $-4.5$  eV) are selected for low contact resistance (Reddy et al. 2011). For example, Ti/Pd/Au has a contact resistance of  $750 \Omega \mu\text{m}$ , i.e. a contact resistivity of  $2 \times 10^{-6} \Omega \text{cm}^2$ , which is similar to the contact resistance in GaAs technology (Huang et al. 2011a). In addition, various technological treatments can reduce the contact resistance of graphene FETs (see Leong et al. (2014) and the references therein), such as soft plasma treatment, ultraviolet/ozone treatment and annealing. The role of these treatments is to destroy the resist residues, which are left on graphene FETs during their fabrication processes via lithographic techniques, such as electron-beam lithography. As shown in (Leong et al. 2014), residue-free metal (Ni)-graphene contacts can be fabricated using a shadow mask. It was found that the contact resistance is reduced from  $600$  to  $340 \Omega \mu\text{m}$  (these values depend slightly on the gate voltage) by annealing for 1 h at  $300^\circ\text{C}$ , because carbon dissolves from graphene into Ni at the chemisorbed Ni-graphene interface, producing many end-contacts between metal and the dangling bonds, these contacts causing a significant decrease of the contact resistance.

There are different graphene-FETs, with different operation principles. For instance, graphene MOSFETs are similar to any MOSFETs, except that graphene is the channel. There also graphene FETs with various gate architectures, such as top gate and/or backgate, side gates, tunnel graphene FETs and vertical FETs (Schwartz 2013).

In the graphene MOSFET (see Fig. 1.20), the top gate and/or backgate transconductance, defined as  $g_m = \partial I_D / \partial V_G$ , determines the cutoff frequency of the transistor  $f_T = g_m / (2\pi C_G)$ , where  $C_G$  is the gate capacitance.

A high cutoff frequency is possible if  $g_m$  is high and the gate length is small. The self-aligned gate technology applied to graphene FETs displays cutoff frequencies beyond 300 GHz (Liao et al. 2010). The graphene FET performances can be further enhanced if the device works in the quantum capacitance limit. This means a thickness of the oxide of few nm and high-permittivity dielectrics. For example, a graphene FET based on  $Y_2O_3$  (relative permittivity of 10) gate dielectric with a thickness of 3.9 nm and an oxide capacitance of  $2.28 \mu\text{F}/\text{cm}^2$ , works near the quantum capacitance limit (Xu et al. 2011). In this case, the cutoff frequency of the graphene FET,  $f_T$ , and  $f_{\max}$  (the maximum frequency at which the transistor oscillates and provides power, i.e. the frequency for which the power gain is 1) can be defined using its equivalent circuit represented in Fig. 1.21.

For graphene MOSFETs the following intrinsic transistor formulas apply:

$$f_{T,\text{int}} = g_m / [2\pi(C_{GS} + C_{GD})] \quad (1.49a)$$

$$f_{\max,\text{int}} = (g_m / 4\pi C_{GS}) \times (g_D R_{\text{int}})^{-0.5} \quad (1.49b)$$

while the corresponding extrinsic parameters describe the whole device:

$$f_T = f_{T,\text{int}} [1 + g_D(R_S + R_D) + (C_{GD}g_m(R_S + R_D)/(C_{GS} + C_{GD}))]^{-1} \quad (1.50a)$$

$$f_{\max} = (g_m / 4\pi C_{GS}) [g_D(R_{\text{int}} + R_S + R_G) + g_m R_G (C_{GD}/C_{GS})]^{-0.5} \quad (1.50b)$$

The intrinsic graphene FET represented by the gate region and the graphene channel controlled by the gate in Fig. 1.20, has the following equivalent elements, illustrated in Fig. 1.21: the capacitance between gate and source  $C_{GS}$ , the

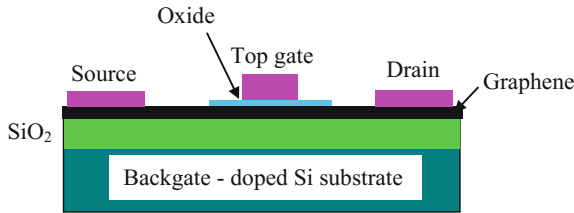


**Fig. 1.20** Graphene MOSFET configuration





with the sheet carrier density  $\rho_{sh}$  as

$$e\rho_{sh} = Q_{sh} = |C_q V_{ch}/2| \quad (1.53)$$

The parameters  $C_q$ , which represents the quantum capacitance, and  $V_{ch}$ , which is the voltage across  $C_q$ , are determined from the system of equations

$$C_q = (2e^2/\pi)e|V_{ch}|/(\hbar v_F)^2 \quad (1.54a)$$

$$V_{ch} = [V_{G-top} - V(x)](C_{ox-top}/C_{ox,eq}) + [V_{G-back} - V(x)](C_{ox-back}/C_{ox,eq}) \quad (1.54b)$$

where  $C_{ox,eq} = C_{ox-top} + C_{ox-back} + C_q/2$ . The system of (1.54a, 1.54b) is derived from the capacitive equivalent circuit of the gate, shown in Fig. 1.22.

Finally, the carrier density sheet can be expressed as

$$n = 2/[\pi(\hbar v_F)^2] \times \int_0^\infty [\exp[(E - E_F)/k_B T] + 1]^{-1} E dE \quad (1.55a)$$

$$p = 2/[\pi(\hbar v_F)^2] \times \int_0^\infty [\exp[(E + E_F)/k_B T] + 1]^{-1} E dE \quad (1.55b)$$

Then,  $C_{GS}$  and  $C_{GD}$  can be computed from this rather simple model, which involves a nonlinear systems of equations.

In graphene MOSFETs with long gate lengths ( $L > 200$  nm) modeled as above,  $f_T$  shows a  $1/L$  dependence and increases as the mobility increases. If the gate length is less than 100 nm, the cutoff frequencies of graphene FETs are very high, around 500–600 GHz, and compete with the fastest transistors ever known, such as InP HEMTs or GaAs mHEMTs. However,  $f_{max}$  of graphene MOSFETs is much lower (tens of GHz) than in InP HEMTs (hundreds of GHz). The degradation of

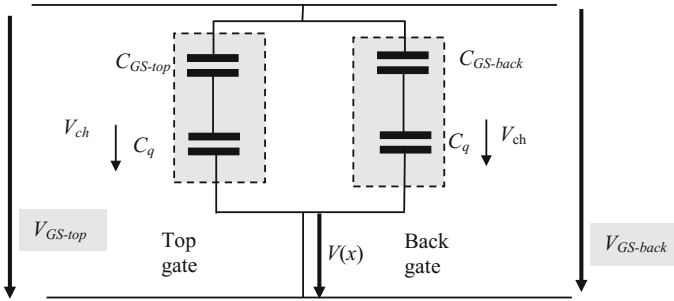


**Fig. 1.22** Gate capacitances and their associated voltages

$f_{\max}$  is caused by the large drain-source conductance, which derives from the fact that saturation is not accomplished in graphene due to the lack of a bandgap. The large source-drain series resistance contributes also to the degradation of power gain and  $f_{\max}$ .

In realistic transistor configurations, the graphene MOSFET has ungated regions between source/drain electrodes and the gate. These regions determine an access resistance, which lowers the drain current and the transconductance. Moreover, the ungated regions favor adsorption of various molecules in ambient conditions, which could degrade the transistor channel during and after processing. Therefore, for enhanced performances it is necessary to reduce to minimum the access region between source/drain and gate, expressed by an access length  $L_A$ . The best method to address the access length problem in a FET is the self-aligned source/drain electrodes technique, illustrated in Fig. 1.23. In this technique, the source and drain electrodes are defined by the gate electrode, which plays the key role in reducing  $L_A$ . The undercut region in the self-aligned transistor, shown in Fig. 1.23b, is obtained via wet-etching, which confers a very small access resistance (Jung et al. 2013). Such self-aligned FETs with a gate length of 3  $\mu\text{m}$  display good performances: mobility of 6100  $\text{cm}^2/\text{V s}$ , normalized contact resistance  $R_c W = 412 \Omega \cdot \mu\text{m}$ , gate leakage currents smaller than 1 nA, and a cutoff frequency of 13 GHz. The transconductance is about one order of magnitude higher than in normal top gate graphene FETs: 114 versus 14  $\mu\text{S}$ .

Better performances are obtained in FETs with sub-100 nm channel length, where the local gate is a highly doped GaN nanowire having an electrical permittivity of 10 (Liao et al. 2010). The transit time in such devices is 120–220 fs, the cutoff frequency varies in the range 700–1400 GHz, and the transconductance is about 2  $\text{mS}/\mu\text{m}$ . The GaN nanowire has a sidewidth of 50–100 nm and a length of 10  $\mu\text{m}$ . The electrical carrier density is about  $n \cong 2 \times 10^{19} \text{ cm}^{-3}$ . This graphene transistor, among the best known up to now, is represented in Fig. 1.24.

As shown in Fig. 1.25, there is a Schottky barrier between the GaN nanowire and graphene, which reduces the leakage current between the graphene channel and the GaN gate. It is worth noting that graphene has Schottky contact with many semiconductors, such as Si and GaAs, this feature being used in various applications.

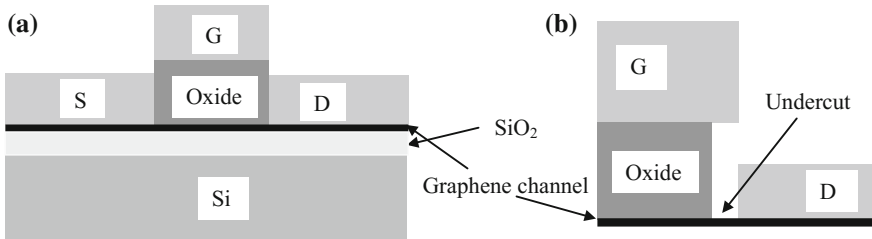


**Fig. 1.23** Self-aligned graphene FET **a** cross section **b** detail in gate region

**Fig. 1.24** Graphene transistor with self-aligned contacts and sub-100 nm gate length

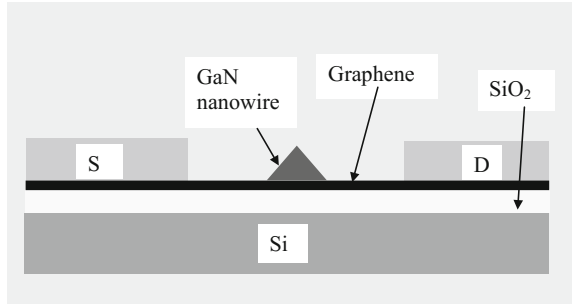
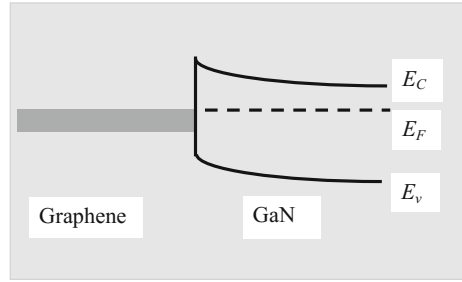


**Fig. 1.25** The graphene-GaN Schottky contact



The graphene FET in Fig. 1.24 displays rather impressive properties, such as a drain current of 10 mA at  $V_D = 1$  V and  $V_G = 0.5$  V. The transconductance peak is  $-4.6$  mS at the same drain voltage, i.e.  $2.3$  mS/ $\mu\text{m}$  considering that the channel has a width of  $2$   $\mu\text{m}$ . This is among the highest transconductances attained in graphene FETs. The current density, of about  $2.3 \times 10^9$  A/cm<sup>2</sup>, is comparable with that in metallic carbon nanotubes and is three orders of magnitude higher than in CMOS transistors with copper electrodes.

The transit time of the transistor is defined as

$$\tau_{tr} = C_{GS}/g_m \quad (1.56)$$

and the intrinsic cutoff frequency is then given by

$$f_T = 1/(2\pi\tau_{tr}) \quad (1.57)$$

Considering that the gate length of the graphene FET is  $L = 90$  nm, we obtain  $\tau_{tr}$  about  $0.19$  ps at  $V_D = 1$  V and a cutoff frequency of  $840$  GHz, meaning that this transistor is 4–5 times faster than a similar Si MOSFET with the same  $L$ , which has a cutoff frequency of only  $200$  GHz. The transit time of graphene FETs for various gate lengths under  $100$  nm is represented in Fig. 1.26, while the cutoff frequency for various gate lengths is displayed in Fig. 1.27. From Fig. 1.27 it follows that for channels shorter than  $70$  nm the cutoff frequencies exceed  $1$  THz.

**Fig. 1.26** The transit time versus channel length dependence in a graphene FET (after Liao et al. 2010)

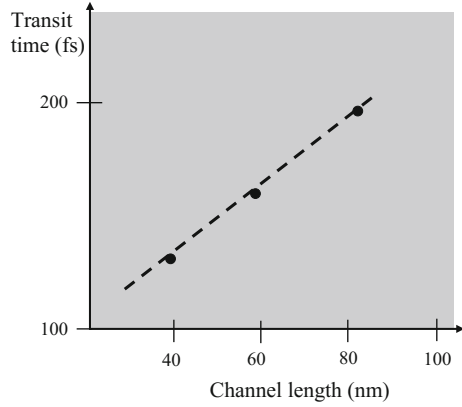
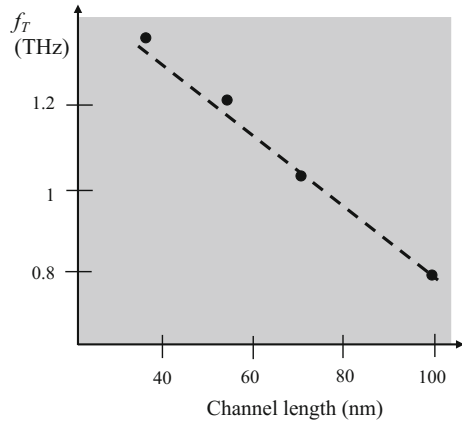


**Fig. 1.27** Cutoff frequency dependence on the channel length in a graphene FET (after Liao et al. 2010)



The transit time can be also expressed as

$$\tau_{tr} = L/v_{drift} \quad (1.58)$$

the intrinsic cutoff frequency becoming then

$$f_T = v_{drift}/2\pi L \quad (1.59)$$

Because the drift velocity is about  $4.3 \times 10^7$  cm/s, the transistor cutoff frequency scales as

$$f_{T,intrinsic} = 70 \text{ GHz}/L (\mu\text{m}) \quad (1.60)$$

High-frequency self-aligned gated transistors work up to millimeterwaves. For example, a self-aligned graphene FET fabricated via transferred gate stacks (Cheng et al. 2012) has a cutoff frequency of 427 GHz. In this case, the gate stacks are

fabricated separately via e-beam patterning and RIE etching, and then transferred on any substrate on which a graphene monolayer acting as a channel is placed. The self-aligned geometry is then followed to obtain low access resistance and parasitic capacitance. The  $f_{\max}$  parameter of the transistor is, however, much lower, attaining 29 GHz for a 220 nm long channel. In this case,  $f_{\max}$  was determined via Mason's unilateral power gain (Cheng et al. 2012), from the relation  $U^{1/2}(f) = 1$  (see Fig. 1.29), where

$$U = [| (S_{21}/S_{12}) - 1 |^2 / 2] / (k_U |S_{21}/S_{12}| - \text{Re}[S_{21}/S_{12}]) \quad (1.61)$$

and

$$k_U = (1 - |S_{11}|^2 - |S_{22}|^2 + |S_{12}S_{22} - S_{21}S_{12}|^2) / (2|S_{12}S_{22}|), \quad (1.62)$$

$S_{ij}$ ,  $i, j = 1, 2$  being the scattering parameters. Figure 1.28 suggests that the highest  $f_{\max}$  is obtained for an optimal gate length, and not the smallest channel length.

One of graphene FET configurations with the most impressive records is that containing an aligned T-gate on the C-face of the SiC substrate. This graphene FET configuration, schematically represented in Fig. 1.29, has  $f_{\max} = 70$  GHz (Guo et al. 2013). This high  $f_{\max}$  value is the result of a high mobility, of  $8700 \text{ cm}^2/\text{V s}$ , and a low contact resistance of the (Ti/Au) electrode,  $R_c < 100 \Omega \mu\text{m}$ . The contact resistance is given by

$$R_c = (1/2)(R_{2p} - R_{\text{channel}}) \quad (1.63)$$

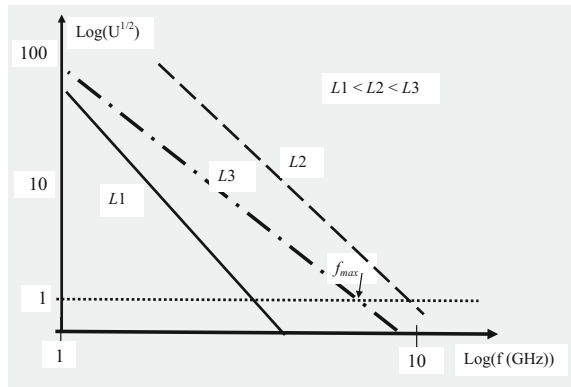
where  $R_{2p}$  is the two-port resistance.

The cutoff frequency of the T-gate graphene FET is 33 GHz for a gate length of 250 nm and about 100 GHz for a gate length of 100 nm.

The extrinsic  $f_{\max}$  is defined by

$$f_{\max} = f_T / (2\sqrt{g_D(R_G + R_{SD}) + 2\pi f_T R_G C_G}) \quad (1.64)$$

**Fig. 1.28** Determination of  $f_{\max}$  for self-aligned graphene FETs with different gate lengths  $L_i$ ,  $i = 1, 2, 3$



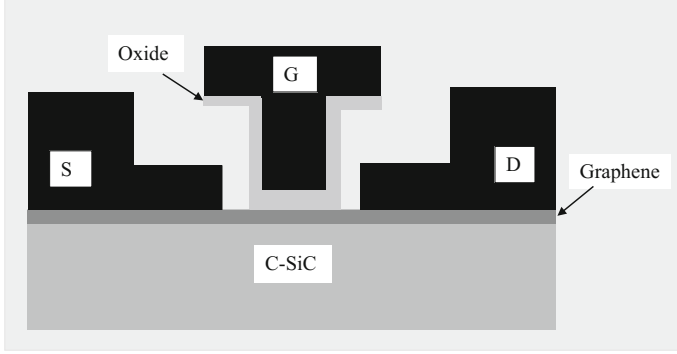


**Fig. 1.29** Graphene FET with self-aligned contacts T-gate

the parameters entering expression (1.64) having the values of  $g_D = 2$  mS, the source-drain access resistance  $R_{SD} = 15 \Omega$ ,  $R_G = 3 \Omega$ , and  $C_G = 5$  pF for the T-gate graphene FET with a 250-nm-long gate. Since in this case the resistance contact is low, we can compute  $f_{\max}$  as

$$f_{\max} = f_T / (2\sqrt{g_D(R_G + R_{SD})}) \quad (1.65)$$

and it is possible to obtain simultaneously high  $f_T$  and  $f_{\max}$ . For instance, multifinger embedded T-shaped gate graphene RF transistors with a high  $f_{\max}/f_T$  ratio were fabricated recently (Han et al. 2013). They have an  $f_{\max}$  of 20 GHz, about 40% higher than  $f_T$ , at a drain bias of 1 V.

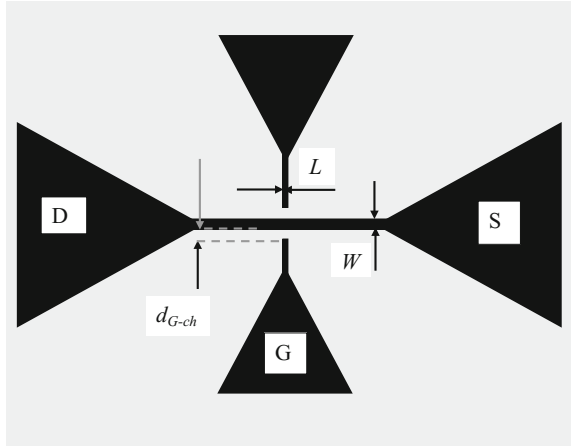
High transconductance values (590 mS/mm) can be obtained using side gate graphene transistors, as that represented in Fig. 1.30, with a lateral gate-channel separation  $d_{G-ch}$  (Hähnlein et al. 2012). In this type of graphene FETs the gate capacitance is determined by the fringing capacitance, given by

$$C_f = (\epsilon_r + 1)\epsilon_0 \sqrt{K(1 - k^2)} / K(k) \quad (1.66)$$

where  $\epsilon_r$  is the dielectric constant of the substrate (SiC for the graphene FET with side gates reported by Hähnlein et al. 2012),  $K(k)$  is the elliptic integral of the first kind with argument  $k = [d_{G-ch}/(d_{G-ch} + W)]^{1/2}$ , where  $W$  is the channel width (see the notations and their significance in Fig. 1.30). The fringing capacitance per unit area is defined as  $C'_f = C_f/(W \times L)$ , and it takes rather small values, of 0.12–0.16  $\mu\text{F}/\text{cm}^2$ , depending on  $d_{G-ch}$  (95–155 nm) and  $W$  (55–67 nm), justifying thus the high transconductance of the side gate graphene FET.

Radio frequency transistors from millimeter-scale graphene monolayer domains of typically hexagonal shape grown by CVD, with  $f_{\max} = 35$  GHz and a cutoff frequency of 178 GHz were reported by (Wei et al. 2014). These graphene FETs, patterned on a Si/SiO<sub>2</sub> substrate, with high resistive Si, have Pd/Au (20/40 nm) source and drain metal contacts, which provide a low contact resistance.

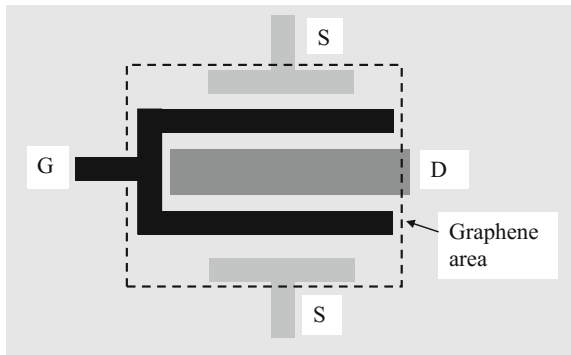
**Fig. 1.30** Graphene FET with lateral gates



The 10 nm-thick  $\text{Al}_2\text{O}_3$  gate dielectric was grown by atomic layer deposition (ALD), which is a standard growth method for all graphene FETs working at high frequencies. Initially, a 2 nm Al layer was pre-deposited on graphene by the e-beam method, in order to improve the interface between  $\text{Al}_2\text{O}_3$  and graphene. The transistor configuration, represented in Fig. 1.31, has a fork-like gate.

In Fig. 1.32 we have illustrated the electrode layout of the graphene FET in coplanar configuration, which is the standard configuration for high-frequency transistors and integrated high-frequency transistors on various circuits, such as amplifiers, oscillators etc. The outer electrodes, i.e. the source electrodes, are grounded in the coplanar configuration, while the central electrode is the signal electrode. In order to exemplify the coplanar graphene FET configuration, Fig. 1.33 presents the SEM image of a graphene FET for high frequencies, which act as a microwave switch (Deligeorgis et al. 2010), while Fig. 1.34 shows the way in which the coplanar electrodes of this type of graphene FET are connected to probe-tips for measurements.

**Fig. 1.31** The graphene FET with a fork-like gate



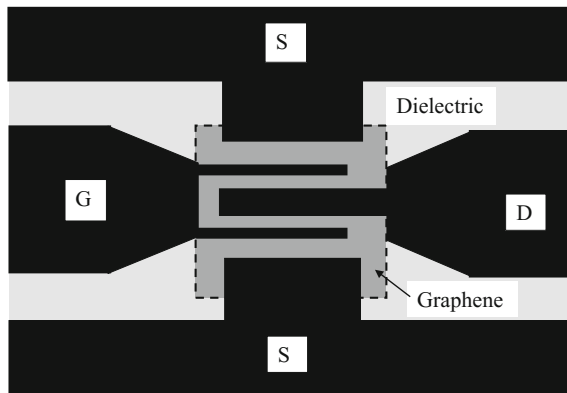


**Fig. 1.32** Coplanar graphene FET electrodes

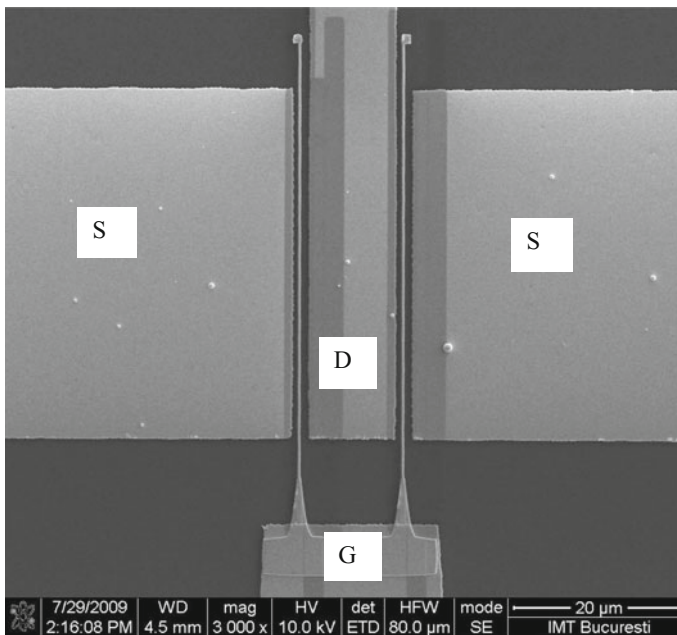


**Fig. 1.33** SEM image of graphene FET with fork-like gate (from Deligeorgis et al. 2010)

In Fig. 1.35 we have represented with dashed line the mobility of a coplanar graphene FET as a function of the drain voltage, when the top gate voltage is zero. From this figure it follows that the peak mobility is of  $9000 \text{ cm}^2/\text{V s}$  at a drain voltage of 3 V while at  $V_D = 4 \text{ V}$  there is a drop in mobility, which corresponds to the position of the Dirac point.



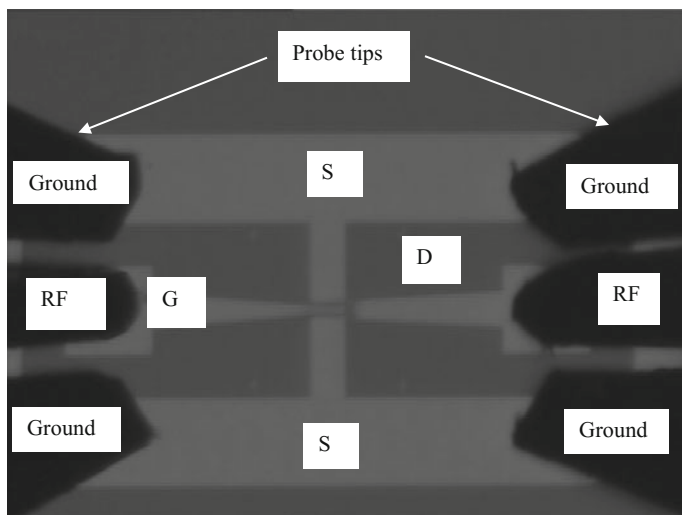
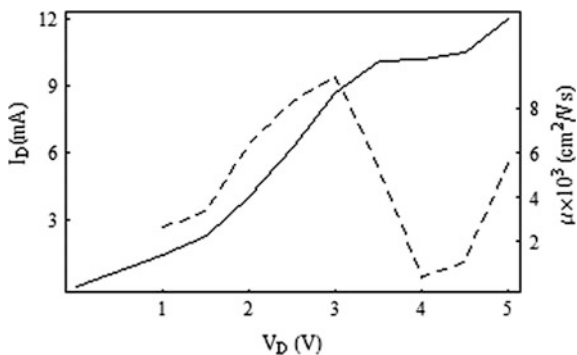


**Fig. 1.34** Graphene FET in a coplanar configuration for RF measurement

**Fig. 1.35** The graphene FET mobility



Batch production of graphene FETs on solid or flexible substrates is performed at 4- and 6-in. wafer scale, 12-in. wafers being expected in few years (Zurutuza and Marinelli 2014). An example of a graphene chip with ballistic graphene FETs is illustrated in Fig. 1.36 (Dragoman et al. 2014a).

The development of graphene FETs on flexible substrates is encouraged by the exceptional mechanical properties of graphene (Lee et al. 2008). In particular, the Young elastic modulus of monolayer graphene is 1 Tpa, conferring to this material a large bending ability, while the breaking strength is 42 N/m, graphene being stronger than steel. In this respect, it was recently demonstrated that multilayer graphene could be used as body armor against bullets (Lee et al. 2014). In addition, stretching of graphene is impressive. The stretching could attain 30% or more in graphene films on PDMS substrates, inducing a change of the sheet resistance by

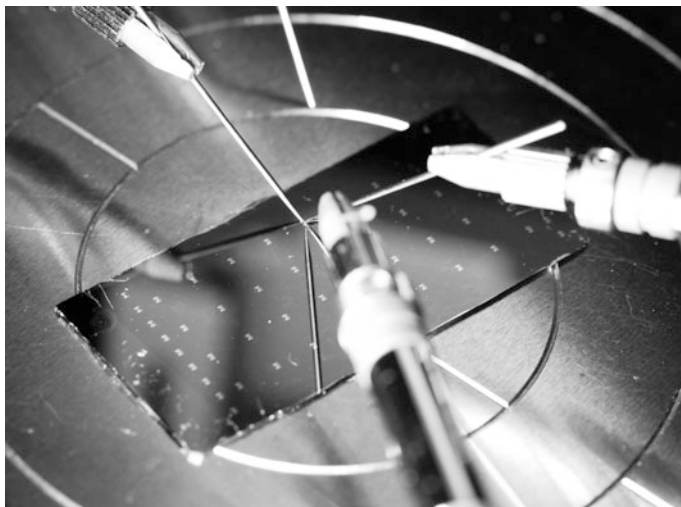
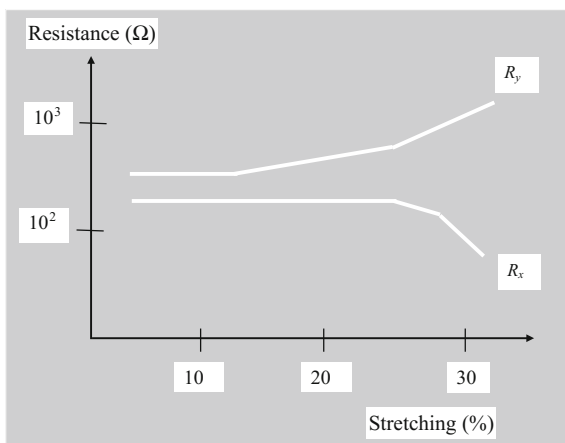


**Fig. 1.36** The graphene FETs on a graphene chip grown by CVD (from Dragoman et al. 2014a)

only one order of magnitude, as can be seen from Fig. 1.37 (Kim et al. 2009), whereas the sheet resistance of ITO increases dramatically after only 2.5% stretching. The stretching in Fig. 1.37 was applied along the  $y$  direction, the PDMS substrate being isotropically stretched by 12% to prevent mechanical failure. Bending and stretching are the two main mechanical properties relevant for graphene FETs on flexible substrates.

There are many types of graphene FETs on flexible substrates (Sharma and Ahn 2013): with commercially available inorganic materials, with ion-gel gate dielectric for printable electronics, and/or with self-healing dielectric gates. Also, the geometry of graphene FETs depends on applications, such as digital electronics, microwave applications or sensors.

**Fig. 1.37** Resistance change due to stretching of a graphene film along the  $y$  direction (after Kim et al. 2009)



A first approach towards flexible FETs is to have a graphene channel, a high dielectric constant oxide, such as  $\text{Al}_2\text{O}_3$ , and a flexible substrate, such as PET (see Fig. 1.38). This is a self-aligned transistor on a plastic substrate, which uses the natural formation of  $\text{Al}_2\text{O}_3$  as gate dielectric (Lu et al. 2012) and the transfer of CVD grown graphene on the PET substrate. The thickness of the oxide is at least 5 nm, and it self-heals at air exposure in a couple of hours when damaged by bending and stretching. In contrast to common gate dielectrics used for graphene FET transistors on solid substrates, such as  $\text{HfO}_2$ , which has a high growth temperature,  $\text{Al}_2\text{O}_3$  in the example above was naturally obtained via air exposure of Al; Al is the top gate of the transistor in Fig. 1.38.

A standard approach for fabricating flexible graphene FETs is to use ion gel liquid and gelating triblock copolymer as gate dielectrics, which have a high capacitance of about  $5 \mu\text{F}/\text{cm}^2$  (Kim et al. 2010). Evidently, such organic-like transistors have low mobility, typical for organic FETs, i.e. lower than  $800 \text{ cm}^2/\text{V s}$  for holes and  $190 \text{ cm}^2/\text{V s}$  for electrons. In particular, the mobilities of the flexible device reported by (Kim et al. 2010) are about  $200 \text{ cm}^2/\text{V s}$  for holes and  $90 \text{ cm}^2/\text{V s}$  for electrons. On PET substrate, the mobility of flexible graphene FETs does not change its value by more than 20% for a bending radius varying with an order of magnitude, from 6 to 0.6 cm (see Fig. 1.39, where  $\mu_0$  is the mobility for a straight substrate). Besides mobility, the on-current of the flexible graphene FET does not show significant difference when the substrate is considerably bent.

Graphene FETs on flexible substrates display excellent performances when working as RF FETs. For example, in a bottom gate configuration, as that illustrated in Fig. 1.40, the extrinsic  $f_{\text{max}}$  reaches a maximum of 3.7 GHz while the cutoff frequency is 10.7 GHz for a strain value of 1.25% (Petrone et al. 2012), the corresponding values for a straight surface being 7.2 and 2.6 GHz. In this case, the oxide is 6 nm thick and was deposited by ALD at  $150^\circ\text{C}$  on a PEN substrate. Both  $f_{\text{max}}$  and  $f_T$  are not degraded significantly up to the strain limit of 1.75%, while the mobility of the graphene FET is about  $1500 \text{ cm}^2/\text{V s}$ .

High cutoff frequencies of 25 GHz can be obtained in a multifinger embedded-gate FET fabricated on a  $100\text{-}\mu\text{m}$ -thick polyimide (PI) film using as gate dielectric  $\text{Al}_2\text{O}_3$  with a thickness of 10 nm deposited by ALD (Lee et al. 2013). The graphene channel length of this graphene FET is 500 nm and its width is  $100 \mu\text{m}$ , the mobility for holes and electrons being 2800 and  $3900 \text{ cm}^2/\text{V s}$ , respectively.

**Fig. 1.38** Flexible graphene transistor with inorganic drain, source and gate

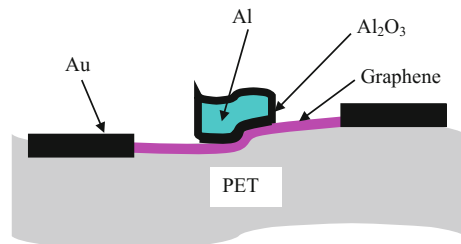


**Fig. 1.39** Typical mobility-bending dependence for flexible graphene FETs

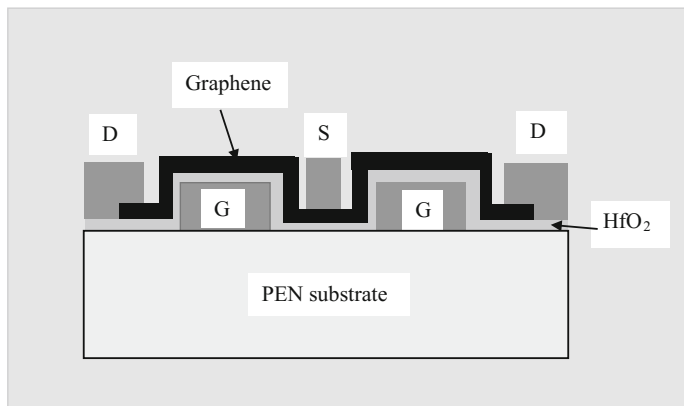
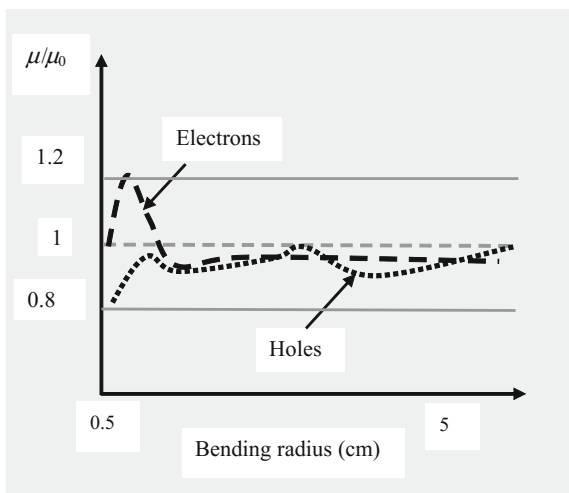


**Fig. 1.40** Microwave FET on PEN substrate

The device has unchanged performances up to a bending radius of 0.7 mm, corresponding to 8.6% strain. The tensile strain is given by

$$\varepsilon = t/(2R_B) \quad (1.67)$$

where  $t$  is the substrate thickness and  $R_B$  is the bending radius.

Flexible integrated circuits on a PET substrate, such as a low-noise amplifier or a mixer, were obtained recently at an extrinsic cutoff frequency of 32 GHz and  $f_{\max} = 20$  GHz (Yeh et al. 2014). In this case, the flexible self-aligned graphene FET is based on a core-shell Al/AIO<sub>x</sub> T-shape top gate (see Fig. 1.41). The main parameters of the transistor are preserved when stretched up to 2.5%.

**Fig. 1.41** T-shaped gate self-aligned graphene FET on PET substrate

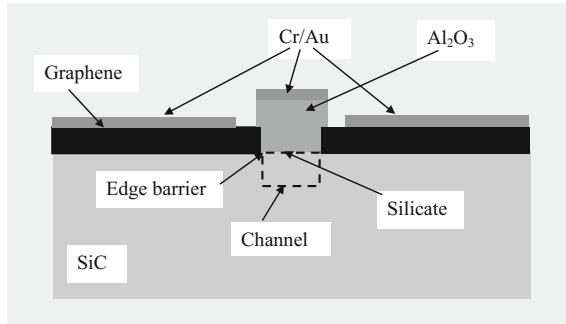
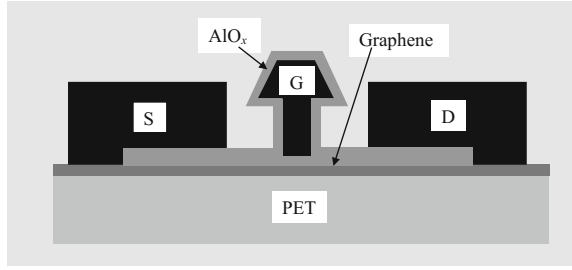


**Fig. 1.42** Graphene transistor with planar edge Schottky barrier-tunneling

The ultimate performances of graphene FETs are expected from tunneling and ballistic FETs. An example of a tunneling transistor is a planar graphene/SiC FET developed for a superior on-off ratio. In this case, the flow current is horizontal over the one-dimensional tunneling barrier between multilayer epitaxial graphene, which acts as planar source and drain contacts, and the coplanar two-dimensional SiC channel (Kunc et al. 2014). The channel is an accumulation layer located at the SiC/surface silicate interface generated by high vacuum annealing, as shown in Fig. 1.42. The SiC accumulation layer and the graphene edge form a Schottky barrier, such that the equivalent circuit of the transistor consists of two back-to-back Schottky diodes controlled by the gate voltage.

At low temperatures the current is determined by tunneling, while at high temperatures the thermionic emission mechanism of the Schottky diode prevails. The drain current versus drain voltage dependence associated to thermionic emission is given by

$$I = A^* T^{3/2} W \exp(-e\phi_B/k_B T) \exp(eV/nk_B T) [1 - \exp(-eV/k_B T)] \quad (1.68)$$

where  $A^* = 0.35 \text{ A/mK}^{-3/2}$  at room temperature and the effective barrier height  $\phi_B$  varies between 0.8 and 0.25 eV when the gate voltage changes in the range (−4 V, 4 V). In the same gate voltage variation interval, the ideality factor  $n$  takes values

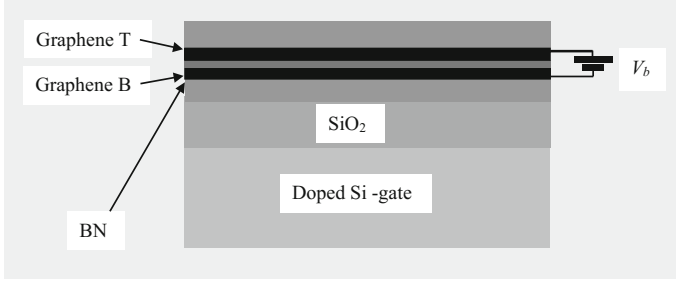


**Fig. 1.43** The vertical tunneling graphene transistor

between 1.1 and 1.5. The on-off ratio reaches  $5 \times 10^6$ , the low mobility, of  $10\text{--}20 \text{ cm}^2/\text{V s}$ , being limited by the doped SiC substrate.

Another graphene tunneling transistor is a graphene/h-BN/graphene or graphene/MoS<sub>2</sub>/graphene configuration, where one or few atomic layers of hexagonal boron nitride or molybdenum disulfide act as barriers while graphene are used as electrodes. This is a MIM (metal-insulator-metal) configuration in the case of h-BN since the bandgap of this material is 6 eV and is a MSM (metal-semiconductor-metal) configuration in the case of MoS<sub>2</sub>, the bandgap of which is 1.9 eV. The graphene tunneling transistor is depicted in Fig. 1.43.

The vertical tunneling graphene FET is based on two high-quality graphene contacts, denoted as graphene T and graphene B in Fig. 1.43, encapsulated in h-BN with a thickness of 20 nm, and surrounding a 1 nm h-BN insulator layer, through which tunneling takes place. The entire structure is a tunable MIM diode with a backgate. As a result, the drain current versus drain voltage dependence is similar to a current-voltage characteristic of a diode tunable via the gate voltage, as that represented in Fig. 1.44. A high on-off ratio of 50 can be obtained in such transistors (Britnell et al. 2012). The on-off ratio reaches  $10^5$  if h-BN is replaced by MoS<sub>2</sub> in a similar vertical tunneling FET.

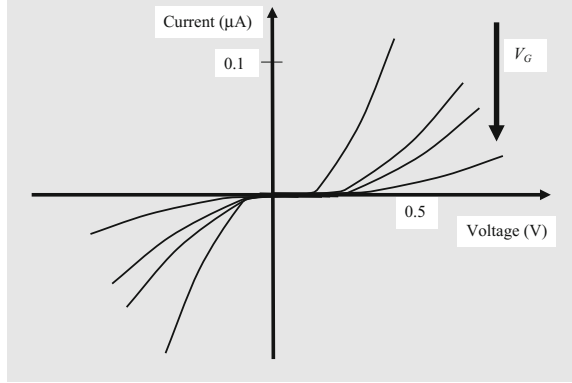
In the vertical tunneling graphene FET configuration, the applied electric field (in modulus) on the barrier and gate regions are given, respectively, by (Ponomarenko et al. 2013)

$$|F_b| = n_T e / \epsilon_0 \epsilon_r \quad (1.69a)$$

$$|F_G| = (n_B + n_T) e / \epsilon_0 \epsilon_r \quad (1.69b)$$

where  $n_B$  and  $n_T$  are the induced carrier densities at the two graphene electrodes and  $\epsilon_r$  is the relative electrical permittivity of SiO<sub>2</sub> and h-BN, as both materials have similar dielectric constants.

**Fig. 1.44** Typical current-voltage dependence on gate voltage in a tunneling transistor



Then, the voltage between the graphene electrodes can be expressed as

$$eV_b = eF_b d - \mu(n_T) - \mu(n_B) \quad (1.70)$$

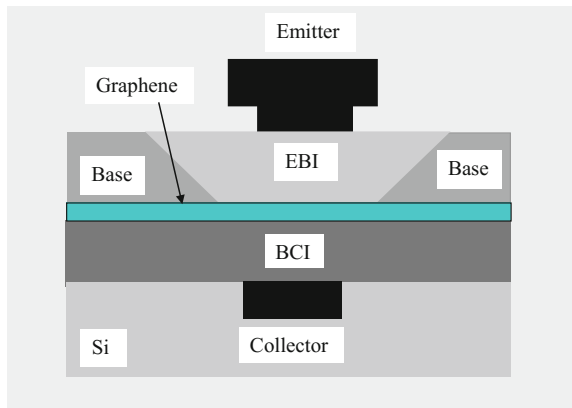
where  $d$  is the thickness of the h-BN barrier and  $\mu_c(n_{T,B})$  are the chemical potentials of the corresponding graphene electrodes. The sheet density  $n_T$  under the simplified assumptions that  $n_T = n_B = 0$  when no electric fields are applied and that  $\mu_c(-n) = -\mu_c(n)$  can be derived from

$$e^2 dn_T / \epsilon_0 \epsilon_r + \mu_c(n_T + \epsilon_0 \epsilon_r E_g / e) + eV_b = 0 \quad (1.71)$$

The Landauer formula can now be used to find the current-voltage dependence.

Among other configurations of graphene FETs we mention here the vertical graphene base heterojunction transistor, which is expected to work at THz frequencies (Mehr et al. 2012). In this type of tunneling transistor, represented in Fig. 1.45, graphene is used as base control electrode for ballistic transport. In the on

**Fig. 1.45** Graphene base transistor



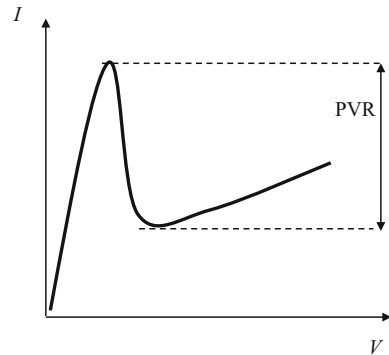
state, charge carriers tunnel through the emitter-base insulator layer, denoted by EBI in Fig. 1.45, the graphene layer, and into the conduction band of the base-collector insulator, denoted by BCI. Graphene tunes the EBI barrier via an applied electron-base voltage. For a positive bias, the transistor is in the on state, while when no electron-base voltage is applied the device is in the off state, the high EBI barrier preventing current flow.

Many graphene transistors display negative differential resistance (NDR) regions. In a NDR the current decreases abruptly as the voltage increases, the current-voltage dependence having a shape similar to the letters S or N. The last shape is the most common one and is illustrated in Fig. 1.46. Such nonlinear current-voltage dependence is used in oscillators to generate oscillations at a certain frequency, but also for multiplication or detection purposes.

NDR was observed in graphene/h-BN/graphene tunneling transistors, where the carriers tunnel through the h-BN insulator. The vertical graphene/h-BN/graphene structure is deposited over  $\text{SiO}_2/\text{doped Si}$ , the Si layer acting as backgate. In this case the NDR shape can be tuned by the backgate voltage. However, the peak-to-valley ratio (PVR), i.e. the ratio between the maximum and minimum currents in the NDR region, was relative small, reaching values between 2 and 4 (Britnell et al. 2013). On the contrary, the NDR effect with a PVR of 28 was observed in dual-gate graphene FETs, if  $V_D$  and  $V_{TG}$  are swept simultaneously (Liu et al. 2013). The origin of the NDR was elucidated in (Sharma et al. 2015), as the result of the competition between the field dependence of the carrier density and the drift velocity.

This is not, however, the only mechanism for generating NDR. In ballistic graphene FETs with oblique gates (Dragoman et al. 2014a), the NDR is due to an abrupt drop to zero of the transmission coefficient of carriers over a certain range of drain voltage values,  $V_D$ . This decrease in transmission produces a minimum in the  $I_D - V_D$  dependence, the drain current  $I_D$  being determined by the transmission coefficient via the Landauer formula. A bias applied on the oblique gate of the ballistic graphene FET can shift the NDR region of the  $I_D - V_D$  dependence, shown in Fig. 1.47, and can affect the PVR of the device; this latter parameter can be tuned up 9.

**Fig. 1.46** Typical current-voltage dependence with negative differential resistance





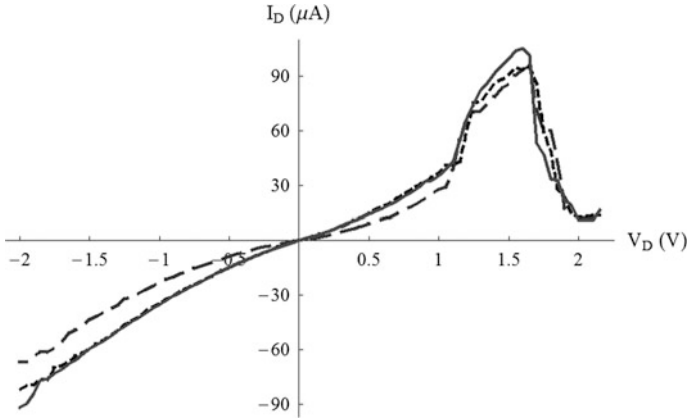


**Fig. 1.47** NDR behavior in the ballistic regime of the graphene FET with oblique gate at  $V_{TG} = 0$  V (dashed line), 0.5 V (dotted line) and 1 V (solid line) (from Dragoman et al. 2014a)

### 1.2.2 Graphene Diodes

Graphene diodes are important electronic devices, graphene widening in many ways our concepts about diodes. Diodes based on  $p$ - $n$  junctions created by doping the host material with acceptor and donor impurities are widespread in semiconductor technology. However, it is difficult to dope graphene with impurities because some electrical properties degrade. Instead, electrical doping can be used since in graphene the carrier density and their type are modulated by a gate voltage. If the gate voltage is positive, the charge carriers are of  $n$  type, while  $p$  type carriers are generated by negative gate voltages.

An example of a  $p$ - $n$  diode (Sutar et al. 2012) in graphene is presented in Fig. 1.48. The  $p$  and  $n$  junctions are induced by the two buried gates, made from highly doped poly-Si, and having the shape of interdigitated fingers. The diode electrodes are tilted at a certain angle since, as pointed out several times, this geometry modulates the transmission in the ballistic regime (Dragoman and Dragoman 2007a). Using suitably applied biases on the gates, all possible doping combinations, i.e.  $n$ - $n$ ,  $p$ - $p$ ,  $p$ - $n$  and  $n$ - $p$ , can be obtained, this versatility being impossible to be achieved in a semiconductor diode with fixed doping concentrations.

By changing the angle of incidence in this graphene diode from  $0^\circ$  to  $30^\circ$  and then to  $45^\circ$ , the mobility changes from  $2300$  to  $2960$   $\text{cm}^2/\text{V s}$ , and up to  $3400$   $\text{cm}^2/\text{V s}$  in various devices with the distance between gates of  $150$  and  $200$  nm, both values being smaller than the mean-free-path in graphene at room temperature. Moreover, as can be seen from Fig. 1.49, as the tilt angle increases the diode resistance is modulated by more than  $100\%$ , from  $1$  up to  $2.5$  k $\Omega$ , at  $V_b = V_{G1} - V_{Dirac} = -(V_{G2} - V_{Dirac}) = 5$  V and, when the tilting angle is  $45^\circ$  the diode displays a particular behavior, illustrated in Fig. 1.50. At this tilting angle, as the bias voltage is varied in the interval  $(-20$  V,  $20$  V), the resistance varies and

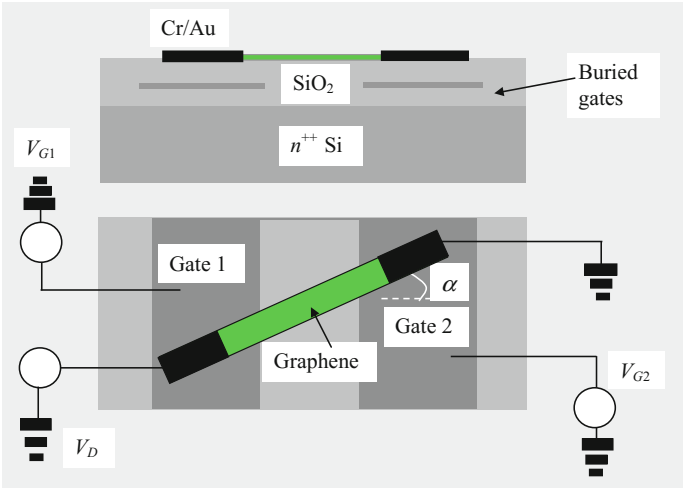


**Fig. 1.48** Tilted angle *p-n* graphene junction: side view (*top*) and top view (*bottom*)

**Fig. 1.49** Diode resistance as a function of the tilting angle of electrodes

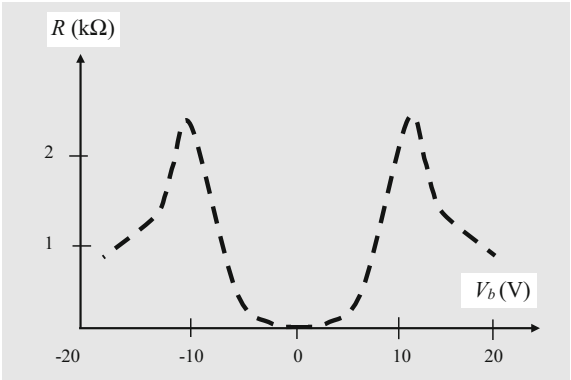
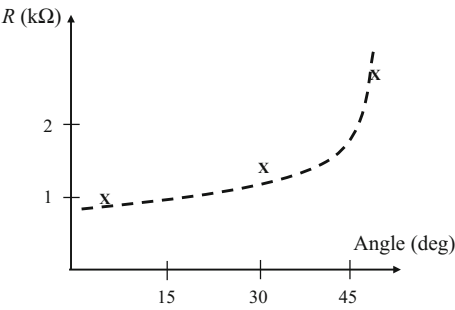


**Fig. 1.50** Metal-insulator transition in the tilted graphene diode

attains a maximum value of about  $2.5 \text{ k}\Omega$ . More precisely, the diode is in a low resistance state near  $V_b = 0 \text{ V}$ , in which it behaves as a metal, and then jumps to a high resistance state at about  $\pm 10 \text{ V}$ , in which it becomes an insulator. The on-off ratio is  $2.5 \times 10^3$ .

One of the most interesting graphene diodes is that resulting from the simple contact of graphene with most well known doped semiconductors, such as  $n$ -type Si, GaAs, 4H-SiC, and GaN. A Schottky contact forms between graphene and these semiconductors, and the charge transfer between the two materials changes the Fermi level. The first graphene-semiconductor diodes were fabricated via the transfer method, i.e. CVD grown graphene flakes were transferred on Si, GaAs, 4H-SiC, and GaN, all of  $n$ -type (Tongay et al. 2012). A typical configuration of a graphene-semiconductor diode is represented in Fig. 1.51. The graphene contacting areas are squares, with sides in the  $500\text{--}2000 \text{ }\mu\text{m}$  range. Ohmic contacts are first grown on semiconductors, then a  $500\text{--}1000 \text{ nm}$  thick  $\text{SiO}_2$  window is grown over the semiconductor followed by gold deposition with a thickness of  $500 \text{ nm}$ . Graphene makes contact with both metal (Au) and semiconductor, showing strong rectification.

The dependence of the current density  $J(T, V) = I(T, V)/A$  on temperature  $T$  and voltage  $V$  in the graphene-semiconductor diode with contact area  $A$ , through which a current  $I(T, V)$  flows, is determined by thermionic emission above the Schottky barrier, and is given by

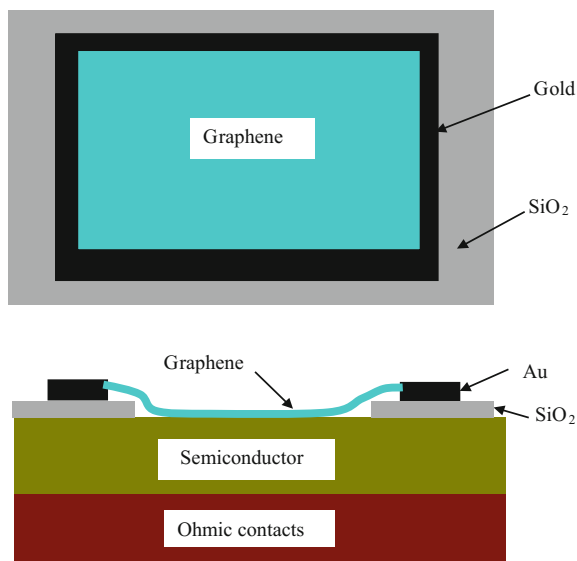


**Fig. 1.51** Graphene-semiconductor diode: top view (*top*) and side view (*bottom*)

$$J(T, V) = J_s(T)[\exp(eV/\eta k_B T) - 1] \quad (1.72a)$$

where  $\eta$  is the ideality factor, and

$$J_s(T) = A^* T^2 \exp(-e\phi_{SBH}/k_B T) \quad (1.72b)$$

is the saturation current dependent on the zero-bias Schottky barrier height (SBH)  $e\phi_{SBH}$  and the Richardson constant  $A^*$ . The ideality factor ranges between 1.2 and 5, having no association with the type of semiconductor. The imprint of the thermionic process is the linearity of the  $\log(J) - V$  dependences at different  $T$  values at forward bias, as well as the linearity of the dependence  $\log(J_s(T)/T^2)$  on  $1/T$ . From the first dependence it is possible to extract the parameters  $J_s$  and  $\eta$ , while from the slope of the latter curve it is possible to determine  $e\phi_{SBH}$ . The graphene workfunction and SBH values at different junctions are listed in Table 1.4 (Tongay et al. 2012).

Schottky barriers are described by two limits: (i) Bardeen and (ii) Schottky-Mott. In the first case, the Schottky contact is fully determined by the interface states, which pin the Fermi level of the semiconductor via charge accumulation. As a result, the dependence of the barrier on the type of metal contacts is weak. The Bardeen limit is valid in the case of the graphene/GaAs diode. On the other hand, the Schottky-Mott limit is applicable for the rest of graphene/semiconductor diodes. In this case, the Schottky barrier height is given by

$$\phi_{SBH} = \Phi_{gr} - \chi_e \quad (1.73)$$

where  $\Phi_{gr}$  is the graphene workfunction and  $\chi_e$  is the electron affinity of the semiconducting material.

Consequently, knowing the electron affinity for Si (4.05 eV), 4H-SiC (3.4 eV) and GaN (4.1 eV), the work function of graphene can be determined as a function of the device fabrication conditions. The graphene workfunction reference is 4.6 eV when the Fermi level  $E_F$  is at the Dirac point. However, this value could differ slightly, with  $\pm 0.3$  eV depending on the semiconductor, due to doping of graphene during the transfer process, as indicated in Table 1.4.

**Table 1.4** Graphene/semiconductor Schottky barrier heights

Junction	Graphene workfunction (eV) ( $E_F$ at Dirac point)	Schottky barrier height (eV)	Graphene workfunction (eV) due to doping
Graphene/ <i>n</i> -GaAs	4.6	0.79	4.89
Graphene/ <i>n</i> -GaN	4.6	0.73	4.83
Graphene/ <i>n</i> -Si	4.6	0.86	4.91
Graphene/ <i>n</i> -4H-SiC	4.6	0.91	4.31

Another bilayer graphene-Si (*n*- or *p*-type) diode configuration contains the Si/SiO<sub>2</sub>/Si<sub>3</sub>N<sub>4</sub>/Cr/Au heterostructure depicted in Fig. 1.52 (Chen et al. 2011a). Although bilayer graphene is able to make Schottky contact with either *n*- or *p*-type Si, there are differences between these two types of diodes: (i) the graphene/*n*-Si diode is turning on at a positive voltage, while the graphene/*p*-Si diode is turning on at a negative voltage, due to the different types of carriers in the substrate, and (ii) the photocurrents are more pronounced (3–4 times higher) in the graphene/*p*-Si diode than in the graphene/*n*-Si diode at the same laser illumination power of 30 mW and at 532 nm wavelength, due to a larger space charge region.

For the graphene diode in Fig. 1.52, the Schottky barrier height is given by

$$\phi_{SBH} = (k_B T / e) \ln(A^* T^2 / J_s) \quad (1.74)$$

and is equal to 0.41–0.42 eV for the bilayer graphene/*n*-Si diode and 0.44–0.46 eV for the bilayer graphene/*p*-Si diode. The ideality factor at room temperature ranges from 4.8 for the first diode type (with an *n*-Si substrate) up to 33 for the second one (with a *p*-Si substrate). However, there are almost ideal graphene/silicon Schottky diodes, which have an ideality factor of about 1.08 (Sinha and Lee 2014). To achieve such a low ideality factor in diodes in which graphene is grown by the LPCVD technique on Cu, it is necessary to etch the top 700 nm of Cu during 90s using ammonium persulfate (APS). This procedure has the role of reducing the metallic impurities in graphene. Then, graphene is transferred on the Si/SiO<sub>2</sub> substrate and contacted with Cr/Au contacts.

The graphene/*n*-GaN diode, depicted in Fig. 1.53, preserves the rectifying behavior up to 550 K, and becomes nonrectifying after 650 K. In this case GaN was *n*-doped with Si, the carrier concentration attaining 10<sup>16</sup> cm<sup>-3</sup>. After cooling, the diode shows improved rectification characteristics (Tongay et al. 2011). This extraordinary stability is due to the thermal properties of graphene, temperatures as high as 900 K being not sufficient to break the carbon-carbon bonds. The Schottky barrier height is in this case of 0.74 eV and the ideality factor is 2.9, the values of these parameters after annealing becoming 0.7 eV and 2.4, respectively.

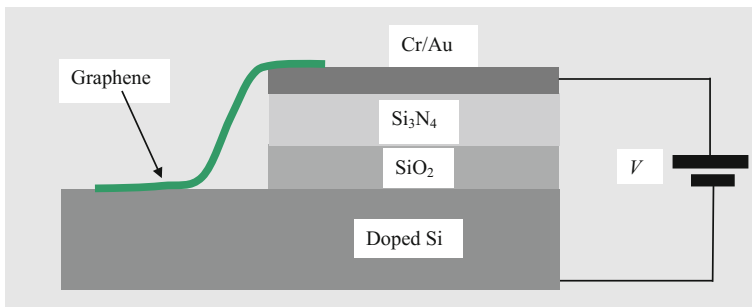


**Fig. 1.52** The bilayer graphene/Si/SiO<sub>2</sub>/Si<sub>3</sub>N<sub>4</sub>/Cr/Au diode

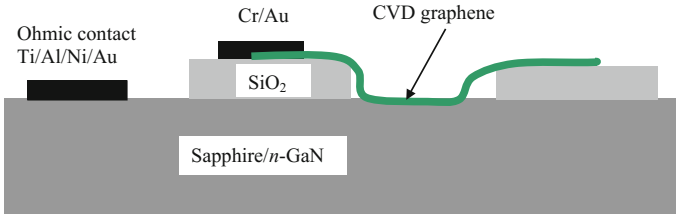
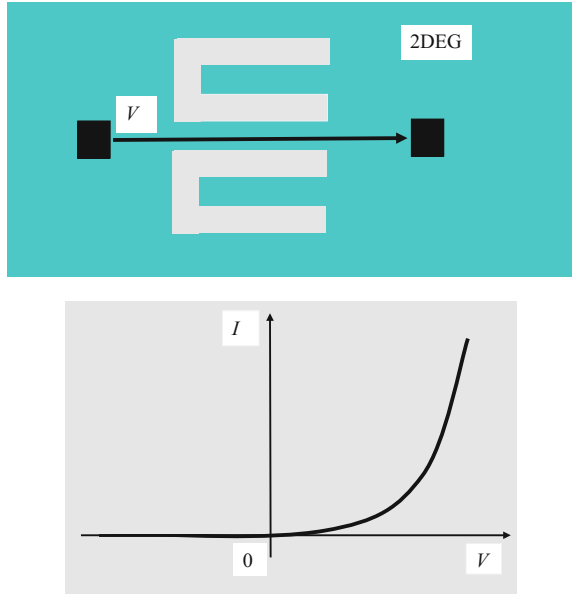


**Fig. 1.53** The graphene/*n*-GaN diode

The graphene diodes presented above have DC characteristics that can be changed under the influence of various adsorbates, such as liquids and gases. Thus, chemically modulated graphene diodes can act as sensors even at elevated temperatures (Kim et al. 2013b).

Another type of graphene diodes is the self-switching diode, fabricated by carving the boundaries of a graphene strip in order to break its symmetry. This configuration is a particular example of self-switching diodes, known for more than 10 years and applied initially to 2DEG materials such as InGaAs/InAlAs (Song et al. 2003). The extension of this diode configuration to graphene is motivated by the fact that graphene is a native 2D material. A schematic representation of this diode type and its  $I$ - $V$  characteristic are illustrated in Fig. 1.54. The self-switching diode was analyzed in several papers as a possible NDR device, but no experimental evidence of this effect was found. The voltage  $V$ , depending on its sign, widens or narrows the effective channel width in the 2DEG.

**Fig. 1.54** Self-switching diode configuration in 2DEG (*top*) and its  $I$ - $V$  characteristic (*bottom*)



The self-switching diode is able to detect THz signals (Balocco et al. 2008). For high-frequency detection, the voltage across the diode can be modelled as

$$V = V_0 + v_0 \cos(\omega t) \quad (1.75)$$

where  $V_0$  is the applied DC bias, and  $v_0$  is the amplitude of the modulating signal with frequency  $f = \omega/2\pi$ . The current can then be expanded in a Taylor series as

$$I = I_0 + v_0 G_d \cos \omega t + v_0^2 G_d' \cos^2 \omega t + \dots = I_0 + (v_0^2/2) G_d' \cos \omega t + (v_0^2/4) G_d' \cos 2\omega t + \dots \quad (1.76)$$

where  $I_0$  is the bias current,  $G_d = dI/dV|_{V=V_0}$  denotes the differential conductance and  $G_d' = d^2I/dV^2|_{V=V_0}$ . The rectified DC current is then given by

$$I_r \propto (v_0^2/4) G_d' \quad (1.77)$$

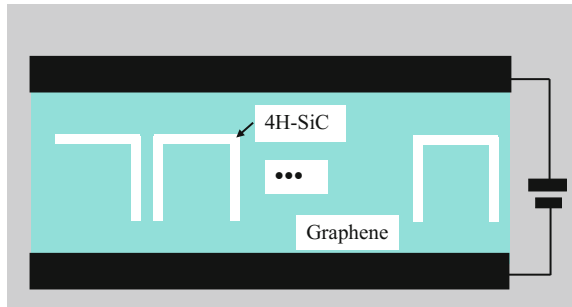
and, in an open-circuit configuration, the detected voltage can be written as

$$\beta_V = (v_0^2/4) G_d' / G_d \quad (1.78)$$

Graphene self-switching diodes used as zero-bias microwave detectors were recently fabricated on graphene epitaxially grown on SiC (Westlund et al. 2015). Since the graphene channel is analogous to a lateral nanowire transistor, nine graphene channels in parallel were used to reduce the resistance and the noise-equivalent power (NEP), which is 2.2 nW/Hz<sup>1/2</sup> (see Fig. 1.55). The responsivity of the diode is 3.9 V/W, and detects signals from 1 to 67 GHz.

Another type of graphene diodes is the ballistic diode. A schematic representation of a ballistic Schottky diode is shown in Fig. 1.56 (Dragoman et al. 2010). It consists of two electrodes separated by a distance  $L$ , which must be less than the mean-free-path of carriers in graphene at room temperature, and an oblique gate with tilting angle  $\theta$  placed between the two diode terminals. This device is similar to the recently fabricated ballistic transistor with an oblique gate described above in this chapter. A gate voltage  $V_G$  has the role of modulating the transmission coefficient  $T$  in graphene, which is less than 1 only at oblique incidence, as can be seen

**Fig. 1.55** Graphene self-switching diode RF detector



from the three curves in Fig. 1.57 corresponding to three different gate inclinations. The transmission coefficient can be calculated based on the quantum mechanical transmission-matrix approach detailed in (Dragoman and Dragoman 2007a).

Once  $T$  is known, the Landauer formula is used to compute the rectifying  $I$ - $V$  dependences. Typical current-voltage curves corresponding to three operating points (the origin of  $V$ ) chosen at 0.19 eV (solid-line), 0.29 eV (dotted-line) and 0.38 eV (dashed-line) are represented in Fig. 1.58. All three current-voltage dependences for positive applied biases can be fitted at room temperature with  $I = I_S[\exp(eV/nk_B T) - 1]$ . The fitting results are given in Table 1.5. Considering the Fermi velocity as  $v_F = 10^6$  m/s, the traversal time between the electrodes is  $t = L/v_F = 250$  fs, the resulting cutoff frequency being  $f_T = 1/t = 4$  THz.

From the ballistic graphene Schottky diode example it follows that there are no reverse currents, as in the case of the semiconductor Schottky diode, and that the ideality factor of this device can be tuned up to the optimal value, equal to 1, by changing the tilting angle of the gate. What is the significance of  $n < 1$ ? Such a value is not encountered in common semiconductors, where the Schottky rectification effect is linked to the potential energy barrier at the interface between two

**Fig. 1.56** Ballistic graphene Schottky diode

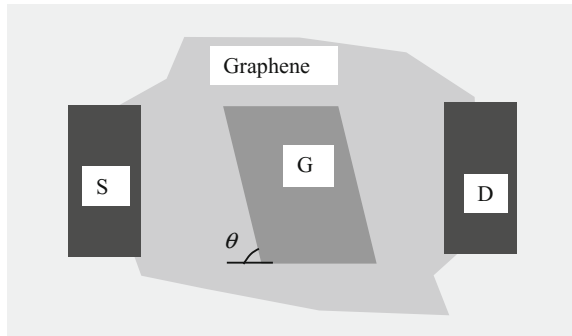


**Fig. 1.57** The transmission at three gate inclination angles 20° (solid line), 30° (dotted line) and 40° (dashed line) (from Dragoman et al. 2010)

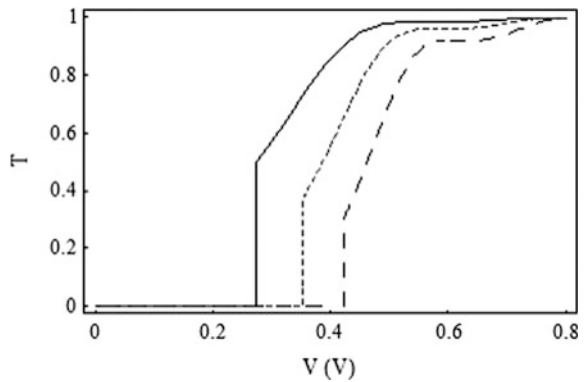




**Fig. 1.58** The current-voltage dependence (from Dragoman et al. 2010)

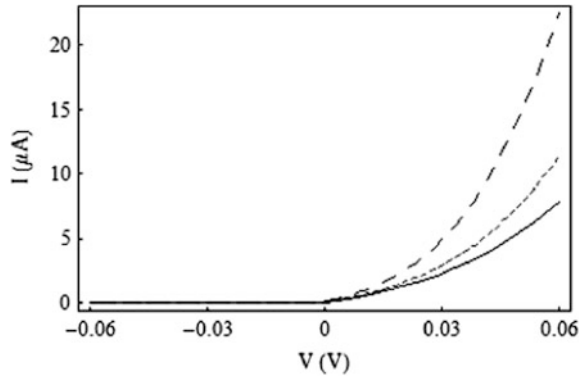


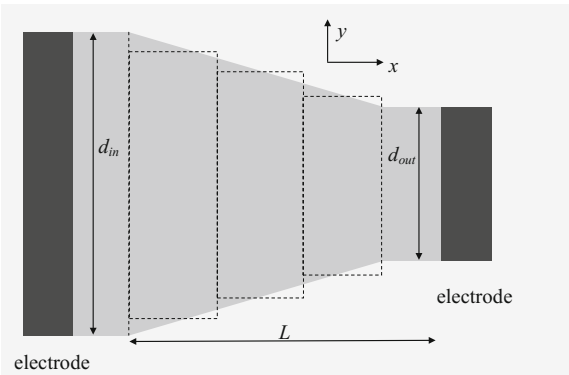
**Table 1.5** The schottky fitting values

Incident angle $\theta$ (°)	$I_S$ ( $\mu A$ )	$n$
20	1.49	1.25
30	1.35	1.02
40	1.7	0.86

materials. In graphene, however, the mechanism is different: the rectification is the result of the lack of a bandgap in the energy dispersion relation.

Another type of rectifying ballistic diode is the geometric diode depicted in Fig. 1.59. The current-voltage dependence of this graphene diode is based also on the Landauer formula (Dragoman and Dragoman 2013). In order to compute the transmission coefficient, the diode is sectioned in a series of thin regions with a constant width, as indicated in Fig. 1.59. Then, the Dirac equation is solved in each region by imposing continuity conditions at the boundaries. It is found that the geometric diode has a certain region of width  $\pi\hbar v_F/d_{out}$  where the transmission coefficient vanishes and thus the current is negligible. The current-voltage dependence of this diode is dependent on the Fermi energy, which can be tuned by a gate voltage.

**Fig. 1.59** The graphene geometric diode (from Dragoman and Dragoman 2013)



The SEM image of the diode, as well as the graphene wafer with diodes, are shown in Fig. 1.60a, b. The diode was fabricated on a 4-in. graphene wafer (Dragoman et al. 2014b), the diodes having a length of 100 nm, a shoulder  $d_{in} = 100$  nm and a neck ( $d_{out}$ ) of only 30 nm. The fabrication of the diodes involved the following steps: (i) e-beam lithography patterning of the regions without graphene monolayers, (ii) PMMA deposition, (iii) patterning of the graphene shapes with an e-beam, (iv) RIE equipment to cut the graphene in trapezoidal

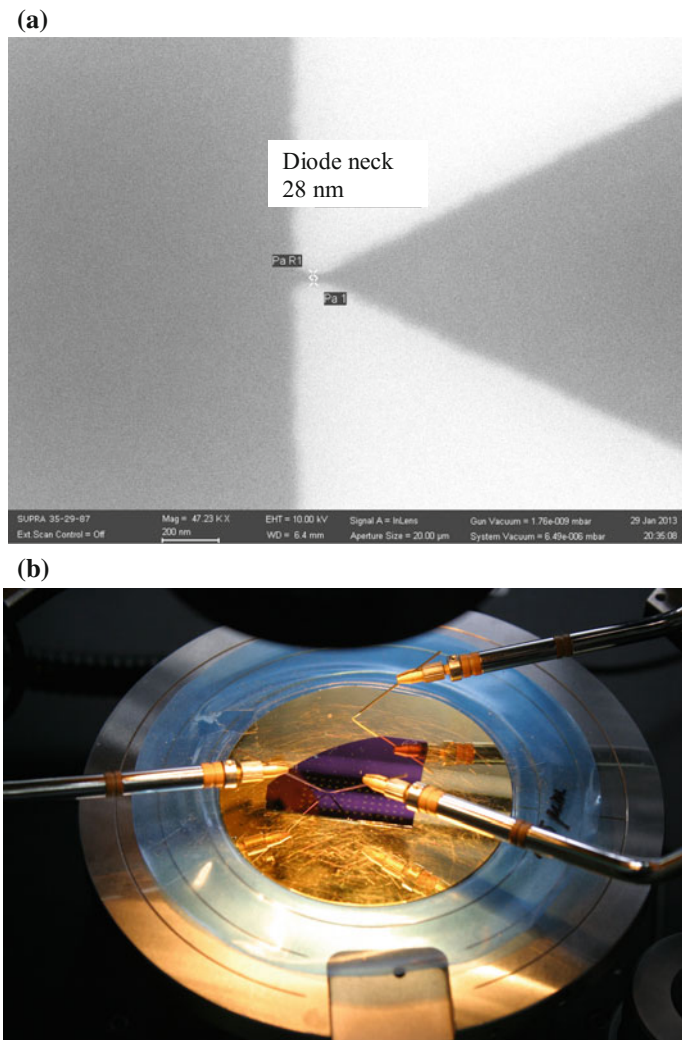


**Fig. 1.60** **a** SEM of the diode and **b** the graphene wafer with geometric diodes (from Dragoman et al. 2014b)

shapes, (v) PMMA coating and e-beam lithography of metallic contacts via an e-gun evaporation chamber.

Experiments have shown that geometric diodes are able to rectify up to even 28 THz, and potentially at optical frequencies (Zhu et al. 2013b). Geometric diodes can be used as rectennas, i.e. antennas integrated with a geometric diode that rectifies in the absence of the bias signal. The rectenna is the IR analogue of a solar cell; note that the largest part of the solar energy is located in IR. The rectenna based on a geometric diode is represented in Fig. 1.61.

### 1.2.3 Graphene Detectors and Receivers

The simplest graphene detector is a coplanar line (CPW) patterned over a graphene monolayer flake (Dragoman et al. 2012b), as shown in Fig. 1.62. Such a graphene radio wave detector was fabricated on a high-resistivity Si substrate, on which 300 nm of SiO<sub>2</sub> is grown by the thermal oxidation method. Then, three parallel gold metallic electrodes forming a CPW were patterned over the graphene monolayer.

The detection of the modulated high-frequency signals is based on the nonlinear DC current-voltage characteristic of graphene with gold contacts, illustrated in Fig. 1.63 with solid line. Further, the experimental  $I$ - $V$  curve is fitted with the equation

$$I = I_0[\exp(V/V_0) - 1], \quad (1.79)$$

the fitting results being marked with dashed lines in Fig. 1.63. The fitting parameters  $I_0$  and  $V_0$  have the values 3.65 mA and 4.68 V, respectively, for the positive polarization, and -2.6 mA and -3.12 V for the negative polarization.

The demodulating term is then found as the second-order term in the Taylor series expansion of the current around the operating point, for which  $I = I_{av}$ ,  $V = V_{av}$ :

$$\Delta I = I - I_{av} = I_0 \frac{V_{RF}^2}{4V_0^2} \exp(V_{av}/V_0) \quad (1.80)$$

In (1.80)  $V_{RF}$  is the RF signal value.

A direct radio can be obtained by connecting this graphene coplanar detector to a modulated high-frequency generator and an oscilloscope, as indicated in Fig. 1.64. The radio can detect carrier wave frequencies between 100 MHz and 25 GHz at a constant power of 0 dBm (1 mW), equivalent to the emitted power of a Bluetooth standard (Class 3) radio in the range 1–5 m. In contrast to radios based on semiconductors, the direct graphene radio is able to work with a good responsivity in a huge frequency range, from the RF spectrum (starting with VHF) up to microwaves

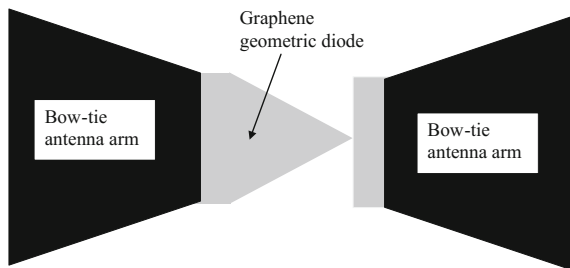


**Fig. 1.61** Graphene rectenna

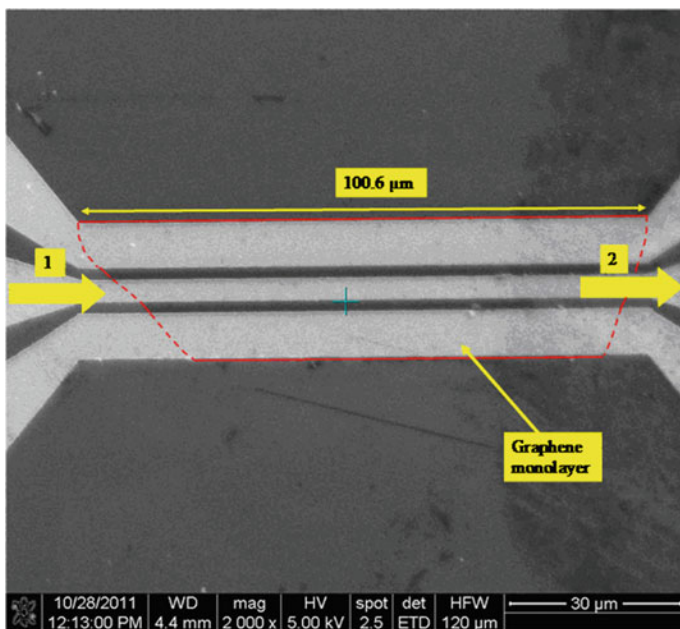


**Fig. 1.62** The coplanar line graphene detector (from Dragoman et al. 2012a, b)

(L-K bands). The AM modulation is 1 kHz, which is compatible with human voice intelligible signals, and is the central frequency of audio hearing aid devices.

The dependence of the amplitude of the demodulated RF signal on frequency is illustrated in Fig. 1.65 for various DC current  $I_{av}$  values: 1 mA (gray thin line), 2 mA (black line) and 3 mA (gray thick line). If the responsivity is defined as the ratio between the detected signal and the RF incident power, the maximum responsivity of the graphene radio, of 1100 V/W, is obtained at 3.5 GHz. Moreover, the CPW graphene demodulator can detect voltages in the range (0.005 V, 0.2 V) in the 3–10 GHz spectrum in the absence of an applied DC current, suggesting that the

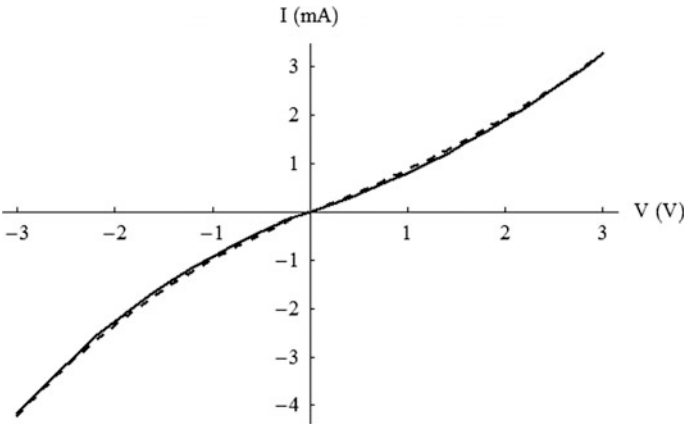


**Fig. 1.63** Current-voltage dependence of the coplanar line patterned over graphene monolayer (from Dragoman et al. 2012a, b)

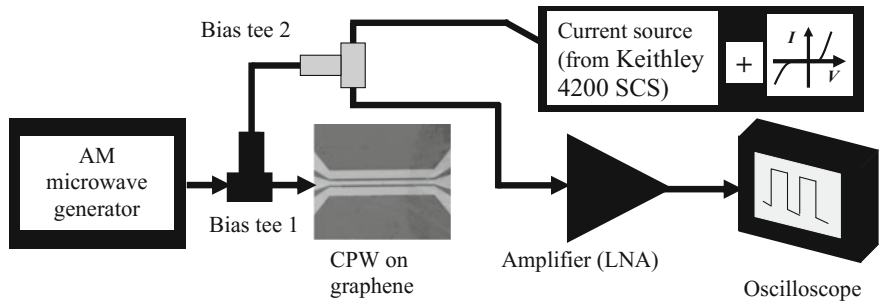
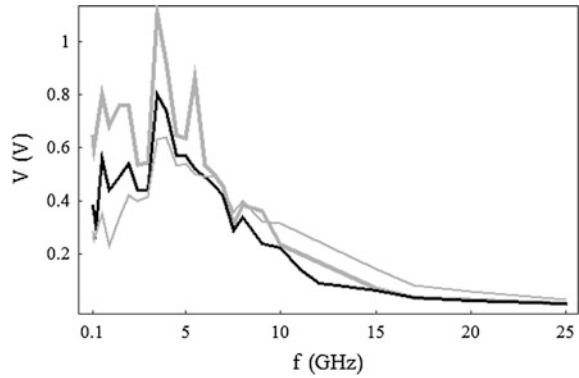


**Fig. 1.64** A graphene monolayer direct radio (from Dragoman et al. 2012a, b)

**Fig. 1.65** Amplitudes of detected signal using the graphene radio (from Dragoman et al. 2012a, b)



graphene coplanar line could work as rectenna in a frequency range where the majority of wireless communications, radar and power transmitters emit.

The results above show that a single sheet of matter—the graphene monolayer—is able to detect high-frequency signals with a very good sensitivity. The first graphene integrated circuit receiver with a carrier frequency of 4.3 GHz was later developed and is represented in Fig. 1.66 (Han et al. 2014). It has an area of 0.6 mm<sup>2</sup> and consists of a two-stage amplifier and a mixer stage. All three transistors T1, T2 and T3 are graphene transistors, with gate lengths of 900 nm and device widths of about 12 μm. The conversion gain of the circuit with 4.3 GHz RF input signal is 10 dB with a low LO input power of 2 dBm, and the gain of the amplifier is around 3 dB. Except the technological performance of integrating few graphene transistors, this receiver shows nothing special regarding its performances, which are well below the existing integrated receivers working in the same frequency band with the same bandwidth. This is a consequence of the fact that graphene transistors in the integrated circuit have poor RF performances.

The results were extended rapidly towards THz frequency range detectors using antennas integrated with graphene transistors. More exactly, THz fields are detected by shaping the gate and source electrodes of graphene FETs into various metallic antennas. The first experimental demonstration of this concept is the detection of a 0.3 THz signal at room temperature using a log-periodic circular-toothed antenna with an outer radius of 322 μm and a grounded source electrode. The channel of the transistor was rather long, of 10 μm. The detected signal at the thin drain contact can be written as (Vicarelli et al. 2012):

$$\Delta V = \frac{V_a^2}{4\sigma(V_0)} \left. \frac{d\sigma(V_G)}{dV_G} \right|_{V_G=V_0} \quad (1.81a)$$

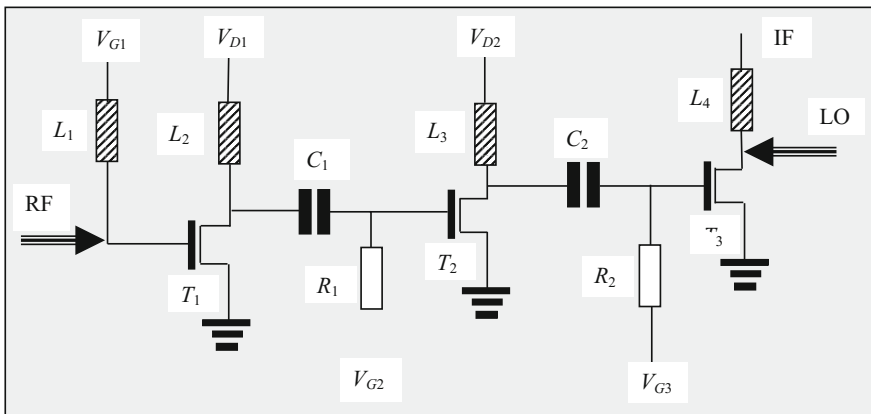


**Fig. 1.66** The 4.3 GHz integrated graphene circuits

where the gate voltage is expressed as

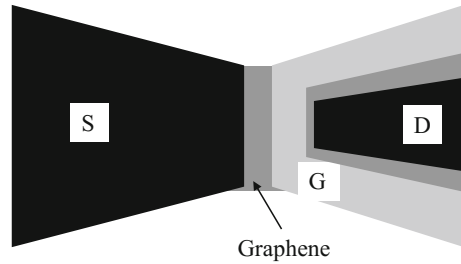
$$V_G(x, t) = V_0 + V_a \exp(-kx) \cos(\omega t - kx) + \frac{V_a^2}{4\sigma(V_0)} \frac{d\sigma(V_G)}{dV_G} \bigg|_{V_G=V_0} [1 - \exp(-2kx)] \quad (1.81b)$$

Another type of antenna—the split bow-tie antenna—was implemented in the same way, consisting of a FET with a graphene channel, with the electrodes in the shape of a bow and capacitive coupling between gate and drain. Figure 1.67 displays the split bow-tie THz graphene detector. In this case, the channel length was shorter, having 2.5  $\mu\text{m}$ , and the gate width was 2  $\mu\text{m}$ . The THz signals were detected at a higher frequency, of 0.6 THz, with a noise-equivalent power (NEP) of 515  $\text{pW}/\text{Hz}^{1/2}$  and a responsivity of 14  $\text{V}/\text{W}$  (Zak et al. 2014).

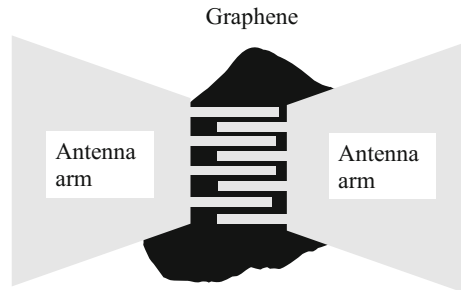
Similarly, a logarithmic-periodic antenna with an interdigitated electrode, consisting of 4 electrode pairs deposited over a graphene flake located in the gap is able to detect THz radiation pulses despite the striking simplicity of this device. This room-temperature THz detector shows a rise time of only 50 ps (Mittendorff et al. 2013). An analogous antenna to that in (Mittendorff et al. 2013) but with bow-tie-shaped instead of logarithmic-periodic arms is represented in Fig. 1.68.

Also, very sensitive THz detection was demonstrated recently at room temperature using the photothermoelectric effect in graphene (Cai et al. 2014). This effect

**Fig. 1.67** Bow-tie antenna electrodes of a graphene FET for THz radiation



**Fig. 1.68** Graphene-based THz pulse detector



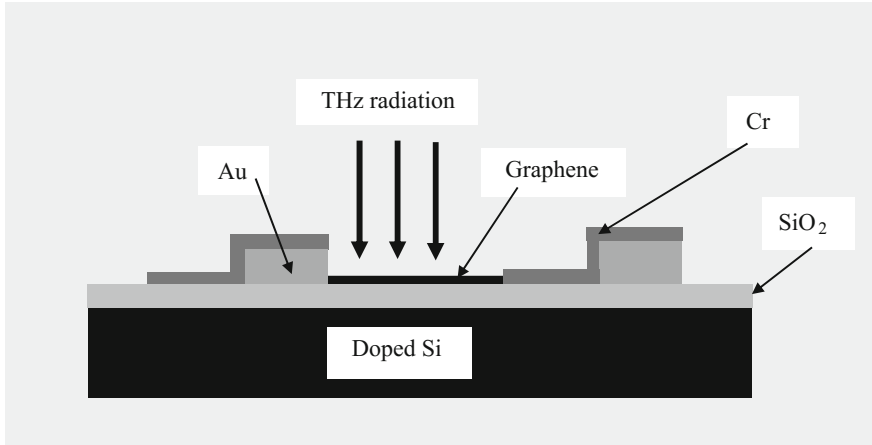


**Fig. 1.69** Photothermoelectric THz detection

is based on a significant interband absorption of graphene in the THz region, as well as on a carrier heat capacity much smaller than in bulk materials, implying an increased temperature gradient for the same absorbed energy. Two dissimilar metals with a  $L = 3 \mu\text{m}$  gap between them were used in experiments to contact graphene, as shown in Fig. 1.69. These metals are in fact overlapping regions of Cr and Au, fabricated via consecutive and different angle evaporations of these metals. The operation principle is based on the fact that the carriers are heated by the incoming THz radiation, while the metallic contacts act as heat sinks, the result being a temperature distribution  $T(x)$  along the device. Then, due to the dissimilar contacts and thus dissimilar contact-induced doping, the Seebeck coefficient  $S$  of graphene becomes spatially asymmetric, and a potential gradient

$$\nabla V(x) = -S \nabla T(x) \quad (1.82)$$

develops due to charge diffusion. The response/output signal of the THz detector is

$$v = \int_0^L \nabla V(x) dx \quad (1.83)$$

At room temperature, the photothermoelectric graphene THz detector has a responsivity of 10 V/W (700 V/W) and a NEP of  $1100 \text{ pW Hz}^{-1/2}$  ( $20 \text{ pW Hz}^{-1/2}$ ) when calculated with respect to the incident (absorbed) power.



## 1.3 Electronic Sensors on 2D Carbon-Based Materials

Graphene is used in many electronic sensors due its exceptional physical and chemical properties, which are listed below (Liu et al. 2015a):

- high and tunable electrical conductivity
- high electron transfer rate due to edges and defects
- mechanical flexibility and strength (two orders of magnitude stronger than steel)
- high surface area (2630 m<sup>2</sup>/g)
- chemical stability
- absence of metallic impurities like in carbon nanotubes and other nanomaterials
- large electrochemical potential window (2.5 V in 0.1 mM phosphate buffer saline solution)
- high thermal conductivity
- fast and strong response in sensing applications

All these properties make graphene a good candidate for many sensing applications. However, the graphene surface needs to be functionalized in order to respond to the many requirements of sensing applications.

By smart processing of its surface, such as oxidation and heteroatomic doping, graphene is enriched with functional materials on its surface and edges. Covalent, noncovalent and other functionalization methods are used in this respect. In principle, each sensor requires a certain functionalization, but some functionalization methods are more frequently used than others and are very successful, and therefore will be presented briefly before describing the main electronic sensors on graphene. The optical sensors based on graphene will be presented in the next section.

Covalent functionalization destroys the conjugated  $sp^2$  structure of graphene and could even immobilize the delocalized  $\pi$  electrons, thus suppressing the graphene conductivity. For example, highly reactive free radicals to be used for addition reactions, which fix aryl-addends on graphene surface, are produced by diazonium salts. These reactions transform the  $sp^2$  structure of graphene in  $sp^3$  and the functionalized graphene becomes an insulating/nonconducting material (Bekyarova et al. 2009). A typical covalent functionalization involves the attachment of carboxyl groups on graphene surfaces, which react in turn with amino groups of a target molecule (DNA, enzyme or proteins). This is the functionalization used for the majority of biosensors that detect electronically DNA or proteins via graphene FETs, for example. Also, graphene oxide is functionalized with thionyl chloride for reaction with hydroxyl or amino groups, whereas nitrogen and boron are used for graphene doping.

Noncovalent functionalization, on the other hand, preserves the original  $sp^2$  structure of graphene, and hence its electrical properties. The main procedure is based on hydrophilic and hydrophobic interactions, and  $\pi$ - $\pi$  stacking. The review (Georgakilas et al. 2012) contains more details on the chemical reactions involved in graphene functionalization and many useful references.

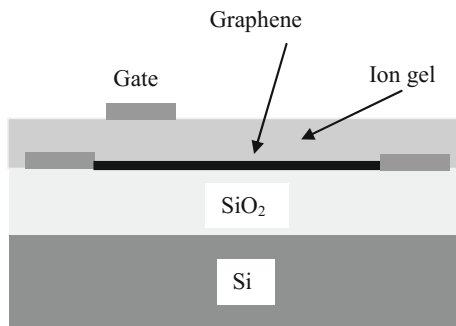
Graphene doping is interesting for a series of applications. For example, a large Fermi level shift, of up to 0.9 eV, corresponding to a high doping concentration, is obtained using ion gels (Chen et al. 2011b) such as 1-ethyl-3-methylimidazolium bis(trifluoromethylsulphonyl)i-mide ([EMIM][TFSI]) as gate dielectrics (see Fig. 1.70).

One of the main reasons of graphene doping, except carrier modulation in transistors and diodes and other tunable devices, is to reduce the surface resistance of graphene. For instance, doped graphene could replace ITO (indium tin oxide) as transparent electrode for solar cells, which would be beneficial because indium is a scarce raw material used in tactile displays, i-phones, laptops and many solar cells. An example of chemical doping of graphene is the use of bis bis (trifluoromethanesulphonyl)-amide  $[(CF_3SO_2)_2NH]$  (TFSA) to increase the power conversion efficiency of a monolayer graphene/Si solar cell from 1.9 to 8.6% (Miao et al. 2012) due to surface resistance reduction as well as Schottky barrier/built-in field enhancement. The doping of graphene is performed by spin-casting TFSA (20 mM in nitromethane) for 1 min at 1000–1500 rpm. The Fermi energy level is shifted by 0.7 eV due to TFSA doping, the series resistance decreases with 30% and the built-in bias increases from 0.36 to 0.56 V. The sheet resistance of five-layer graphene doped with TFSA on a flexible (polyethylene terephthalate) PET substrate is reduced even more significantly, from 240 to  $90 \Omega \text{ sq}^{-1}$  (Kim et al. 2013a).

Because graphene is highly transparent, tactile displays and even stretchable i-phones are among its first applications. The tactile display is in fact an actuator composed from graphene electrodes and a dielectric elastomer substrate. When DC voltages are applied on graphene electrodes, the elastomer is bumping up producing actuation, and it preserves its physical properties up to 25% stretching (see Fig. 1.71).

A cost-effective solution for transparent electrodes used for touch screens is to use silver nanowires coated with graphene, which reduces the amount of required nanowires by 50 times compared to a high-density nanowire network. Thus, the electrical performance of silver nanowires, with ultra-low densities, is enhanced by graphene coating. The Langmuir-Schaefer technique is used to wrap graphene around silver nanowires. As a result, the sheet resistance, of around  $600 \text{ k}\Omega/\text{sq}$  of a low-density Ag nanowire network having a transmittance of 97%, is drastically

**Fig. 1.70** Graphene doping with ion gel



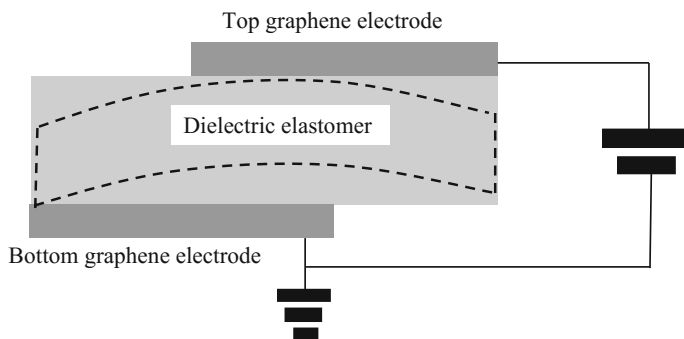


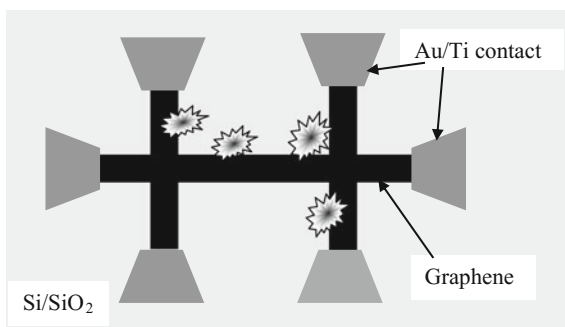
**Fig. 1.71** Graphene actuator for tactile display

reduced by graphene coating, reaching up to  $200 \text{ } \Omega/\text{sq}$ , without affecting too much the transmittance, which remains at a high level, of 93%. Similarly, high-density silver nanowires having initially a  $40 \text{ } \Omega/\text{sq}$  sheet resistance and a transmittance of 93%, attain a sheet resistance of  $28.7 \text{ } \Omega/\text{sq}$  and a transmittance of 87% when covered with graphene. These results are explained by the fact that the electrical conduction of the hybrid structure is increased due to percolation doping. Finally, the touch screen is deposited by laser ablation (Jurewicz et al. 2014).

Since the specific surface area of graphene is  $2630 \text{ m}^2/\text{g}$ —the highest of all materials, graphene is a good material for sensing applications, especially as gas sensors or biosensors (Hill et al. 2011; Yavari and Koratkar 2012; Dragoman and Dragoman 2012). In particular, graphene gas sensors are sensitive enough to detect even a single molecule of gas (Schedin et al. 2007). Gas detection is based on specific changes in graphene resistivity for different gases, which after adsorption on graphene in an interval of typically about 200 s induce a variation of resistivity with +4% for  $\text{NH}_3$ , −4% for  $\text{NO}_2$ , or −1% for  $\text{H}_2\text{O}$  at a gas concentration of 1 ppm. A common graphene gas sensor configuration has the shape of a Hall bar, as illustrated in Fig. 1.72.

In this device, Hall measurements have demonstrated that some gases are graphene donors ( $\text{NH}_3$ , CO, and ethanol), i.e. in these cases  $\Delta\rho/\rho > 0$ , while others,

**Fig. 1.72** Graphene Hall constriction (fabricated by oxygen plasma etching) acting as a gas sensor



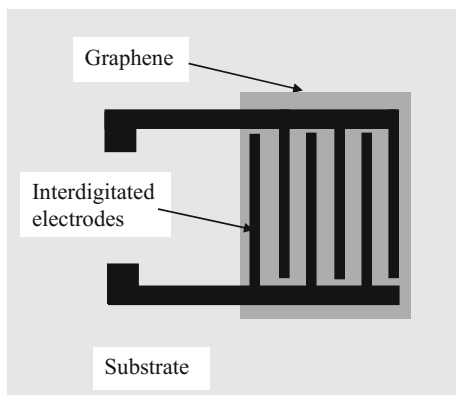
for which  $\Delta\rho/\rho < 0$ , are acceptors ( $\text{NO}_2$ ,  $\text{H}_2\text{O}$  vapors and iodine). The detection limit of the graphene gas sensor is 1 ppb, corresponding to a variation of graphene resistivity of  $\Delta\rho/\rho \propto 10^{-4}$ . Few graphene layers were used to decrease the contact resistance around 100  $\Omega$ . Thus, the variation in adsorption and desorption of a single  $\text{NO}_2$  molecule shows a change in the resistance of 2.5  $\Omega$ . In reality, for normal electronic noses, sensitivities of few parts per billion are easily obtained with a simple sensor geometry made from a graphene monolayer with two metallic contacts or interdigitated electrodes, as shown in Fig. 1.73.

More recently, researches have found a surprising result, that graphene defects, such as an isolated grain boundary, have 300 times higher sensitivity for detecting adsorbed gas molecules than a single-crystalline graphene grain. Graphene and the grain boundary are grown via CVD at normal atmospheric pressure, and controlled growth time. Under such conditions, single-crystalline graphene grains with a generally hexagonal shape grow individually and eventually merge into an individual grain boundary. Much higher gas detection sensitivity is achieved due to accumulation of adsorbed gas molecules at the boundary between graphene grains, favored by the appearance of a stress-relaxation-induced corrugation in this region, which is equivalent to local doping/electric field gradient (Yasaei et al. 2014).

Several grain boundaries connected in series can be obtained and further connected to obtain a very sensitive gas sensor, i.e. an electronic nose. Such a gas sensor containing two grain boundaries is illustrated in Fig. 1.74. The sensitivity of the sensor is defined as  $S = (R - R_0)/R_0$ , with  $R$  and  $R_0$  the resistance of the device after and before gas exposure, respectively. Taking into account in a more detailed manner the different contributions to the total resistance, the sensitivity of the electronic nose can be written as

$$S = \frac{N\Delta R_{GB} + 2N\Delta R_{G1} + (N-1)\Delta R_{G2}}{NR_{GB} + 2NR_{G1} + (N-1)R_{G2}} \quad (1.84)$$

**Fig. 1.73** An interdigitated electrode for graphene gas sensing



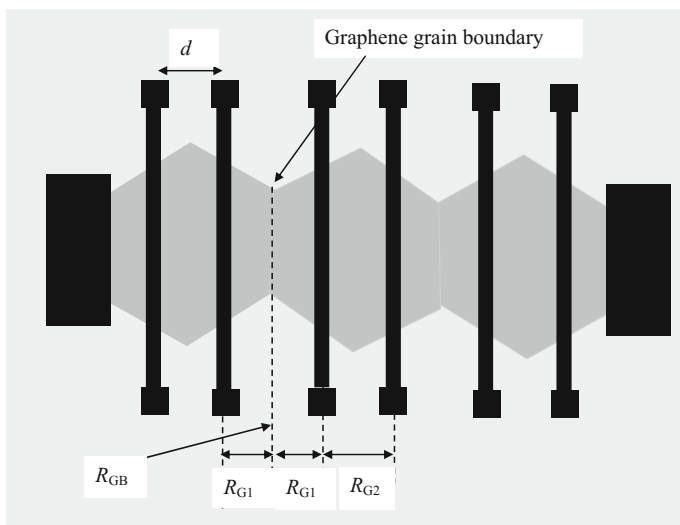
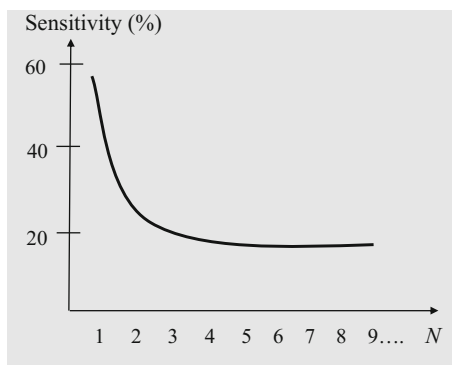


**Fig. 1.74** Gas sensor containing two graphene grain boundaries

where  $N$  is the number of grain boundaries,  $R_{GB}$  is the resistance of an isolated grain boundary, and  $R_{G1}$  and  $R_{G2}$  are the resistances of the trapezoidal graphene region and of the single-crystalline region, respectively. From (1.84) it follows that when  $N = 1$  the terms containing  $R_{G2}$  vanish and the sensitivity increases significantly. The dependence of sensitivity on the number of grain boundaries is displayed in Fig. 1.75. Also, Fig. 1.76 indicates that the distance between electrodes,  $d$ , is critical for obtaining a high sensitivity.

As an example of an ultrasensitive electronic nose, a bilayer graphene transistor was fabricated on a flexible PET substrate (Park et al. 2012). The transistor has a ionic liquid gate consisting of a phosphate-buffered solution (PBS) with a pH of 7.4, the sensing layer being obtained by integrating the modified (by oxygen and

**Fig. 1.75** Sensitivity dependence on  $N$  of a graphene grain boundary gas sensor (after Yasaei et al. 2014)



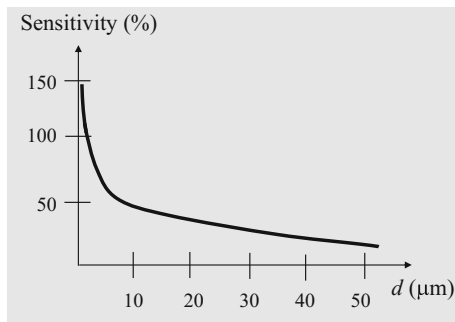


**Fig. 1.76** Dependence of graphene grain boundary gas sensor sensitivity on the distance between electrodes (after Yasaei et al. 2014)

ammonia treatments) bilayer graphene with the human olfactory receptor 2AG1 (hOR2AG1:OR). OR binds selectively to the amyl butyrate (AB) odorant. This flexible nose is so sensitive that it is able to detect an odorant with atom resolution, with a minimum detection limit of 0.04 fM. The sensing is based on the change of the transistor drain conductance with the AB binding quantity.

Very sensitive and very rapid vapor sensors are obtained using heterodyne graphene sensors (Kulkarni et al. 2014). In this case, an AC signal  $V_\omega$ , with frequency  $\omega$ , is injected in the source of a graphene FET with DC grounded source and gate, as shown in Fig. 1.77. The electrostatic coupling between the gate

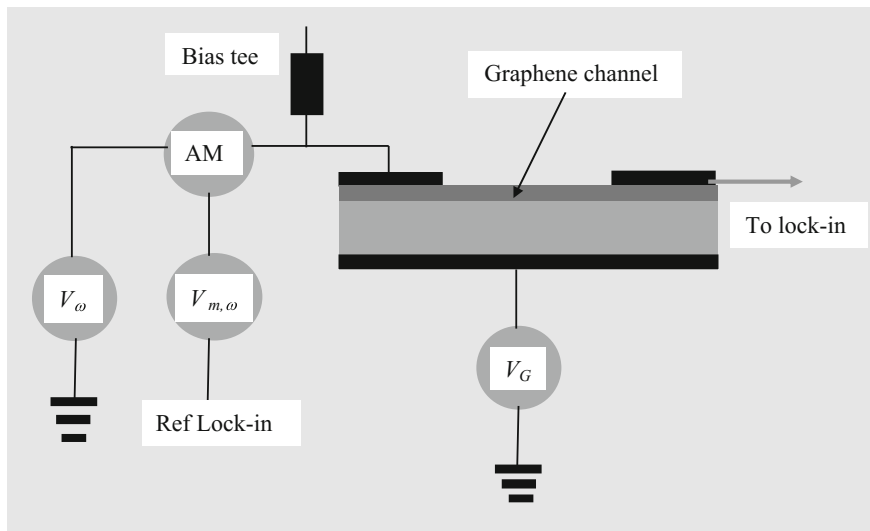


**Fig. 1.77** Heterodyne graphene FET gas sensor

electrode and the graphene channel generates a gate-induced modulation of the charge density given by

$$Q_{G,\omega} = C_G V_{G,\omega} = -C_G V_\omega / 2 \quad (1.85)$$

where  $C_G$  is the gate capacitance. When a molecule is adsorbed, dipole-induced charge densities  $Q_{m,\omega}$  appear, modulated at the frequency  $\omega$ . The frequency mixing between  $V_\omega$  and the total modulated charge is expressed by the mixing current

$$I_{mix} = G_\omega V_\omega = (\mu W / L) (-C_G V_\omega / 2 + Q_{m,\omega}) V_\omega \quad (1.86)$$

For vapor sensing, the relevant quantity is the change in the mixing current, given by

$$\Delta I_{mix} = (\mu W / L) Q_{m,\omega} V_\omega \quad (1.87)$$

To improve the noise performance, an AM modulation can be introduced. The AC signal frequency is 100 kHz and the AM modulation frequency is of 1.43 kHz in the device studied in (Kulkarni et al. 2014). This sensor was tested for dichloromethane, showing a response time of 0.61 s, for ethanol, with a response time of 0.92 s, and for other vapors with similar response times. The sensor is able to detect airborne chemicals, either exhaled or released through skin, and various dangerous gases.

There are also mechanical sensors based on graphene, which detect parameters such as pressure and strain. Pressure sensors used as touch control displays were presented earlier. However, for a gentle touch and small objects' manipulation, pressure in the range of 10–100 kPa need to be detected. Laser-scribed graphene (LSG), which are loosely stacked graphene layers with a foam-like structure, can be used as sensing material for these purposes (Tian et al. 2015). The sensor is displayed in Fig. 1.78. The sensitivity of the LSG graphene sensor is defined in terms of the relative variation of the conductance as

$$S = \delta(\Delta G / G_0) / \delta P \quad (1.88)$$

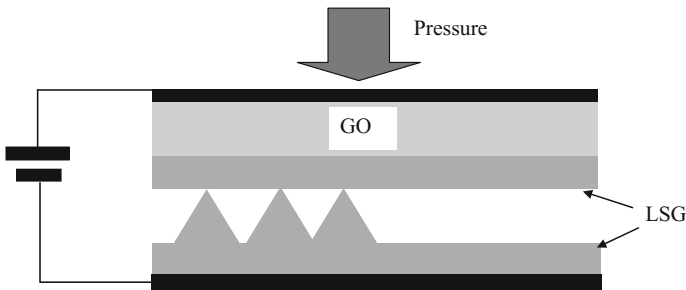


**Fig. 1.78** LSG graphene pressure sensor

its value being  $0.96 \text{ kPa}^{-1}$  for pressures  $P$  lower than 50 kPa, while the response and releasing times at 26 kPa are of 72 and 0.4 ms, respectively.

Using the same LSG technology, graphene earphones on PET were fabricated for communications for both human and animals (Tian et al. 2014). Humans can hear sounds in the bandwidth 20 Hz–20 kHz, whereas animals communicate in the ultrasound spectrum: bats up to 160 kHz, whales at 160 kHz, while dolphins generate sounds at 300 kHz. The graphene earphones have a frequency response in the range 100 Hz–50 kHz and low fluctuations ( $\pm 10 \text{ dB}$ ), whereas graphene sound emitters could reach 1 MHz.

Arrays of pressure/temperature sensors, called electronic skin in analogy with human skin, have a wide range of applications in bionics, robotics and high-tech industries. An e-skin made from reduced graphene oxide foam (RGOF) obtained from a frozen GO solution reduced with hydriodic acid (HI) followed by washing and drying was recently reported (Hou et al. 2014). RGOFs are porous due to the ice template, and the networks preserve their patterns after ice melting and removal. RGOFs are freely standing, flexible, and have a sheet resistance of  $1.5 \text{ }\Omega/\text{sq}$ , this remarkable value being due to the fact that HI reduction induces iodine doping. RGOFs can be compressed up to 65% by a strain of 2 kPa and recover rapidly their initial shape and physical properties; for example, the electrical properties are recovered after 0.05 s. As such, the RGOF can be tuned by human touch (1–10 kPa). Moreover, RGOFs response discriminates between human touch and otherwise applied pressure via surface temperature difference between humans and inanimate objects, which indicates a temperature-activated sensing mechanism.

As electronic skin, the RGOF is contacted on the upper and lower surfaces and placed on PET, at a temperature of  $20 \text{ }^\circ\text{C}$ , as schematically represented in Fig. 1.79. The upper levels of this artificial skin are heated at different temperatures. Rather high temperature differences can be applied between the heated surface, along  $x$ , and other areas of the devices (along the  $y$  and  $z$  directions), inducing corresponding current flows due to the high thermoelectric effect in graphene and its network formed in RGOF. For example, if a temperature difference of about  $30 \text{ }^\circ\text{C}$  is applied between electrodes along the  $z$  direction, a current of  $9 \text{ }\mu\text{A}$  is measured between the corresponding electrodes (a comparable current is measured between electrodes along the  $y$  direction), if the heating surface of RGOF sample is  $5.6 \text{ cm}^2$ . Based on this principle, RGOF is able to discriminate between human body and other objects, such as metals, plastic or glass, when the applied pressure alone is not high enough to induce significant changes in the resistance. The sensor responds in this case only to human body touch, because the body temperature is higher than the surroundings (Hou et al. 2014). The sensitivity of this device to pressure, defined as  $\delta(\Delta I/I_0)/\delta\Delta p$ , is  $15.2 \text{ kPa}^{-1}$  for  $\Delta p = 300 \text{ Pa}$ .

Placing arrays of FETs on flexible substrate is another approach to implement an e-skin (Sun et al. 2014). Such a device involves only graphene and a ion gel dielectric, and consists of a top cover layer and a backplane, separated by  $100 \text{ }\mu\text{m}$  thick epoxy; this configuration forms a pixel of the pressure sensor matrix, which contains  $4 \times 4$  pixels. The top cover contains a square graphene region, the contour of which is represented by a dashed line in Fig. 1.80, placed on a flexible PET



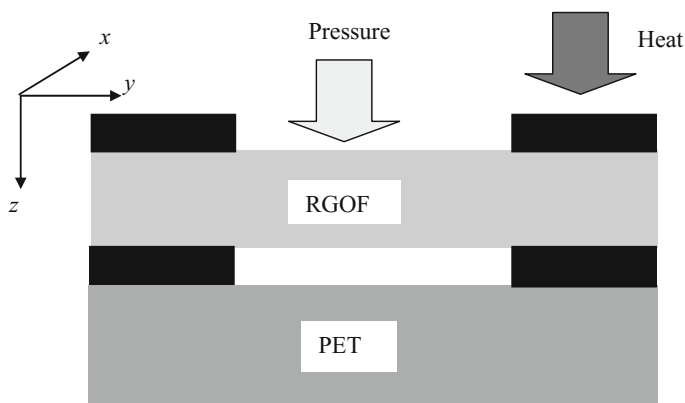
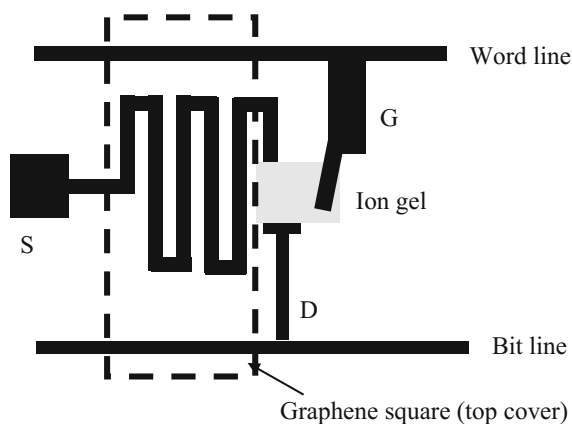


**Fig. 1.79** Electronic skin based on RGOF

substrate. The backplane contains a graphene FET, which acts as pressure sensor. The graphene FET is patterned in a coplanar-gate configuration, and consists of a single graphene strip on which an ion gel is deposited. The graphene region below the ion gel is the FET channel, the remaining graphene strip regions acting as drain and zigzag-shaped source electrodes. The drain is connected to the bit line and the gate electrode, which is also a graphene strip, is connected to the word line of the device (see Fig. 1.80). The gate dielectric is in this case an ion gel formed from poly (ethylene glycol) diacrylate (PEGDA) monomers, the photo-initiator 2-hydroxy-2-methylpropiophenone (HOMPP) and the ionic liquid 1-ethyl-3-methylimidazolium bis(trifluoromethyl sulfonyl)imide ([EMIM][TFSI]) with a weight ratio 7:3:90. When pressure is applied, the square graphene on the top cover is in contact with the bottom zigzag source electrode, the resistance between source and drain is reduced, and thus the conductance increases. The transistors work at 2 V and have a pressure

**Fig. 1.80** One pixel of a graphene-based e-skin



sensitivity of  $0.12 \text{ kPa}^{-1}$ . The drain conductance is about  $5 \text{ }\mu\text{S}$  at  $10 \text{ kPa}$ ,  $8 \text{ }\mu\text{S}$  at  $20 \text{ kPa}$ , and  $14 \text{ }\mu\text{S}$  at  $30 \text{ kPa}$ .

Because there is a close relation between pressure and strain, graphene is a good candidate for strain sensors also (Zhao et al. 2013). The relation between the variation of the electrical resistance of graphene and the applied mechanical strain  $\varepsilon$  can be written as

$$\Delta R/R = (1 + 2\nu)\varepsilon + \Delta\rho/\rho = (1 + 2\nu)\varepsilon - 2\Delta v_F/v_F \quad (1.89)$$

where  $\nu = 0.2$  is the Poisson ratio,  $\rho$  is the resistivity and  $\Delta\rho$  and  $\Delta v_F$  are the changes in resistivity and Fermi velocity, respectively, caused by strain. Strain sensors are widespread in buildings, bridges, airplanes, cars and anywhere where mechanical deformations are monitored. According to (Zhao et al. 2013) the strain market is exceeding 5 billions dollars. A typical strain sensor configuration based on suspended graphene is represented in Fig. 1.81.

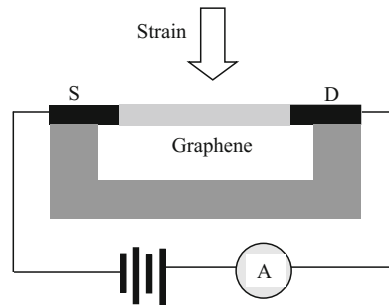
The gauge factor describing the sensitivity of strain sensors is defined as the ratio between the electrical resistance variation and the mechanical strain:

$$G = (\Delta R/R)/\varepsilon \quad (1.90)$$

We have pointed out already that graphene has exceptional mechanical properties, the third-order elastic stiffness of this material being  $-2 \text{ TPa}$ , with an intrinsic strength of  $130 \text{ GPa}$  at  $25\%$  in-plane tensile strain (Lee et al. 2008). A suspended graphene membrane used as a strain sensor shows a  $5\%$  change in the resistance ( $\Delta R/R$ ) for  $3\%$  strain, corresponding to a gauge factor of  $1.9$  (Huang et al. 2011b). For CVD grown graphene transferred on PDMS substrates, it was shown that the electrical conductance behaves reversibly as the elastic tensile strain varies up to  $4.5\%$  (Fu et al. 2011) with a high gauge factor of  $150$ .

The piezoresistivity of graphene is used in many strain sensor types. For example, large graphene areas in which graphene growth is not completed, i.e. consisting of graphene sheets connected together in a network, are sensitive strain detectors. When compressive or tensile strain is applied to the graphene area, the overlapping areas between graphene sheets change, inducing a change in resistance.

**Fig. 1.81** Graphene strain sensor



Tunneling between adjacent graphene sheets is another mechanism for obtaining an exponential dependence of the electrical resistance as a function of applied strain.

A piezoresistive sensor containing a SiN<sub>x</sub> membrane on which a graphene meander resistance is patterned is depicted in Fig. 1.82 (Zhu et al. 2013a). The pressure sensing mechanism is based on inducing strain in graphene by applying pressure across the membrane (see Fig. 1.83). The maximum tensile strain, of about 0.25%, appears at the middle of each edge of the membrane. The thickness of the square SiN<sub>x</sub> membrane is of 100 nm, its length is 280 μm with a residue stress of 50 MPa, a Young modulus of 200 GPa and a Possion ratio of 0.22.

Under an applied strain, the resistance  $R$  of the meandering graphene resistor, measured with a Wheatstone bridge, changes with  $\Delta R$ . The parameter that is measured is the voltage drop across the graphene resistor for an input voltage of  $V_{in} = 2.5$  V. The output voltage is given by

$$V_{out} = V_{in}\Delta R/(2R + \Delta R) \quad (1.91)$$

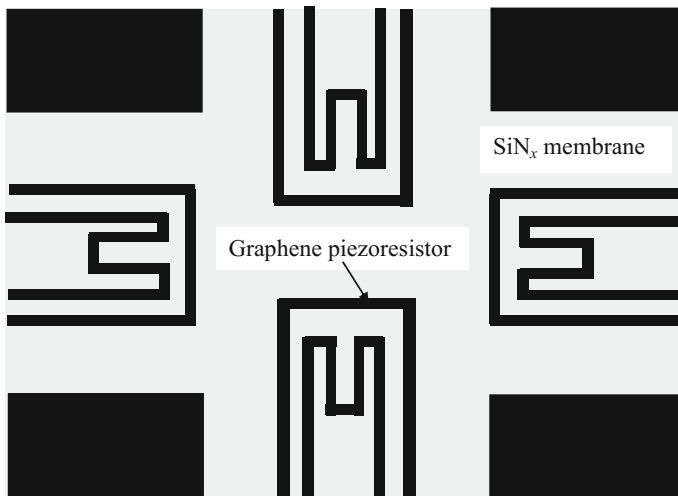


**Fig. 1.82** Pressure sensor containing four graphene piezoresistors

**Fig. 1.83** Principle of the graphene pressure sensor

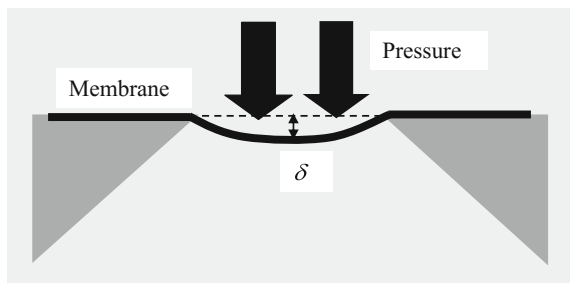
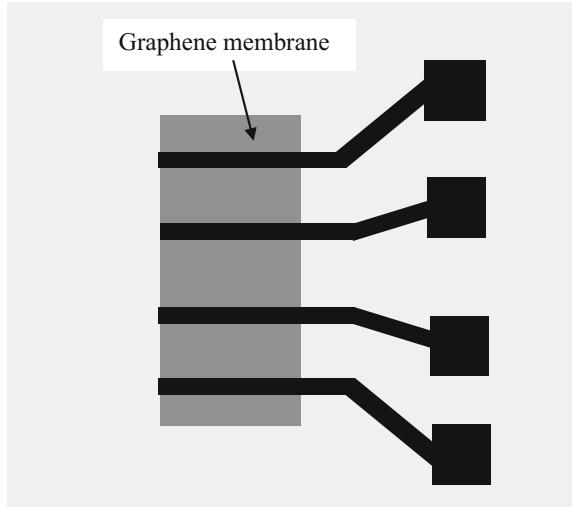


**Fig. 1.84** Pressure sensor on a graphene membrane



The linearity of the above relation is maintained up to 500 mbar (50 kPa) with a sensitivity of 8.5 mV/bar. For example, an output voltage of 5 mV is obtained for a 0.4% resistance change in 0.9 s, the sensor having a gauge factor of 1.6.

The piezoresistive effect was demonstrated also using graphene as a membrane suspended over cavities etched in a Si/SiO<sub>2</sub> substrate (Smith et al. 2013). In this case, the gauge factor was 2.92 and the sensitivity per unit area attained almost 4  $\mu\text{V/V/mmHg}$ , which is 20–100 times better than in conventional pressure sensors. The output voltage of this device, represented in Fig. 1.84, is collected with a Wheatstone bridge.

The resistance of the suspended graphene sheet depends on the mechanical strain as

$$R_{g,suspended} = L(1 + \varepsilon_{xx}) / [W(1 + \varepsilon_{yy}) \times (2eN(\varepsilon)\mu(E))] \quad (1.92)$$

where  $N$  and  $\mu$  are the carrier density and mobility, respectively, and  $\varepsilon_{xx}$  and  $\varepsilon_{yy}$  are the strain tensor's components parallel and perpendicular to the carrier transport direction. The induced strain is uniaxial because  $\varepsilon_{xx} \gg \varepsilon_{yy}$ . The value of the resistance in Smith et al. (2013), of about 0.2 k $\Omega$  at 1000 mbar, changes with 0.6% with respect to the value in the absence of an applied pressure.

The piezoresistive effect in graphene monolayers is exploited in NEMS (nano-electro-mechanical-systems) as an effective readout method, the NEMS resonator consisting of a H-shaped graphene monolayer clamped at the four corners, as shown in Fig. 1.85 (Kumar and Bhaskaran 2015). In NEMS resonators, which act as mass or force sensors, two important parameters must be determined. One of them is the minimum detectable mass:

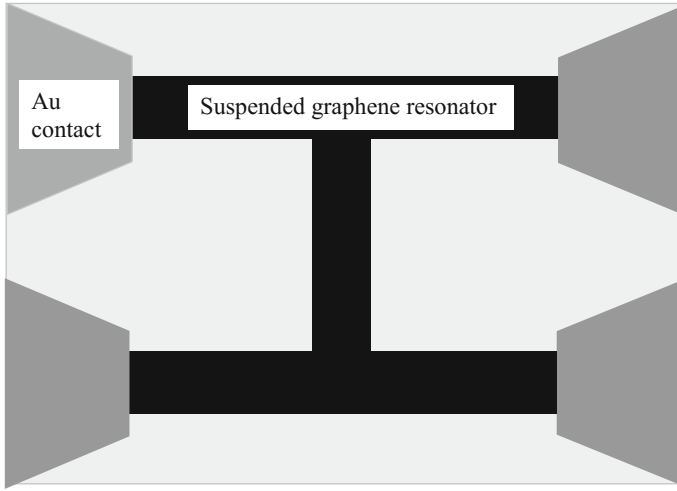


**Fig. 1.85** The graphene monolayer suspended NEMS resonator

$$\delta m = 2m_{\text{eff}} \sqrt{\Delta f / Q \times \omega_r} 10^{-(DR/20)} \quad (1.93)$$

where  $m_{\text{eff}}$  is the mass of the resonator,  $Q$  is the quality factor,  $\omega_r$  the resonance frequency,  $\Delta f$  is the bandwidth, and DR the dynamic range. The other parameter is the minimum detectable force, defined as

$$F_{\min} = \sqrt{4k_B T k / \omega Q} \quad (1.94)$$

where  $k = m_{\text{eff}} \omega^2$  is the spring constant and  $T$  the temperature.

The mechanical resonator with a resonant frequency of about 1.2 MHz has a total length of 1.8  $\mu\text{m}$  and a total width of 1.2  $\mu\text{m}$ , each leg being 120–150 nm wide and 0.5–0.7  $\mu\text{m}$  long. The quality factor at room temperature and 4  $\mu\text{Torr}$  is around 1000. The resonator is mounted on a piezo disk and is mechanically activated by an external DC voltage (see Fig. 1.86), while a bias voltage is applied across the two legs on the same side of the resonator to transduce the change in resistance of the resonator due to mechanical action into voltage. The minimum detectable mass is 1.4 zg ( $10^{-21}$  g), and the minimum detectable force of this mechanical sensor is 16 aN/(Hz) $^{1/2}$  for a spring constant of  $10^{-4}$  N/m.

Wearable electronics is one of the most advanced nanotechnologies focused on new devices that combine mechanical and electronic properties of nanomaterials mounted on skin or near the skin. Nanomaterials for such applications must have special properties. In particular, they should be stretchable, bendable, and deformable at any motion. Such devices, integrated into clothing or directly on skin, have applications in monitoring of finger and muscle motions, sensing the posture,

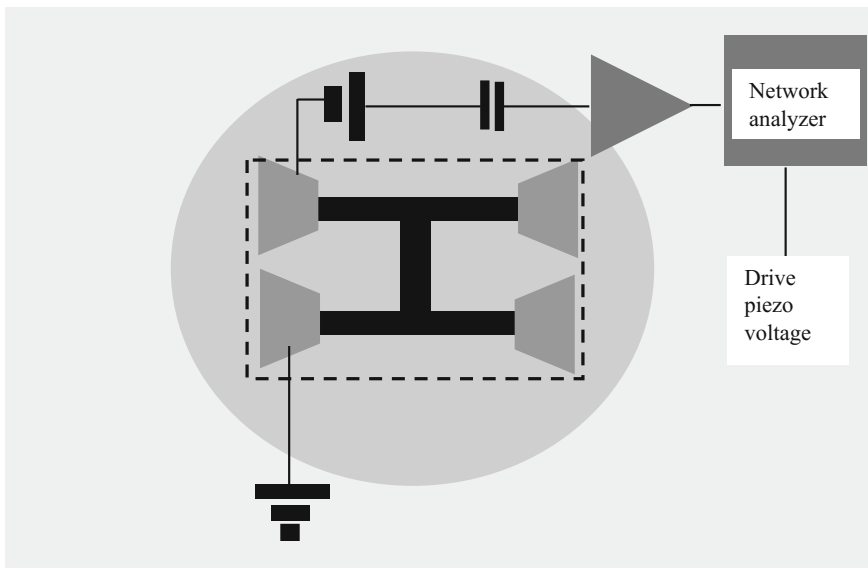


**Fig. 1.86** Measurement set-up of the graphene NEMS resonator

movement and breathing. Medical applications range from emergency medicine up to remote monitoring of patients.

Wearable sensors must satisfy some prerequisites (Boland et al. 2014):

- (i) light weight and high degree of miniaturization
- (ii) high sensitivity
- (iii) ability to work under high strain
- (iv) fast time response

Recently, it was demonstrated that graphene-rubber composites satisfy the conditions above (Boland et al. 2014), graphene being an ideal filler for strain sensors. Graphene infiltrates commercial elastic bands, conferring them electrical properties, sensing being based in most cases on the change of the resistance with strain. The concentration or volume fraction of graphene at depth  $x$  in composites

$$\phi(x) \propto \operatorname{erfc}(x/\sqrt{4Dt_s}) \quad (1.95)$$

is determined by the diffusion coefficient of graphene into rubber,  $D = 4 \times 10^{-13} \text{ m}^2/\text{s}$ , and the soak time  $t_s$ . At low graphene concentration, the resistance of the composite is  $4 \text{ M}\Omega$ , but decreases at  $57 \text{ k}\Omega$  at a graphene concentration of 0.56% with a soak time of 48 h. The conductivity of the composite is described by the percolation theory, where the conductivity is given by

$$\sigma = \sigma_0(\phi - \phi_c)^t \quad (1.96)$$

with  $t$  the percolation exponent,  $\sigma_0$  the conductivity of the filler in a thin film configuration, and  $\phi_c = 0.1\%$  the experimentally determined graphene concentration at which percolation occurs.

The resistance of the graphene rubber composite changes with orders of magnitude at strains up to 600% and beyond (see Fig. 1.87). Note that the rubber is very extensible, showing breaking at a strain of 1100%. The gauge factor is dependent also on the volume fraction, reaching 20 at 0.1%.

The above composite was used to monitor the movement of the first knuckle of index finger. The strain motion reached  $\varepsilon = 40\%$  when the finger was bent few times. Breathing was also monitored by observing periodic, repetitive changes in the resistance of the composite from 1 to 2 M $\Omega$ . Also, the muscle movements were detected by wrapping the composite band around the forearm.

There are also transparent and flexible strain sensors (Bae et al. 2013), used for monitoring the motion of body parts. In this case, the strain sensor is fabricated from CVD grown graphene on Ni followed by reactive ion etching and stamping techniques, graphene being finally transferred on flexible or stretchable substrates, such as PDMS. The PDMS transmittance is 70% in the visible region. The flexible strain sensor is based on the piezoresistive effect of graphene, i.e. on the variation of the electrical resistance with strain. In this case, the resistance has a nonlinear variation with the strain, starting from 500 k $\Omega$  for 0–0.5% strain and reaching 900 k $\Omega$  for 7% strain. A rosette-like configuration containing three transparent strain sensors, each of them oriented at 120° with respect to the others, was used to detect the three independent components of the strain tensor (see Fig. 1.88). A rosette-like strain sensor array was introduced in gloves, targeting wearable electronics applications to detect finger motions.

Very effective strain sensors for wearable electronics, displaying high stretchability of up to 150%, are made in a simple way, by using different stretchable yarns on which poly(vinyl alcohol) (PVA) and graphene nanoplatelets (GNP) are deposited using layer by layer techniques (Park et al. 2015). Depending on the yarn structure, these strain sensors are able to detect large-scale body motion, such as

**Fig. 1.87** Graphene composite change in resistance versus strain (after Boland et al. 2014)

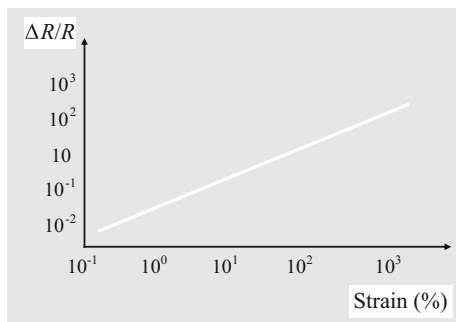
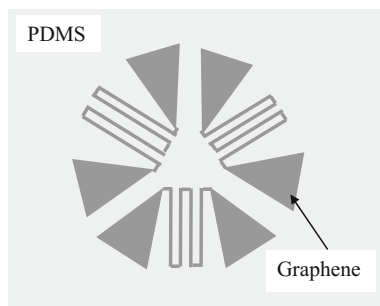


**Fig. 1.88** Rosette-like transparent graphene strain sensor

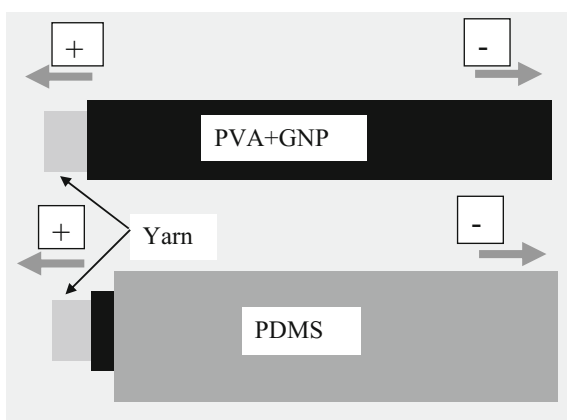


bending movements of the hands, arms and legs, and small-scale body motions, such as chest and neck motions associated with breathing, speaking, and swallowing. The uncoated strain sensor based on depositing several layers of PVA and GNP on the yarn is displayed in the upper part of Fig. 1.89, whereas the sensor with a protective PDMS coating is represented in the lower part of the same figure.

Different stretchable yarns were tested in sensors coated with PDMS: (i) wool yarns (WY), (ii) rubber (RY), and (iii) nylon covered rubber (NCRY), all having good stretchability. As the strain changes between 0 and 100%,  $\Delta R/R$  varies by 2000% in the case of RY and by 200% in the case of NCRY, whereas  $\Delta R/R$  decreases about 10% when the strain on WY is varied between 0 and 50%. The difference in resistance increases in all cases with the number of PVA and GNP layers. In particular, small-scale motion of the throat and large-scale motion of fingers were detected by monitoring  $\Delta R/R$  in time.

For wearable electronics, autonomous and miniaturized DC sources are necessary. Supercapacitors based on graphene, which are shape-tailorable, were recently reported (Xie et al. 2015). Graphene is an ideal candidate for supercapacitors since its specific surface area is 2675 m<sup>2</sup>/g and has a very high specific capacitance (550 F/g). The supercapacitor consists of Ni nanocone arrays covered with reduced graphene oxide (RGO) sandwiched between two flexible electrodes.

**Fig. 1.89** Graphene yarn strain sensor





The last category of graphene sensors discussed in this section is the biosensor. Biosensors are well described in our book about Bionanoelectronics (Dragoman and Dragoman 2012), reprinted in China at 2015. However, few years ago graphene biosensors were in infancy. Therefore, this topic is discussed in more details here.

A biosensor is a device formed from two parts: (i) a bioreceptor, which is the sensing part, connected to (ii) the detector, which transforms the information about the sensed analyte into a signal (optical, electrical, etc.). The configuration of the biosensor is represented in Fig. 1.90.

Depending on the type of bioreceptors, we have immunobiosensors, genobiosensors, enzymatic biosensors, while with respect to the detection process we have electrical, optical, piezoelectric and electrochemical biosensors. The electrochemical biosensors are widespread and further divided into impedimetric, potentiometric or amperometric sensors. All these categories of sensors are able to detect glucose, cholesterol, E-coli, viruses, cortisol, DNA amino acids and vapors and gases relevant for breath diagnosis, for example, or dangerous gases (Kuila et al. 2011). Graphene biosensors are able to detect the main cancer biomarkers, cancer cells and pathological bacteria and pathogens, traces of the Alzheimer disease, and can act as scaffolds for stem cells.

Graphene is considered as an elite nanomaterial for biosensing (Kumar et al. 2015). Among the many unique attributes of graphene, of relevance for this application is that in all carbon-based nanomaterials there is a direct electron transfer between the functionalized nanomaterial and the bioreceptor, without any mediator (fluorescent molecules, chemical groups, etc.). As such, graphene amplifies the output signal and confers high sensitivity to free-label sensing. Graphene is also a biocompatible material.

A large majority of graphene biosensors are based on graphene FETs and FET arrays, where the biomolecules to be sensed change the conductance of the channel, thus modifying the drain current and the transconductance. A typical graphene FET biosensor with liquid gate is depicted in Fig. 1.91.

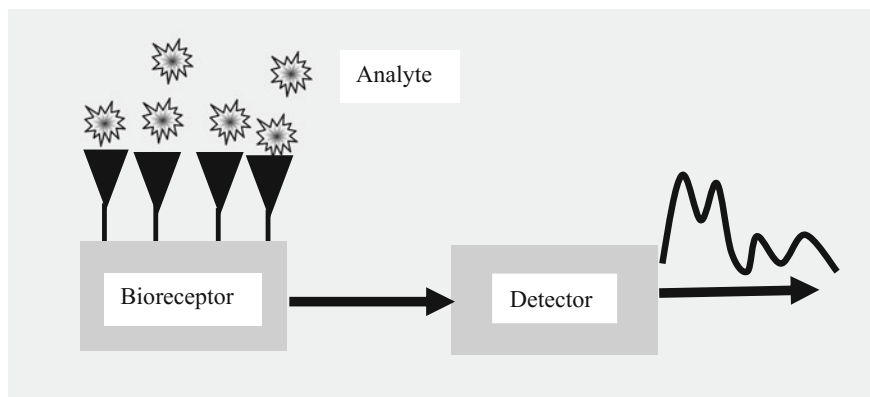


**Fig. 1.90** Biosensor configuration

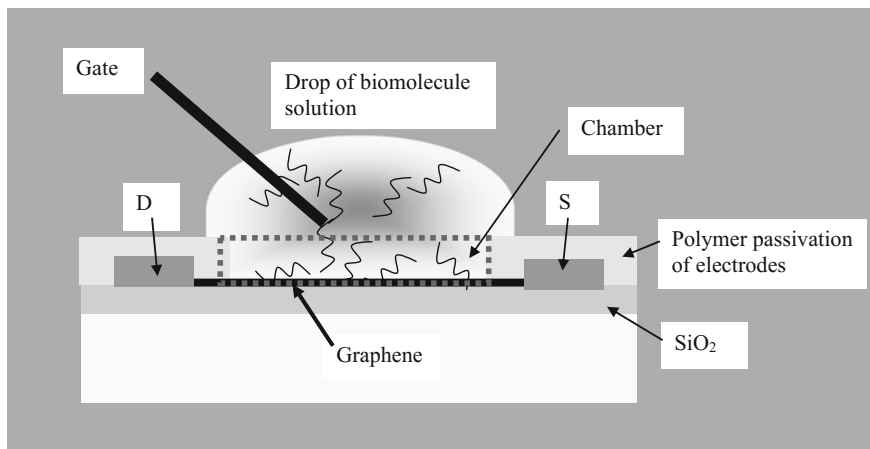


**Fig. 1.91** Typical configuration of graphene biosensor based on graphene FET

Molecules are anchored to graphene, functionalized in a special manner to hold the majority of biomolecules on the graphene channel. Hence, significant changes in the channel conduction are produced by the sensed biomolecules. The main property of the graphene FET biosensor is the liquid gate. In principle, the ionic liquid separates the gate electrode and the graphene sheet that forms the transistor channel. At low gate bias, the current flow is limited by the formation of a Debye layer (a double ionic layer), but at high gate voltages the electrolytic processes produce relatively high currents between the gate and graphene. Graphene FETs based on liquid gates are also used to detect proteins, small molecules and viruses (Green and Norton 2015).

The ultimate performance of such a sensor was the detection of a single base mutation from a DNA sequence (Dong et al. 2010). The probe, the complementary DNA and the one-base mismatched DNA string were dissolved in phosphate buffered saline (PBS, with pH 7.4), which contains 0.25 M NaCl and 10 mM phosphate. The probe DNA is preimmobilized on graphene and 40  $\mu\text{L}$  of PBS is added in the chamber made of PDMS, the gate voltage being applied via an Ag wire. The detection sensitivity is of 0.01 nM. The target DNA introduces an  $n$ -doping of graphene, so that the transconductance changes. This  $n$ -doping is observed by monitoring the  $I_D - V_G$  dependence, which shifts upwards in current in this case, the Dirac point showing a slight shift towards higher gate voltages. The shift in the gate voltage corresponding to the minimum current, which is the footprint of the Dirac point, is directly proportional to the concentration of the complementary sequence. As this concentration increases from 0.01 up to 10 nM, the shift increases from 10 to 55 mV. For higher concentrations of the complementary sequence there is no gate voltage shift due to the saturation of the hybridization process. On the other hand, the shift of the voltage corresponding to minimum current is less pronounced for one-base mismatched DNA string, the shift

being of only 20 mV for a concentration of 500 mM. The biosensing mechanism is displayed in Fig. 1.92.

Another important application of graphene in biosensors is DNA sequencing using nanopores, which implies the electrical detection of the sequence of bases A, G, C and T that form the DNA code. DNA sequencing provides important information for the understanding and early detection of serious diseases such as cancer. The electrical detection of DNA sequences is based on the fact that the DNA backbone is charged in ionic solution. More precisely, a single negative charge corresponds to each nucleotide, or two charges are associated to a pair of nucleotides for ds (double-stranded) DNA. As the negatively charged DNA is dragged by an applied electric field through a nanopore with a very small diameter, of 1–2 nm, the bases generate distinct electrical signals, which are further amplified and processed (Zwolak and di Ventra 2008). The nanopore diameter must be so small because the DNA diameter is no larger than 2 nm, the length of a nucleoside being of 0.7 nm. Thus, the limits of nanotechnologies and electronics are reached, and in many ways a nanopore-based DNA sequencing device, as that represented in Fig. 1.93, is one of the most advanced nanoelectronic circuits.

DNA sequencing using a nanopore consists of two ionic chambers with the roles of trapping and translocating the DNA sequence, respectively, followed by electronic detection. The ionic chambers that trap and translocate the DNA sequence are labelled as *cis* and *trans*. By applying a DC bias across the nanopore, a DC electric field is created, which generates an ionic current through the pore by pulling out the negatively charged DNA through the pore.

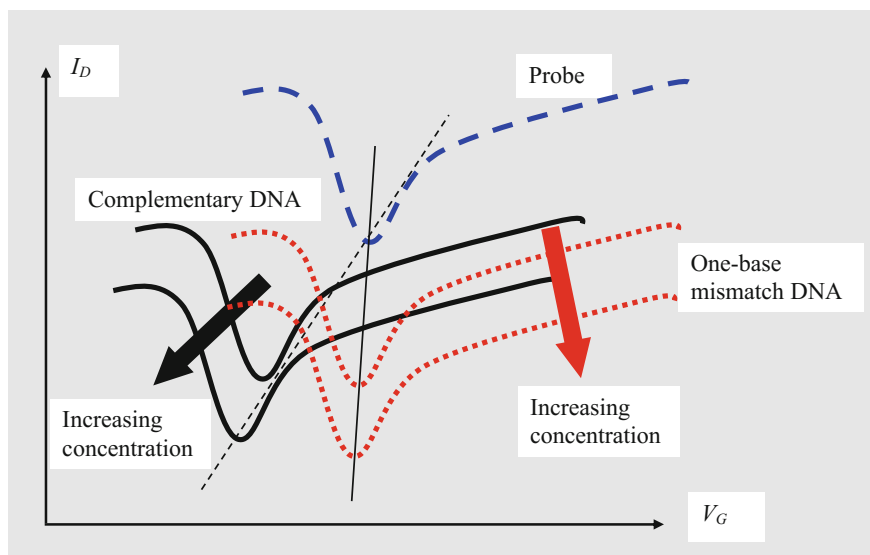


**Fig. 1.92** DNA hybridization and one-base mismatch detection

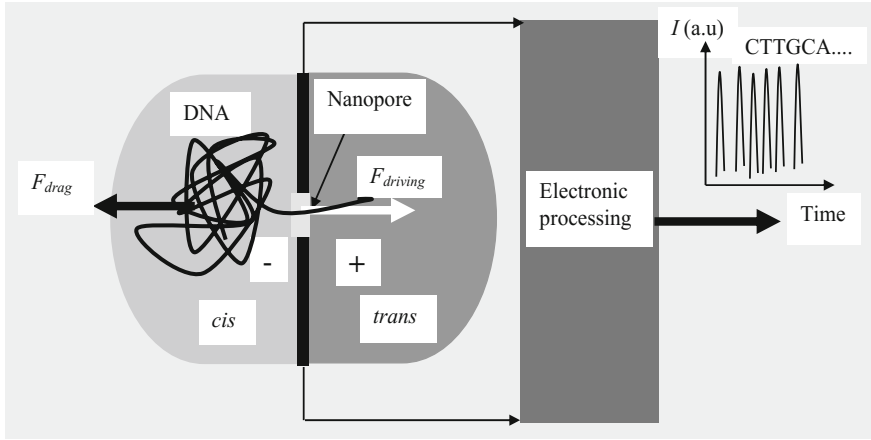


**Fig. 1.93** DNA nanopore sequencing circuit

The trapping of DNA depends on the concentration of the solution and the strength of the applied DC electric field, while the translocation is dependent on the applied field (bias) and many other factors (viscosity, ionic concentrations, etc.), which are generally referred to as DNA-pore interaction effects. The physical principle of DNA sequencing with the help of a nanopore, shown in Fig. 1.94, is based on the fact that translocation occurs in a certain time duration  $t_d$ , and during this time the strand of DNA disables the flow of ions through the pore. Because the nucleotide localized in the pore has a much slower velocity than the ions, the DNA nucleotide inside the pore blocks the ionic current, inducing a spike in the ionic current, with durations in the 300–1300  $\mu\text{s}$  interval (Zwolak and di Ventra 2008). The blockade current is the main source of information about the length of the DNA string and its bases' sequence, because each base has a different geometrical dimension and thus different  $t_d$ .

There are two forces that act on DNA: the driving force in the nanopore region, given by

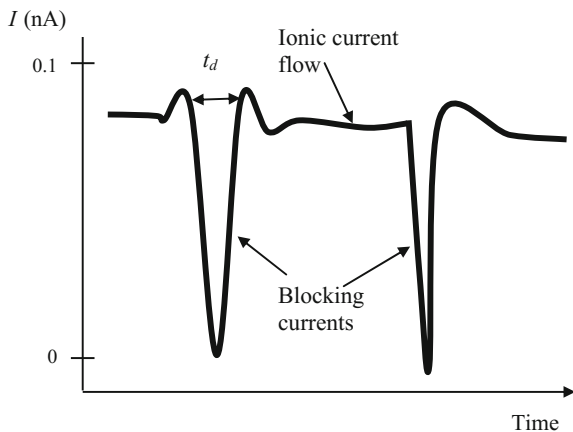
$$F_{driving} \cong -0.5eNE \quad (1.97)$$

where  $N$  is the number of DNA folds in the pore region and  $E$  is the applied electric field, and the drag force

$$F_{drag} \cong N\gamma v \quad (1.98)$$

expressing the nanopore-DNA interaction. In (1.98)  $\gamma$  is a coefficient specific for the surface of the contact area between DNA and the pore and  $v$  is the DNA velocity. For a constant velocity  $v$ , an equilibrium is reached between the dragging and driving force, which requires

**Fig. 1.94** A schematic behavior of the DNA blocking current



$$F_{drag} = F_{driving} \quad (1.99)$$

An enhanced sensitivity of DNA sequence detection is achieved in the transverse electronic current method, in which two DC biased electrodes are added on the two sides of the nanopore, as illustrated in Fig. 1.95, and the transverse current is monitored.

The parallel electric field, denoted by  $E_{\parallel}$  in Fig. 1.95, drags the DNA through the nanopore, while the transverse field,  $E_{\perp}$ , contains the DNA sequencing information, since each base has a very distinct current signature (Zwolak and di Ventra 2008). More precisely, as suggested by Fig. 1.96, each nucleotide translocating through the nanopore has a distinct electronic signature of the bases that is imprinted in the

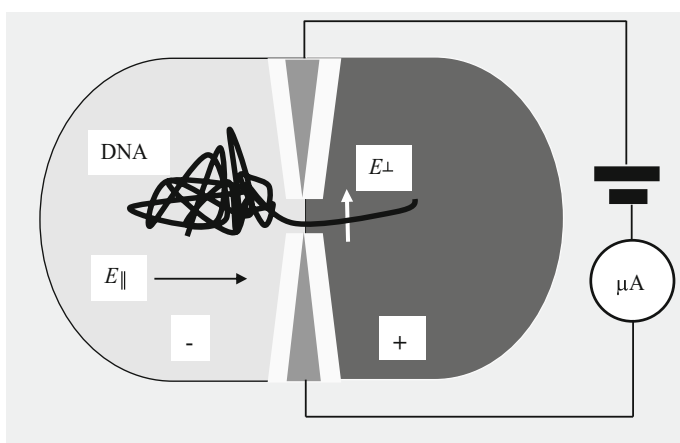
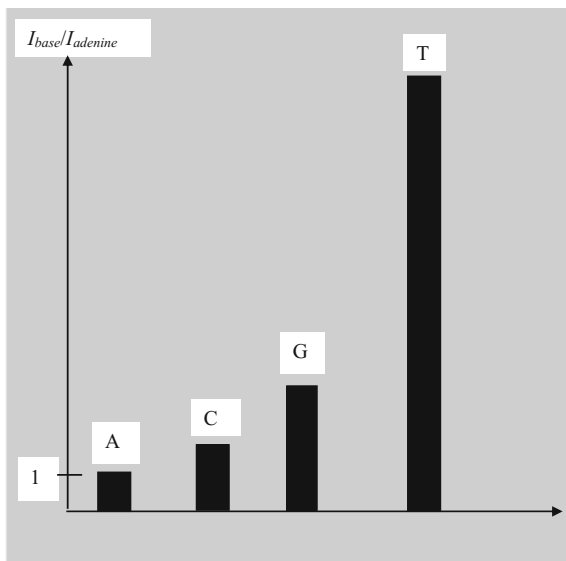


**Fig. 1.95** DNA sequencing using the transverse current method

**Fig. 1.96** Amplitudes of base currents



transverse current. The origin of this important distinction between the transverse currents corresponding to different DNA bases is the Fermi level position with respect to the HOMO and LUMO, and the DOS values, since the bases have different spatial extent and thus different extended molecular orbitals. The nanopore current (Zwolak and di Ventra 2008) is given by:

$$I \cong e^2 \Gamma_L(E_F) \Gamma_R(E_F) V / [\pi \hbar (E_F - E_N)^2] \quad (1.100)$$

where  $\Gamma_L$  and  $\Gamma_R$  are coupling coefficients, which are very different for each base due to their different shapes, corresponding wavefunctions and Fermi levels. The three billion bases of a human ssDNA could be sequenced in about 7 h using the transverse current sequencing technique (Zwolak and di Ventra 2008), but the main disadvantage of this method is the noise, especially the ionic noise.

Graphene is used in nanopores because it is the thinnest known material, other solid-state nanopores being 100 times longer than the distance between two bases, which is of 0.5 nm. Few-layer graphene nanopores with diameters of 2–20 nm have been produced (Schneider et al. 2010; Merchant et al. 2010).

At the beginning of this section we have pointed out that graphene and its various forms (GO, RGO, aerogels) are able to detect gases with unprecedented sensitivity. We refer here to the gas sensor as biosensor for harmful gases, which are able to destroy life in a very short time. In general, the physical mechanism for detection of these dangerous gases is gas adsorption, which produces a change in the conductivity of graphene due to the local doping.

There are many types of sensors on pristine graphene (see the examples above), graphene oxide (GO), reduced oxide graphene (RGO) or graphene aerogels

(Varghese et al. 2015). Pristine graphene gas sensors are so sensitive that they can detect the adsorption or desorption of a single gas molecule from the graphene surface (Schedin et al. 2007). The sensing mechanism is the change in graphene resistivity due to local doping induced by the gas molecules. In particular, graphene detection of  $\text{NO}_2$  reaches an outstanding performance of 0.1 ppm.

Graphene sensors in a Hall bar configuration were used also to understand the type of doping induced by various molecules. It was found out that *n*-type doping is produced by  $\text{NH}_3$ , CO and ethanol, while *p*-type doping is induced by  $\text{NO}_2$ ,  $\text{H}_2\text{O}$  and iodine. The detection limit of Hall bar gas sensor is 1 ppb, concentration at which the relative resistivity of graphene changes by  $\Delta\rho/\rho \propto 10^{-4}$ .

The decrease of contact resistance at 100  $\Omega$  in few graphene layers devices due to adsorption and desorption of a single  $\text{NO}_2$  molecule is also used for sensitive detection. In this case, the difference in resistance, of 2.5  $\Omega$ , is very large considering that a single molecule is attached or detached from the graphene surface.

Other forms of graphene are able to detect harmful gases with a very high sensitivity and selectivity. For example, flakes of GO deposited on a Pt IDT electrode array by the drop casting method detect  $\text{NO}_2$  with a sensitivity of 20 ppb (Prezioso et al. 2013). In this sensor, represented schematically in Fig. 1.97, detection is associated to the oxygen functional groups at the GO surface, on which  $\text{NO}_2$  is mainly adsorbed.

A promising path for highly sensitive gas sensors is offered by 3D graphene aerogel-ZnO composites (Liu et al. 2015b). Semiconductor oxides, such as ZnO, are extensively used in gas sensors, but ZnO sensors work at high temperatures due to the high activation energy required for surface adsorption and redox reaction

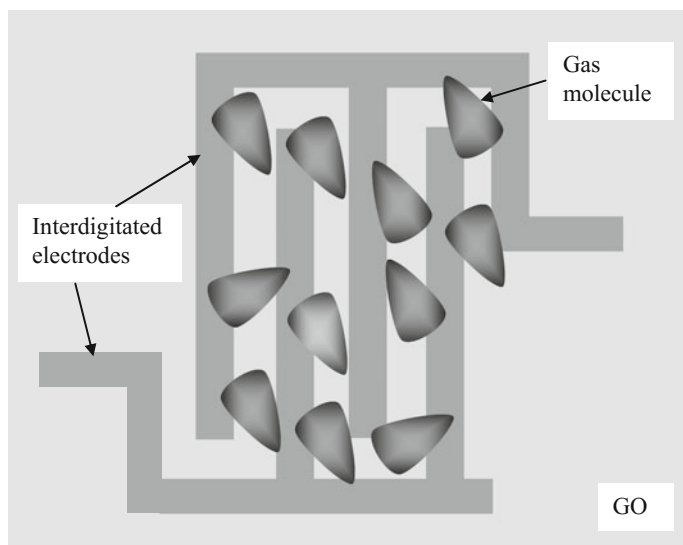


**Fig. 1.97** GO gas sensor

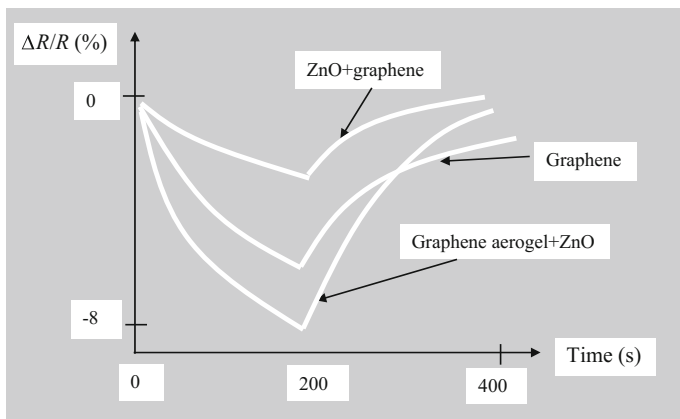


**Fig. 1.98** Typical response in time of graphene aerogel+ZnO in comparison with other related sensors at 50 ppm  $\text{NO}_2$  gases (after Liu X et al. 2015a, b)

between ZnO and the gas. On the other hand, ZnO spheres in combination with graphene aerogel display different physical sensing mechanisms, which do not require high temperatures. The graphene aerogel creates a conductive matrix between ZnO spheres, necessary for sensing and for avoiding also agglomeration between spheres. The sensing process as well is enhanced significantly due to the large specific surface of graphene aerogel. Thus, the graphene aerogel-ZnO composite works as gas sensor at room temperature, with fast response and recovery times. For example, the sensitivity of this sensor for  $\text{NO}_2$  detection is 50 ppm at room temperature, the resistance variation  $\Delta R/R$  at 200 ppm of  $\text{NO}_2$  being of 20%. The  $\Delta R/R$  dependence on time of ZnO+graphene, graphene and graphene aerogel and ZnO spheres is displayed in Fig. 1.98. Graphene aerogel+ZnO is faster than the graphene sensor and has a shorter recovery time due to the heterostructures formed between graphene and ZnO, which attract more electrons from graphene to  $\text{NO}_2$  via new conduction channels created in these heterostructures.

## 1.4 Graphene Photonics

Graphene is a material with tunable optical properties, and as such has many photonic applications. We have pointed out in the above section that the density of carriers in graphene, and hence its conductivity, is modulated by an applied DC voltage. In photonics this means that the index of refraction, the absorption coefficient, the optical nonlinearities, and plasmonic resonances are all dependent on the applied DC voltage. It was never simpler to tune the optical response than using photonic devices based on graphene.



Intrinsic graphene has a universal optical conductance (Low and Avouris 2014)

$$G_{opt} = e^2/4\hbar \quad (1.101)$$

and thus an absorption

$$\alpha\pi = 2.3\% \quad (1.102)$$

where  $\alpha = e^2/\hbar c \cong 1/137$  is the fine structure constant. Equation (1.102) shows that the absorption is independent of the wavelength of light, in strong contradiction with semiconductors, where absorption has a narrow band centered on the wavelength that corresponds to the bandgap.

The optical conductivity has a more general expression (Sensale-Rodríguez et al. 2013) and is dependent on the type of optical transition: intra- or interband, as illustrated in Fig. 1.99.

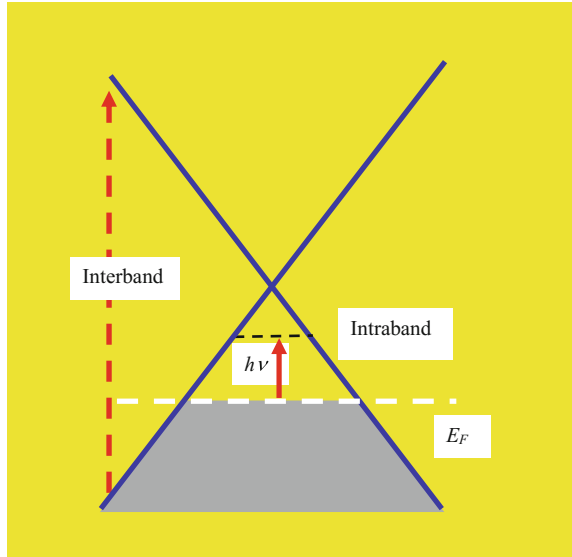
We have

$$\sigma_{intra} = ie^2E_F/[\pi\hbar^2(\omega + i/\tau)] \quad (1.103a)$$

and

$$\sigma_{inter} = (ie^2\omega/\pi) \int_0^\infty dE[f(E - E_F) - f(-E - E_F)]/[(2E)^2 - (\hbar\omega + i\Gamma)^2] \quad (1.103b)$$

**Fig. 1.99** Graphene optical transitions



where  $\tau$  and  $\Gamma$  are the momentum relaxation time and broadening of interband transitions, respectively, and  $f(E) = 1/[(\exp(E - \mu_c)/k_B T) + 1]$  is the Fermi distribution, with  $\mu_c$  the chemical potential describing charge accumulation in graphene. This latter parameter is related directly to the applied voltage  $V$  via

$$\mu_c = \hbar v_F \sqrt{(\pi \epsilon_{ox} / e d_{ox})(V - V_{Dirac})} \quad (1.104)$$

where  $\epsilon_{ox}$  is the permittivity of dielectric,  $d_{ox}$  its thickness and  $V_{Dirac}$  the Dirac voltage.

Because the Fermi level is tunable via the carrier density:  $E_F = (\pi n)^{1/2} / h$ , which in turn is changed via the electrostatic doping induced by the gate voltage, the optical conductivity is DC tunable. So, via the Fermi energy shift and the chemical potential dependence on the applied voltage, the optical absorption in graphene depends on the DC voltage since  $\sigma$  is directly proportional to absorption.

When the optical frequency is very high, including the visible, UV, and far IR ranges, the conductivity becomes  $e^2/4\hbar$ , independent of frequency.

Another consequence of the direct proportionality between  $\sigma$  and absorption is that the index of refraction becomes dependent on the gate voltage via the formula:

$$n_{gr}(V_G) = \sqrt{1 - i\sigma(V_G)/(\omega \epsilon_0 t_{gr})} \quad (1.105)$$

where  $t_{gr} = 0.34$  nm is the thickness of graphene. The dependence  $n_{gr}(V_G)$  was recently experimentally proven (Xu et al. 2015) at 1550 nm. In these experiments graphene was transferred on a Si/SiO<sub>2</sub> substrate, where the doped Si substrate played the role of the backgate. The measurements were performed in a reflection configuration, the change in the power reflectivity with respect to the value  $R_0$  in the absence of graphene being calculated with the formula

$$\Delta R/R_0 = \pi t_{gr} \text{Re}[(1 - n_{gr}^2)(1 + r_0)^2/(r_0 \lambda)] \quad (1.106)$$

where  $r_0$  is the substrate reflectivity without graphene.

The dependence of the index of refraction of graphene on the applied gate voltage and the corresponding chemical potential is depicted in Fig. 1.100. This figure shows that the index of refraction is strongly tunable with the applied gate voltage. At zero gate voltage, the real part of the refractive index of graphene is 3, but can be strongly modulated by the backgate voltage even below 1. This very strong index of refraction modulation can be used in several photonic devices since up to a chemical potential value of 0.5 eV graphene behaves like a dielectric and beyond this value like a metal. This reversible transition between “dielectric” and “metallic” graphene is the key of many graphene-based modulators.

The optical constants of graphene in the visible spectral range can be deduced from the general formula of an absorbing medium with extinction coefficient  $k$  and refractive index  $n$  having thickness  $t_{gr}$  (Bruna and Borini 2009):

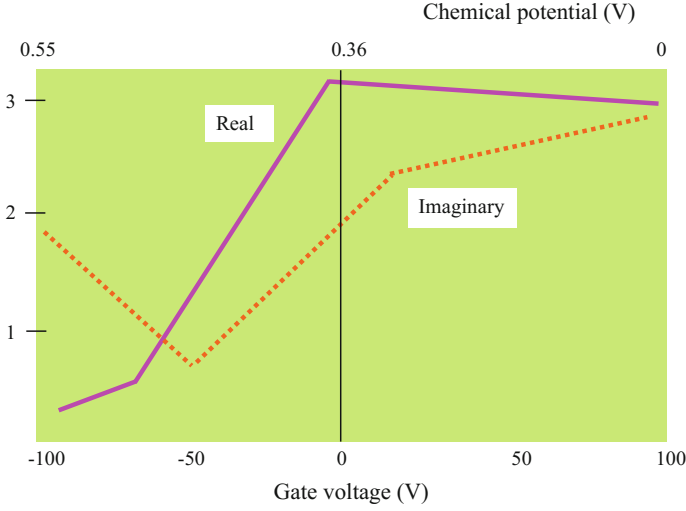


**Fig. 1.100** Graphene refractive index as a function of the gate voltage (after Xu et al. 2015)

$$4\pi k/\lambda = -(nt_{gr})^{-1} \ln[(I/I_0)(1-R)^{-1}] \quad (1.107)$$

Because in the graphene monolayer

$$I/I_0 \approx (1 - \alpha\pi) \quad (1.108)$$

and  $1 - R \cong 1$ , we obtain

$$k = -(\lambda/4\pi nt_{gr}) \ln(1 - \pi\alpha) \equiv C_1 \lambda/n \quad (1.109)$$

where  $C_1 = 5.446 \mu\text{m}^{-1}$ . This is a simple relation between the index of refraction and the extinction coefficient. Assuming that  $n$  is constant in the visible domain,  $n = 3$ , it follows that  $k = C_1 \lambda/3$ .

The optical transmission and reflection in graphene are also tunable by the gate voltage. The optical transmission depends on the optical conductance  $G_{opt}$  as (Bonaccorso et al. 2010):

$$T = [1 + G_{opt}N/(2\epsilon_0 c)]^{-2} \quad (1.110)$$

where  $N$  is the number of graphene layers. Because the sheet resistance  $R_s$  is determined by the DC gate-dependent conductivity via:

$$R_s = [\sigma(V_G)N]^{-1} \quad (1.111)$$

it follows that

$$T(V_G) = [1 + Z_0 G_{opt}/2R_s \sigma(V_G)]^{-2} \quad (1.112)$$

where  $Z_0 = 1/\epsilon_0 c = 377 \, \Omega$ . When the gate voltage  $V_G$  is nearly zero, the conductivity is  $4e^2/h$ ,  $R_s = 6 \, \text{k}\Omega/\text{sq}$  and  $T = 97.7\%$  for  $N = 1$ , the graphene monolayer being more transparent than ITO. However, the sheet resistance is too high; it should be around  $100 \, \Omega\text{--}200 \, \Omega/\text{sq}$ .

One method to reduce the sheet resistance is to dope graphene, and to transform it into a transparent conductor, with reduced surface resistance and a high transmission in an as-large-as-possible optical bandwidth. Because graphene-based transparent electrodes have important applications in touch displays, solar cells, and transparent loudspeakers, heaters or actuators (Zheng and Kim 2015) the doping process will be described briefly below.

We have already discussed about graphene doping in several contexts. First, the role of doping is to engineer the Fermi level in graphene, and thus to control the charge carrier density. By shifting the Fermi level away from the Dirac point, we are able to decrease the sheet resistance of graphene. The doping could be *p*-type or *n*-type, depending on the doping method. We have already mentioned the electrostatic doping of graphene, which is one of the most important properties of graphene and 2D materials, and in which the Fermi level is shifted by a gate voltage, but electrostatic doping is not applicable for transparent electrodes. Other doping methods were mentioned in connection with graphene functionalization. Here we discuss the main methods of doping for transparent electrodes.

The wet doping is referred to as spin coating or dip coating of graphene in a solution. Acid treatment is a typical doping method, and the nitric acid ( $\text{HNO}_3$ ) is used extensively for this purpose, produces a *p*-type doping and a shift of the Fermi level of up to 0.8 eV depending on its concentration (see Fig. 1.101). Halogenating agents such as  $\text{SOCl}_2$ , produce also *p*-type doping of graphene and reduces the sheet resistance with 50–80%. Auric chloride  $\text{AuCl}_3$  is also a *p*-type dopant. In the case of multilayer graphene, the sheet resistance decreases with 80% as a result of this doping method, becoming less than  $100 \, \Omega/\text{sq}$ . Note that the optical transmittance is preserved beyond 90%.

Another method of doping is hybridization with carbon nanotubes, metal nanowires, nanorods, and metal grids. For a good review of doping methods applied for graphene as transparent conductor see Zheng and Kim (2015, Chap. 4).

Nonlinear effects in graphene are very strong and are caused by the interaction between optical fields and electrons on the outer shell of carbon atoms, which shifts the electron cloud from its initial position around the nucleus and generates a net polarization. At moderate optical fields, there is a linear relation between the polarization  $P$  and the electric field  $E$  (Bao and Loh 2012)

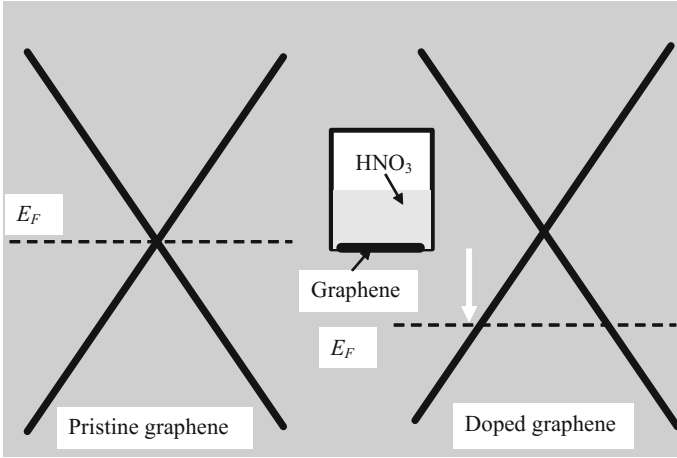


**Fig. 1.101** Graphene doping using nitric acid

$$P = \epsilon_0 \chi^{(1)} E \quad (1.113)$$

where  $\chi^{(1)}$  is the first order linear susceptibility. At stronger optical fields, however,

$$P = \epsilon_0 (\chi^{(1)} + \chi^{(2)} E^2 + \chi^{(3)} E^3 + \dots) \quad (1.114)$$

where  $\chi^{(2)}$  and  $\chi^{(3)}$  are the second- and third-order nonlinearities, respectively, which are related to nonlinear phenomena such as saturable absorption, self-focusing or two-photon absorption. Graphene displays very large third-order nonlinearity, of  $10^{-7}$  esu, and a very large Kerr coefficient and optical damage threshold, with orders of magnitude larger than in semiconductors (see Table 1.6).

In relation (1.113), the real part of  $\chi^{(1)}$  is associated to the real part of the refractive index, while the imaginary part is linked to optical loss or gain. Graphene modulators are based on the tunability of the real part of  $\chi^{(1)}$  with an applied DC field, i.e. the variation of the index of refraction with the DC voltage. We have seen above that when the gate voltage, i.e. the chemical potential, varies graphene undergoes a reversible transition from a “dielectric” to a “metallic” state. If

**Table 1.6** Nonlinear optical properties of graphene and other materials (Bao and Loh 2012)

Material	Refractive index	Optical damage threshold (MW/cm <sup>2</sup> )	Third order nonlinearity (esu)	Kerr nonlinear coefficient at 1.55 $\mu$ m
Graphene	2.6–3	$3 \times 10^6$	$10^{-7}$	$10^{-11}$
h-BN	2.2	500	$1.36 \times 10^{-14}$	–
GaAs	3.4	45	$4 \times 10^{-8}$	$3.3 \times 10^{-17}$
Si	3.44	500	$5 \times 10^{-11}$	$4.5 \times 10^{-18}$

graphene is integrated along an optical waveguide, so that light propagates along graphene and strongly interacts with this material, such a transition produces light modulation. For a recent review of optical modulators based on graphene see Luo et al. (2015).

The simplest modulator, shown in Fig. 1.102, consists of a graphene sheet integrated with a slightly doped Si bus waveguide (Liu et al. 2011), the device having an area of  $25 \mu\text{m}^2$ . Graphene is separated from the doped Si by an  $\text{Al}_2\text{O}_3$  dielectric. This modulator is based on the fact that graphene is a DC-voltage-controlled absorption medium, which modulates the transmission of the Si bus waveguide. For small drive voltages, the Fermi level in graphene is near the Dirac point, so that interband transitions are allowed and the transmission of photons with a wavelength of  $1.53 \mu\text{m}$  is attenuated due to absorption. For larger drive voltages, interband transitions are forbidden and the transmission through the bus waveguide increases. A modulation depth of  $0.1 \text{ dB}/\mu\text{m}$  was achieved in this way in the bandwidth  $1.35\text{--}1.6 \mu\text{m}$ , the operation bandwidth being of about  $1 \text{ GHz}$ .

A similar double-layer graphene modulator operating around  $1 \text{ GHz}$  has an enhanced modulation depth, of  $0.16 \text{ dB}/\mu\text{m}$ , at a drive voltage of  $5 \text{ V}$ . The entire graphene- $\text{Al}_2\text{O}_3$  dielectric-graphene structure is functioning as a *p-i-n* junction to minimize the losses (Liu et al. 2012). This type of modulator is schematically represented in Fig. 1.103. The state-of-the-art of optical modulators based on Si and graphene using the concepts described above is a broadband  $10 \text{ Gb/s}$  modulator at telecom wavelength (Hu et al. 2014).

A double layer formed from two graphene monolayers separated by a dielectric in a FET-like configuration and integrated on a Si waveguide is able to work simultaneously as modulator and photodetector (Youngblood et al. 2014). In this device, illustrated in Fig. 1.104, the bottom graphene monolayer acts as a channel, playing also the role of an optical absorber where photocarriers are generated, while the top graphene electrode is an optical transparent gate able to tune the optical and electrical behavior of the graphene channel. The thickness of the  $\text{Al}_2\text{O}_3$  gate dielectric is  $100 \text{ nm}$ . The drain and source contacts are made from different metals,

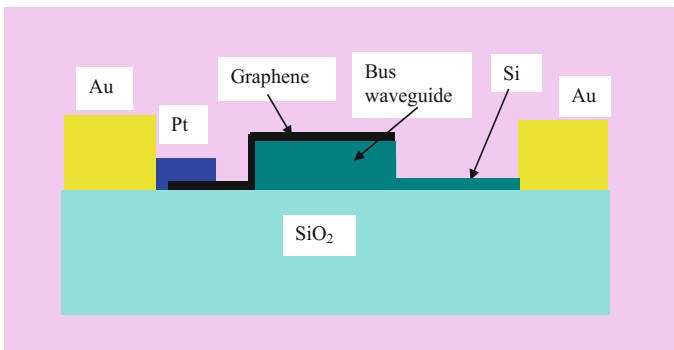
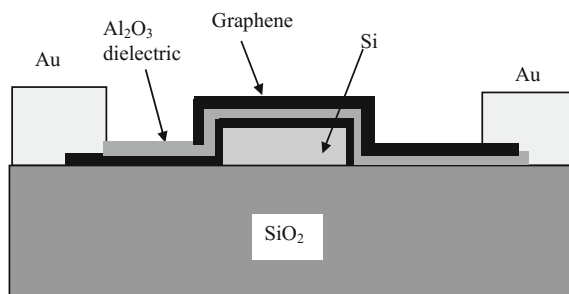


**Fig. 1.102** Optical modulator based on a slightly doped Si waveguide

**Fig. 1.103** Optical modulator based on double-layer graphene

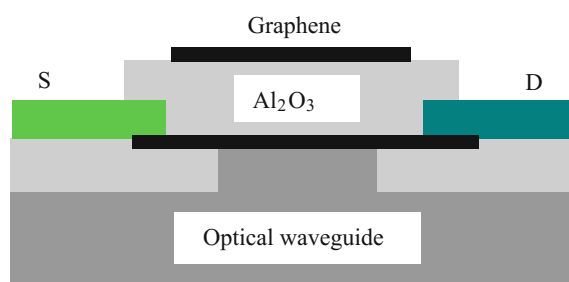


Ti/Au and Pd/Au, with different workfunctions, these electrodes doping the graphene channel *n*-type and, correspondingly, *p*-type. As a result, if the middle of the graphene channel is tuned to the Dirac point, the entire device mimics a lateral *p-i-n* junction, so that a built-in field located in the channel separates the photocarriers. The device displays a modulation depth of 64% in the GHz bandwidth and a responsivity of 57 mA/W.

Another photonic device is presented in Fig. 1.105, where a graphene–graphene capacitor is integrated with a silicon nitride ring resonator coupled to a bus waveguide. The capacitor, consisting of two graphene monolayers separated by 65 nm  $\text{Al}_2\text{O}_3$  dielectric, is grown on top of a portion of the ring resonator. When both graphene sheets are unbiased, the bus waveguide and ring resonator, with a 300 nm gap between them, are practically decoupled due to the high losses in the ring caused by opaque graphene; light propagation through the bus waveguide is almost unimpeded. On the other hand, when a DC bias is applied on the graphene capacitor, the transmission changes dramatically, from  $-8$  to  $-25$  dB at  $-50$  V, so that light propagation through the bus waveguide is obstructed. In this case, graphene is electrostatically doped, the shift of the Fermi level preventing light absorption, and the ring resonator and bus waveguide become coupled. Light modulation is caused by graphene-tuned interference in the coupling region between the ring and the bus waveguide. The device has 30 GHz bandwidth operation, a 15 dB tuning of cavity transmission being achieved with only 10 V swing (Phare et al. 2015).

All the above optical modulators are based on interband transitions, but modulation at higher frequencies, up to 3 THz, is possible using intraband transitions. The

**Fig. 1.104** Modulator and photodetector based on graphene



working principle of such modulators is similar to that of optical modulators in the visible or IR spectral regions. Graphene at the Dirac point is transparent, having zero charge density and behaving like a “dielectric” such as ITO in the visible spectrum. As a result, the absorption has low values and the transmission  $T \rightarrow 1$ . On the contrary, when a gate voltage is applied, the density of carriers increases and graphene tends to behave as a “metal”, such that  $T \rightarrow 0$  (Sensale-Rodríguez et al. 2012). A THz modulator working on this principle is represented schematically in Fig. 1.106. The modulation depth is 64% with the insertion loss of 2 dB at 0.62 THz.

All-optical spatial THz modulators can be successfully implemented using graphene transferred on Ge. Ge was chosen as substrate instead of Si due to its higher bulk mobility, and thus an increased surface mobility and better modulation performances. In this graphene-based modulator, a wideband modulation, from 0.25 up to 1 THz, was obtained under laser pumping at 1550 nm (Wen et al. 2014).

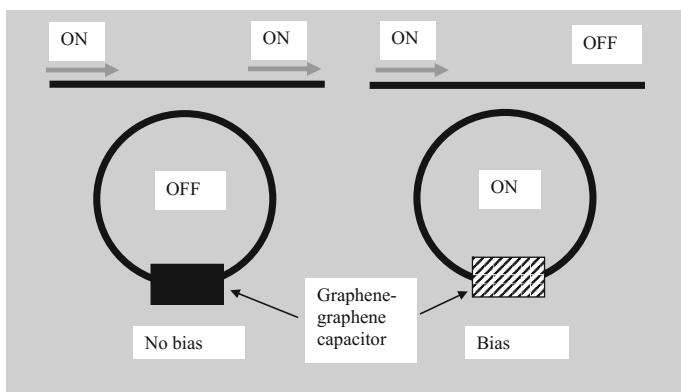


**Fig. 1.105** Graphene modulator with a bandwidth up to 30 GHz

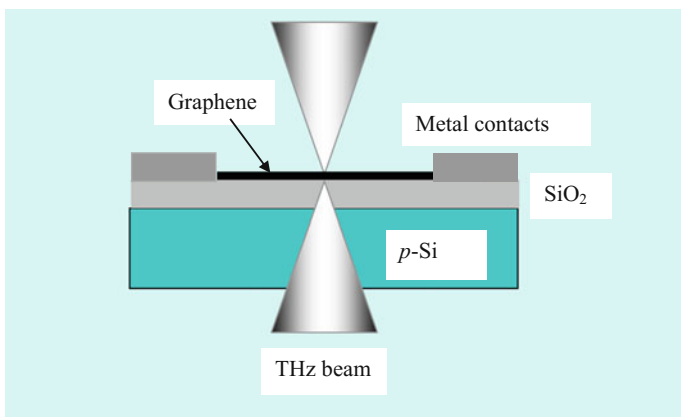


**Fig. 1.106** THz modulator



The modulation depth is impressive, reaching 94%, and the measured modulation speed is 200 kHz at a 340 GHz carrier. The modulator is represented schematically in Fig. 1.107 and its modulation principle is described in Fig. 1.108. No bias needs to be applied on graphene for modulation purposes in this case. Instead, at a laser pumping power of 400 mW, both graphene and Ge layers show a very large attenuation of the THz wave due to the photogenerated free carriers, which form a thin conductive layer. But, in dark, i.e. when the optical power is reduced to 0, the transmission of THz waves reaches 50%. In this way, THz waves are modulating the optical carrier at 1550 nm.

The transmission is given by

$$T(E) = [1 + 0.5\alpha\pi\sigma(E)]^{-2} \quad (1.115)$$

where  $\alpha$  is the fine structure constant and the nonlinear conductivity can be expressed as

$$\sigma(E) = \sqrt{(1 + \sigma_3(E)H_2)^2 + \sigma_3^2(E)H_1^2} \quad (1.116)$$

**Fig. 1.107** All optical THz modulator

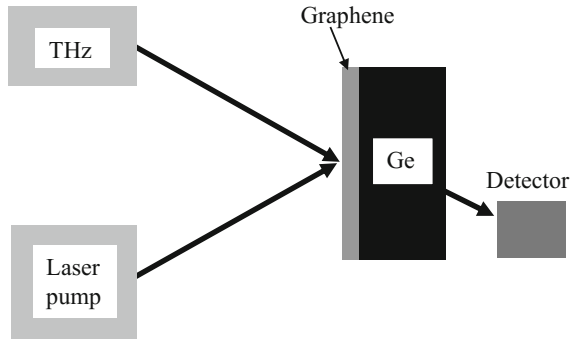
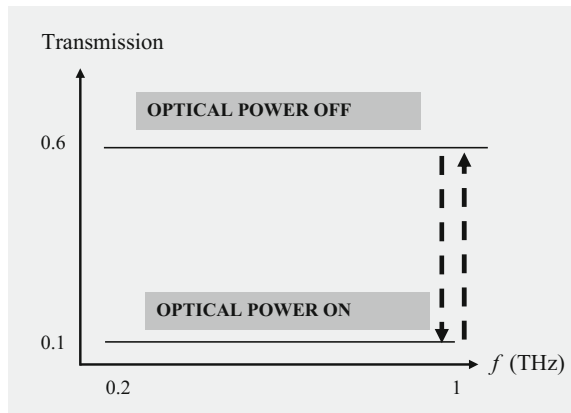


**Fig. 1.108** Principle of the all-optical THz modulator



where

$$\sigma_3(E) = e^2 v_F^2 E_0^2 / \hbar^2 \omega^4, H_1 = (13/48)N(1/2) - (2/3)N(1) + (45/48)N(3/2), H_2 = 2N(1), \quad (1.117)$$

$E_0$  is the strength of the incident field,  $N(x) = \tanh(x\hbar\omega/2k_B T)$  and  $T$  is the temperature; the terms  $H_1$  and  $H_2$  originate from the time averages of the nonlinear currents of the first and third order, respectively, in graphene. This model is precise enough to fit the experimental data.

Photodetection in graphene is due to interband and intraband absorption and generation of photocarriers. Since graphene absorption is independent of wavelength, this material can be used for photodetectors in a wide range of wavelengths, from microwaves up to visible, infrared and even ultraviolet. Various types of graphene, such as inks, flakes, or aerogels can be used for photodetection in specific types of devices, but there are also photodetectors fabricated at the wafer scale. The most common device for photodetection is the graphene FET.

There are several physical mechanisms for light detection using graphene (Sun and Chang 2014), the photoelectric effect being mostly used for this purpose. According to the photoelectric effect, excitons are formed when photons excite the graphene monolayer, which are separated in photoexcited carriers (electrons and holes) by the built-in field at the graphene-metallic electrode interfaces. The basic metal-semiconductor-metal-like (MSM-like) configuration of a graphene photodetector is shown in Fig. 1.109. Different configurations for electrodes, such as interdigitated electrodes, can be used, the substrate can be doped and then can act as the backgate, a top gate with the corresponding biasing circuit can be added to the configuration in Fig. 1.109, but in principle this is the basic configuration for graphene photodetection.

The photocurrent in graphene is given by

$$I_{ph} = e\mu AV\Delta n \quad (1.118)$$

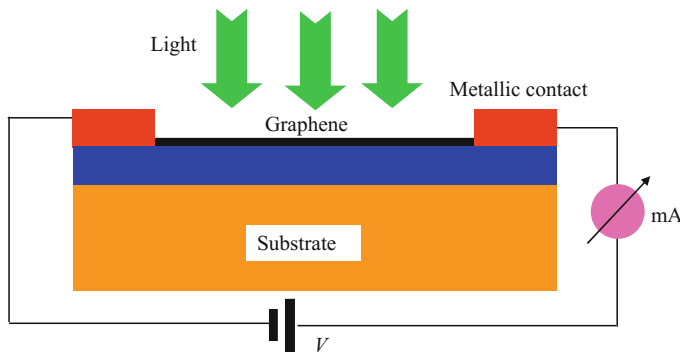


**Fig. 1.109** MSM-like basic configuration of a graphene photodetector

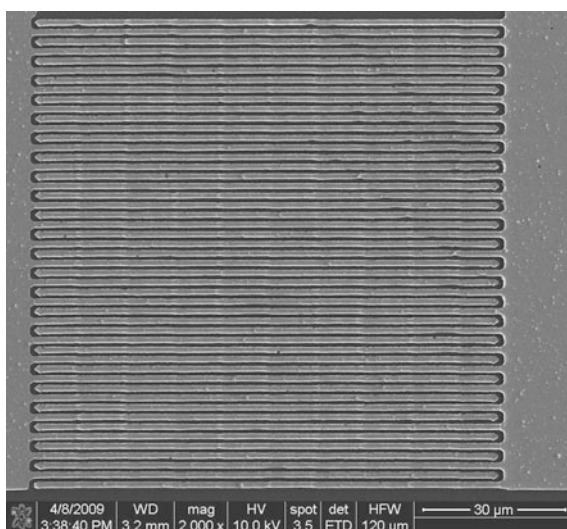
where  $A$  is the cross section,  $V$  is the bias voltage,  $\mu$  is the mobility of carriers, and  $\Delta n$  is the density of photocarriers. The carrier mobility in graphene is high, but the low absorption and the short lifetime of photocarriers generate low quantum efficiency in graphene and, despite many efforts to alleviate these issues, there are other 2D materials such as  $\text{MoS}_2$  where the quantum efficiency is much higher. Therefore, graphene photodetectors have average performances and their most important advantage is the large bandwidth. The responsivities of graphene photodetectors are below 10 mA/W, which is a modest performance taking into account that photodetectors based on 2D transition metal dichalcogenides have responsivities of  $10^6$  A/W and even higher.

Graphene photodetection in a very large spectral bandwidth: ultraviolet, visible and near infrared, was demonstrated with graphene inks (GI) or GI functionalized with Au, Ag, or Au nanoparticles further encapsulated with bovine serum albumin (BSA) and deposited on interdigitated electrodes (IDTs) fabricated on a silicon dioxide/silicon substrate (Radoi et al. 2010). In contrast to gold-functionalized GIs, which have responsivities better than 1 mA/W at a 0.1 V bias over the huge bandwidth extending from 215 to 2500 nm, Ag-functionalized inks show at least a four-fold increased responsivity, with a record value of 13.7 mA/W in near infrared.

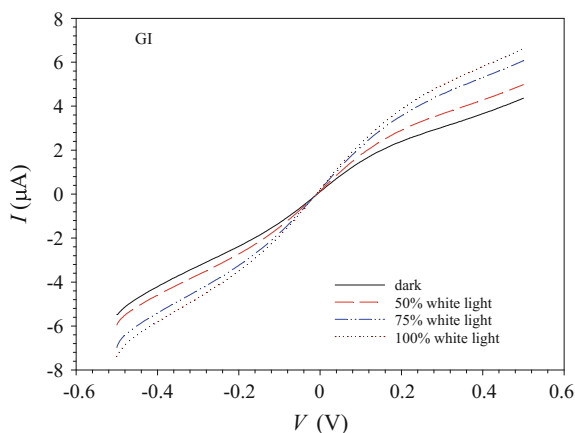
The IDT structures are fabricated on 0.5- $\mu\text{m}$ -thick  $\text{SiO}_2$  grown over a high resistivity silicon wafer ( $\sim 8 \text{ k}\Omega \text{ cm}$ ). The Ti/Au IDT electrodes are fabricated from Ti with a thickness of 60 nm, the gold thickness being 240 nm. The width of an IDT electrode is 3  $\mu\text{m}$  and the gap between adjacent digits is 1  $\mu\text{m}$ . The SEM photo of 24 IDTs electrodes is displayed in Fig. 1.110.

Figure 1.111 illustrates the response of GI at white light. For the UV-VIS spectrum, the photodetector was illuminated with a halogen lamp terminated with

**Fig. 1.110** SEM photo of graphene ink photodetector (from Radoi et al. 2010)



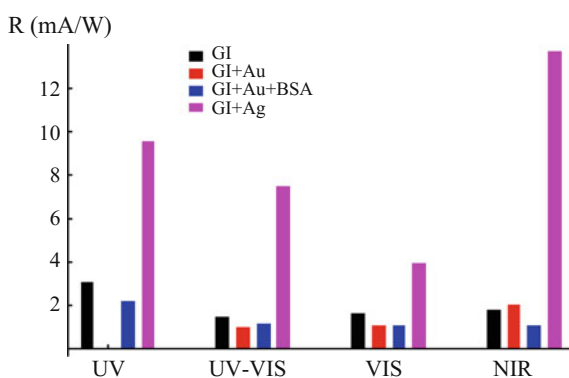
**Fig. 1.111** GI response at white light with various intensities (from Radoi et al. 2010)



an optical fiber, having a power of 43  $\mu\text{W}$  for the visible (VIS) spectral domain and a deuterium lamp with a power of 7  $\mu\text{W}$  for ultraviolet (UV), both lamps covering the spectrum 215–1500 nm. For near-infrared (NIR), a tungsten halogen lamp with a power of 0.5 mW was employed, for an extension of the optical spectrum from 1500 to 2500 nm. Thus, all optical lamps cover the huge spectral spectrum from 215 up to 2500 nm. The optical responsivities of GI and GI functionalized with nanoparticles from UV up to FIR are displayed in Fig. 1.112.

There are many reviews explaining how the low absorption of graphene can be increased using optical cavity integration, optical waveguide integration, or plasmonic excitations (Koppens et al. 2014). These methods are well-known solutions for improving the performances of photodetectors of many types, so that we will not present them in detail here. But, as we have pointed out, graphene FETs act as electromagnetic detectors in the THz region when integrated with an antenna, and in the IR region if the transistors are integrated with antennas or excited via waveguides (Li et al. 2014).

**Fig. 1.112** Responsivities of graphene inks over different spectral regions at the constant bias of 0.1 V (from Radoi et al. 2010)



The best performance graphene photodetector is obtained by band structuring, which introduces electronic trapping centers and induces a bandgap in graphene (Zhang et al. 2013). In this way, a responsivity of 8.61 A/W can be achieved, which is about three orders of magnitude higher than that of the majority of graphene photodetectors. This graphene photodetector is based on the physics of graphene; it does not just mimic (without much success) existing detecting solutions for other semiconductor photodetectors.

More precisely, a very thin Ti layer (2 nm) deposited on graphene and then removed after fabrication of a graphene dot-like array (see Fig. 1.113) induces a defect midgap states band (MGB) and a bandgap. The thickness of the Ti layer controls the average size of the graphene quantum dots. Thicker Ti layers produce smaller sizes of quantum dot-like features. For example, for a Ti thickness of  $t = 20$  nm, the average dimension of the quantum dots is  $W = 7.5$  nm, while for  $t = 2$  nm the average dimension increases to 20.5 nm. However, smaller features generate higher bandgaps, according to the formula

$$E_g \cong \hbar v_F / W, \quad (1.119)$$

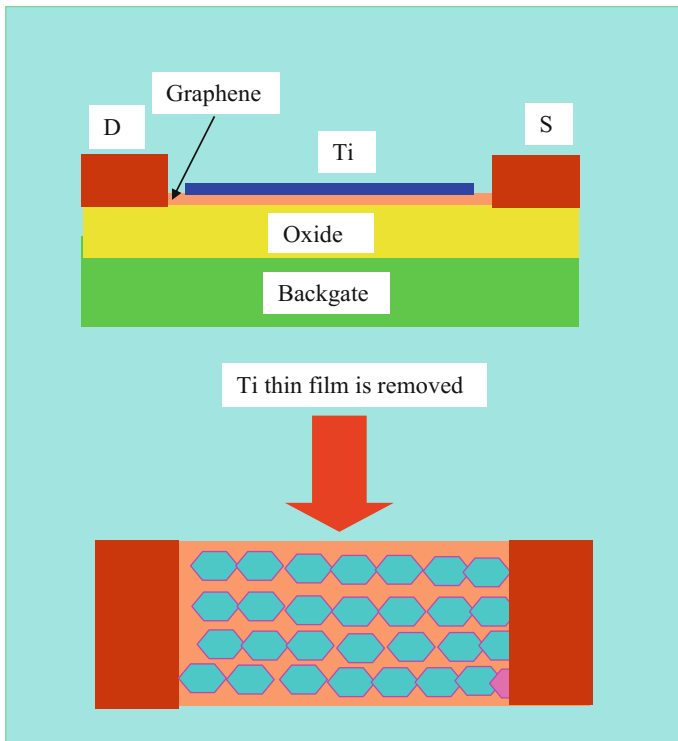


**Fig. 1.113** Photodetector based on a graphene quantum dot-like array

while the average crystallite size of the quantum dots,  $L_c$ , are determined from the Raman analysis via the ratio of the intensities of the  $D$  and  $G$  bands, denoted by  $I_D$  and  $I_G$ , respectively:

$$L_c \cong (2.4 \times 10^{-10}) \lambda^4 (\text{nm}) (I_D/I_G)^{-1}. \quad (1.120)$$

There are two mechanisms competing for a high photoresponse

- (i) impact ionization in the quantum-dot arrays; a photoexcited electron with a high energy relaxes to lower levels in the conduction band, exciting (one or few) carriers from the valence band into the conduction band;
- (ii) recombination of an electron from the conduction band with a hole in the valence band, associated with the excitation of an electron in the conduction band to a higher energy state based on the resulting energy in the recombination process (Auger recombination).

Impact ionization is more efficient than Auger recombination in confined quantum systems, such as quantum dots, and thus carrier multiplication occurs, i.e. more and more electrons are produced in the conduction band. This mechanism is called multi-excitation generation (MEG). The photoconductive gain is caused in this case by trapping of the photogenerated and the secondary electrons on MGB states, which allows few-times circulation of holes in the photoconductive channel before recombination.

With the following notations:  $n$  and  $m$  the electron populations in the conduction band and MGB,  $R$  the recombination time (equal to 1 ps),  $\alpha$  the capture rate of the MGB,  $\tau_1$  the lifetime of trapped electrons,  $\tau_t$  the transition time,  $\beta$  the photogeneration rate,  $\chi$  the number of electrons per absorbed photon due to impact ionization, and  $I$  the photodetected current, the relevant balance equations are:

$$dn/dt = \chi\beta - Rm - \alpha n = 0 \quad (1.121a)$$

$$dm/dt = \alpha n - m/\tau_1 = 0 \quad (1.121b)$$

$$n + m = I\tau_t/e \quad (1.121c)$$

From these, the capture rate is found as

$$\alpha \approx R(I/e\chi\beta)(\tau_t/\tau_1) \quad (1.122a)$$

and the quantum efficiency is

$$\eta = \alpha n/\beta \cong (I/e\chi\beta)(\tau_t/\tau_1). \quad (1.122b)$$

From experimental data it follows that  $\eta$  is about  $10^{-6}$  for  $\tau_1 = 30$  s and  $\tau_t = 250$  ns. The photoconductive gain is then

$$G = \eta(\tau_1/\tau_t). \quad (1.123)$$

This parameter depends on the energy of photons, and reaches 100 for a photon energy of about 2.3 eV.

The ultimate graphene photodetector, the configuration of which is represented in Fig. 1.114, is obtained by integrating the photodetector with an optical antenna, which works at visible and IR wavelengths. As an example, an antenna coupled to a graphene photodetector shows a responsivity of 17 nA/ $\mu$ W at 580 nm and has a signal-to-noise ratio (S/N) of 200 (Chakraborty et al. 2014).

In order to avoid the main drawbacks of graphene photodetectors: low absorption and short lifetime of photocarriers (of about 1 ps), mid infrared graphene detectors can be integrated with antennas. In such a configuration, illustrated in Fig. 1.115, the role of the metallic antenna array is to improve light absorption and to enhance the yield of photocarrier collection by increasing the photocarrier lifetime (Yao et al. 2014). The antenna array is formed from end-to-end coupled antennas and has a resonance in mid-infrared, at 4.45  $\mu$ m.

As a result of integrating the antenna array, the responsivity of the graphene photodetector increases to 0.4 V/W, which is orders of magnitudes higher than the same parameter in graphene photodetectors without antenna (2 mV/W). The gap size  $g$  between antennas is about 100 nm. The antennas are made of Pd/Au, the Pd layer, with a thickness of 10 nm being used to decrease the contact resistance.

The photoconductor current in the device in Fig. 1.115 is given by

$$I_{ph} = (eP_{inc}/h\nu)(2M\tau_R/\tau_{tr})[1 - \exp(-\tau_{tr}/\tau_R)] \quad (1.124)$$

where  $\tau_R$  is the recombination lifetime,  $\tau_{tr} = g/v_{tr}$  is the transit time across the gap and  $M$  is the multiplication factor of hot carriers. An equivalent circuit of the

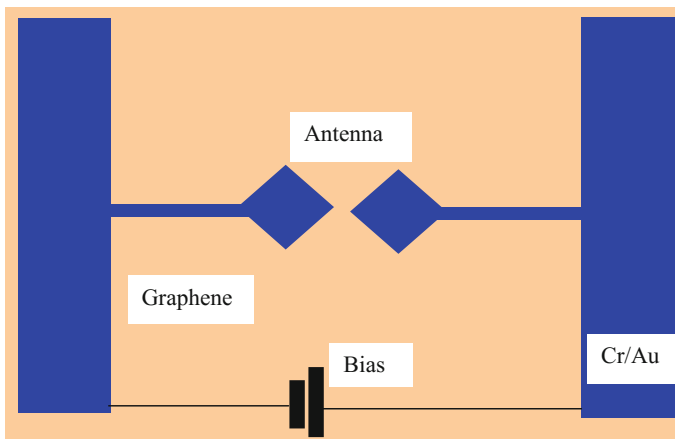


**Fig. 1.114** Graphene photodetector antenna

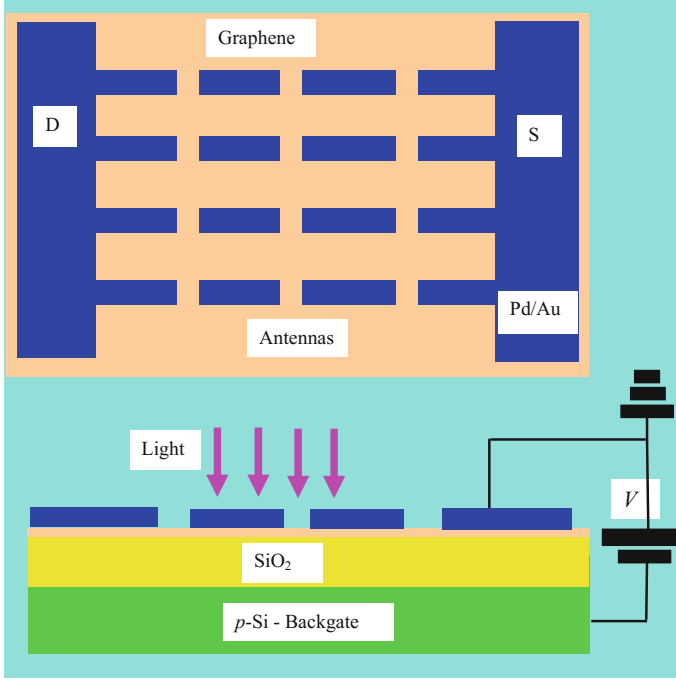


**Fig. 1.115** Mid-infrared graphene photodetector: top view (*top*) and side view (*bottom*)

photodetector is presented in Fig. 1.116. Using this circuit, the responsivity of the photodetector can be defined as

$$R = (\alpha e G / h\nu) R_G / (R_G + R_S + R_L) \quad (1.125)$$

where  $R_G$  is the resistance of graphene between electrodes,  $R_S$  is the series resistance, accounting for the contact resistance between graphene and metals,  $R_L$  is the load resistance,  $\alpha$  is the fraction of the incident light that is absorbed in graphene and

$$G = 2 M \tau_R [1 - \exp(-\tau_{tr}/\tau_R)] / \tau_{tr} \quad (1.126)$$

is the photoconductive gain. The maximum responsivity, of 0.4 V/W, is attained at a drain current of 4 mA.

Bolometric detection is another way to sense electromagnetic waves. This method requires low temperatures, below 1 K, and is targeting electromagnetic waves from THz up to IR. In principle, the bolometer absorbs one photon and detects the temperature increase. The bolometers are able to detect the power  $P$ , since their thermal conductance is given by  $G(T) = dP/dT$ . Among the different ways of readout of a graphene bolometer, we mention the measurements of Josephson noise,



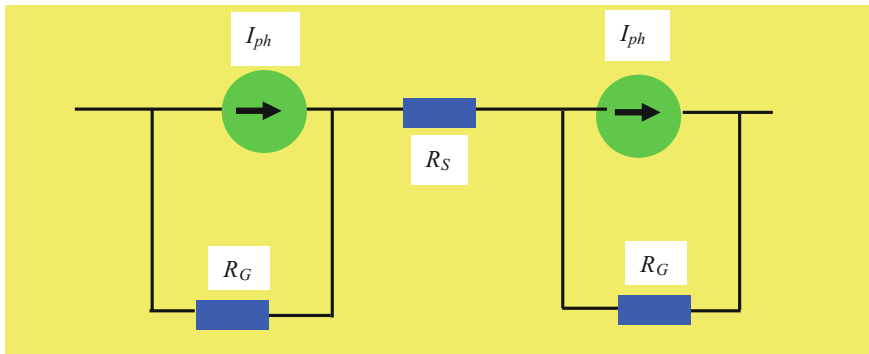


**Fig. 1.116** Equivalent circuit of the graphene antenna photodetector

superconducting critical currents, or resistance of a superconducting tunneling contact. The working principle of the graphene bolometer is depicted in Fig. 1.117.

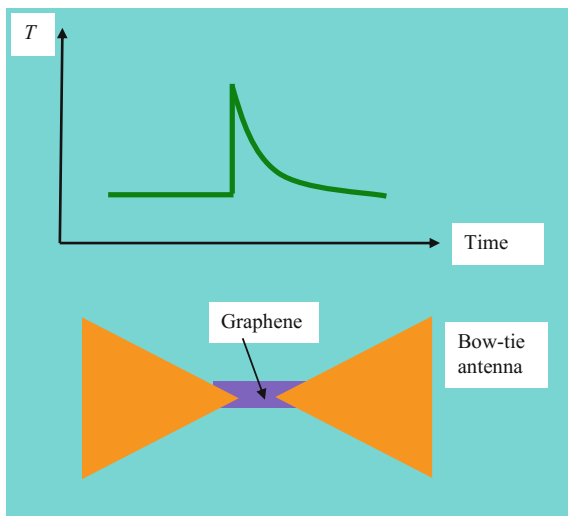
The figure of merit of a bolometric graphene detector is the energy resolving power, given by

$$R = E/\delta E \quad (1.127)$$

where  $E$  denotes the photon energy and  $\delta E$  the energy width. More details about graphene bolometers are found in Du et al. (2014).

The last issue related to graphene photonics concerns surface plasmon polaritons (SPPs) in graphene, which is a subject extensively treated in literature due to biosensing applications (Dragoman and Dragoman 2012). SPPs are collective

**Fig. 1.117** The bolometric graphene detector



electron excitations generated by an electromagnetic field, which travel along a metal-dielectric interface, are localized around nanoparticles or nanowires placed on a substrate, or pass through an array of nanoholes. Because the wavelengths of SPP waves are smaller than the free space optical wavelength, miniaturization and scalability of optical devices are possible, although little progress was done in this respect up to now. However, SPP remains one of the most sensitive sensors for many analytes.

The simplest SPP configuration is the metal-dielectric interface, represented in Fig. 1.118. The SPP oscillations are localized in the  $z$ -direction, perpendicular to the interface. SPPs are electromagnetic fields with transverse magnetic (TM) polarization propagating in the  $x$  direction with a wavevector component  $k_{SPP}$ , which exist only if

$$\varepsilon(\omega)K = -\varepsilon_r K_m \quad (1.128)$$

where  $\varepsilon(\omega)$  is the dielectric function of the metal and  $\varepsilon_r$  that of the dielectric, and  $K_m = \sqrt{k_{SPP}^2 - \varepsilon(\omega)\omega^2/c^2}$  and  $K = \sqrt{k_{SPP}^2 - \varepsilon_r\omega^2/c^2}$  are the wavevector components along  $z$  in metal and dielectric, respectively. The SPP theory and its applications are reviewed in Dragoman and Dragoman (2008b).

The advantages of SPP in graphene are that the SPP resonant frequencies, which occur generally at optical frequencies at metal/dielectric interfaces, could shift at much lower values, in the THz range, by applying gate voltages and that SPP waves in graphene display stronger electromagnetic confinement and lower dissipation losses compared to SPP waves in metallic structures. To illustrate the effect of graphene on the dispersion relation of SPPs, let's consider a thin metal slab of thickness  $d$ , in the limit  $d \rightarrow 0$ . SPP are TM waves at the metal-dielectric interfaces, but at very small metal thicknesses the SPP waves propagating at the two metal-dielectric interfaces couple, so that even and odd TM modes are produced, only the odd TM modes propagating with the dispersion relation (Jablan et al. 2013)

$$\exp(K_m d + 1) / \exp(K_m d - 1) = -\varepsilon(\omega)K / \varepsilon_r K_m \quad (1.129)$$

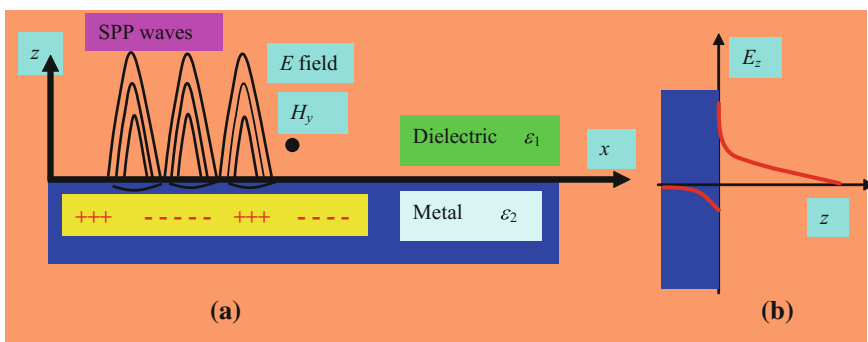


**Fig. 1.118** **a** SPP waves at the dielectric/metal interface and **b** field penetration depth in dielectric and metal

The dielectric function of the bulk metal can be expressed as  $\varepsilon(\omega) = 1 + i\sigma_v(\omega)/(\omega\varepsilon_0)$ , where  $\sigma_v(\omega)$  is the volume conductivity of the metal. In a very thin metal slab, however, the relative parameter is the surface conductivity defined as  $\sigma_s = \sigma_v d$  and, in the limit  $K_m d \ll 1$ , we obtain the dispersion relation  $K = 2i\omega\varepsilon_0\varepsilon_r/\sigma_s(\omega)$ . In graphene,  $\sigma_s(\omega)$  must be replaced by the graphene conductivity,  $\sigma_G(\omega)$ , which depends on the DC gate voltage, so that both SPP dispersion loss and resonant frequency are tunable.

If the volume conductivity is expressed by the Drude model:

$$\sigma_v = (in_v e^2/m_{eff})(\omega + i/\tau)^{-1} \quad (1.130)$$

where  $\tau$  is the relaxation time and the volume electron density  $n_v$  is related to the surface density of carries  $n_s$  as  $n_s = n_v d$ , in the limit  $\tau \rightarrow \infty$  we obtain  $\varepsilon(\omega) = 1 - \omega_p^2/\omega^2$ , with  $\omega_p = n_v e^2/\varepsilon_0 m_{eff}$  the oscillation frequency of the volume plasma. For a thin metal slab the dispersion relation in the subwavelength limit, i.e. in the approximation  $k_{SPP} \gg \omega/c$ , we obtain

$$k_{SPP} = (2m_{eff}\varepsilon_0\varepsilon_r/n_s e^2)\omega(\omega + i/\tau) \quad (1.131)$$

In the generalization of the Drude model for graphene valid for large graphene doping, which corresponds to small SPP energies, the surface conductivity becomes

$$\sigma_D(\omega) = (ie^2 v_F n_s^{1/2}/\hbar\pi^{1/2})(\omega + i/\tau)^{-1} \quad (1.132)$$

where  $n_s = \alpha V_G$ . In this case, the gate-voltage-dependent SPP dispersion relation in graphene is given by

$$k_{SPP} = (2\hbar\varepsilon_0\varepsilon_r\pi^{1/2}/v_F n_s^{1/2} e^2)\omega(\omega + i/\tau) \quad (1.133)$$

For large SPP energies, we must take into account the interband transitions, case in which

$$\sigma_I = \frac{e^2}{4\hbar} \left( \theta(\hbar\omega - 2E_F) - \frac{i}{\pi} \ln \left| \frac{2E_F + \hbar\omega}{2E_F - \hbar\omega} \right| \right) \quad (1.134)$$

and the dispersion relation depends also on the Fermi level/doping in graphene. The total graphene conductivity is  $\sigma_s = \sigma_D + \sigma_I$ .

For frequencies below  $2E_F$ ,  $\sigma_I$  is negative and there is no solution for SPP dispersion relation for TM waves. In this situation, a SPP dispersion relation for TE waves can be found as

$$K = \mu_0 \omega i \sigma_s(\omega)/2. \quad (1.135)$$

Although light-plasmon coupling is much stronger in graphene than in conventional 2D semiconductors, the excitation of SPP modes in graphene is impeded

by the mismatch between the wavenumber of free photons incident from air, where  $k_{SPP} < \omega/c$ , and SPP modes in the subwavelength region, for which  $k_{SPP} \gg \omega/c$ . A straightforward solution is to cut an array of ribbons in graphene, as suggested in Fig. 1.119. Then, plasmon waves in a ribbon with width  $W$  could be excited if their wavelength  $\lambda_{SPP} = 2\pi/k_{SPP}$  satisfies the condition (Nikitin et al. 2012):

$$W \cong m\lambda_{SPP}/2 \quad (1.136)$$

where  $m$  is an integer. Equivalently, according to (1.133) in the weak damping limit  $\tau \rightarrow \infty$ , the light will be strongly absorbed/plasmon matching occurs for resonant frequencies

$$\omega_p \propto n_s^{-1/4} W^{-1/2} \propto V_G^{-1/4} W^{-1/2}, \quad (1.137)$$

which can be tuned by applied gate voltages  $V_G$  and/or by carefully choosing  $W$ . In particular, for a periodic arrays of graphene microribbons with widths chosen in the range 1–4  $\mu\text{m}$ , and a gap:width ratio of 1, the SPP resonances are located in the THz region. For example, the SPP wavelengths can be tuned between 3 and 6 THz, as function of  $W$ , for a carrier density in graphene of  $n_s = 1.5 \times 10^{13} \text{ cm}^{-2}$ , or their

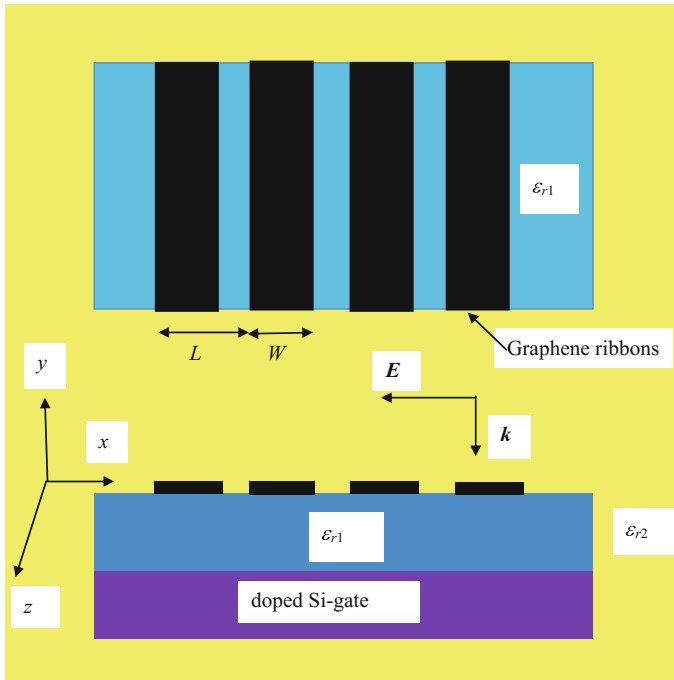


**Fig. 1.119** Periodic array of graphene ribbons for SPP generation: top view (*top*) and side view (*bottom*)

frequencies vary between 3.6 and 6 THz for  $W = 1 \text{ } \mu\text{m}$  if  $n_s$  changes between about  $1.3 \times 10^{13} \text{ cm}^{-2}$  and  $1.95 \times 10^{13} \text{ cm}^{-2}$  (Ju et al. 2011). The concentration of carriers  $n_s$  is simply modulated via gate voltages. The experimental structure needed to demonstrate the tuning of SPP frequencies via  $W$  or the carrier concentration is represented in Fig. 1.120, the top gate dielectric being ion gel.

Another way to excite SPPs is to use a silicon diffractive grating with a period  $\Lambda$  (Gao et al. 2013), as shown in Fig. 1.121. In this case, the dispersion relation can be written as

$$k_{SPP}(\omega) = \pi \hbar^2 \epsilon_0 (\epsilon_{r1} + \epsilon_{r2}) \omega^2 (1 + i/\omega\tau) / e^2 E_F \quad (1.138)$$

where  $E_F$  is the Fermi energy in graphene and  $\epsilon_{r1}$  and  $\epsilon_{r2}$  are the relative electric permittivities of the materials above and below graphene. Because the phase matching condition occurs when

$$\text{Re}(k_{SPP}(\omega)) - \omega \sin \theta / c = 2\pi / \Lambda \quad (1.139)$$

where  $\theta$  is the incidence angle of light with respect to the normal, under normal incidence, the SPP resonance frequency is given by

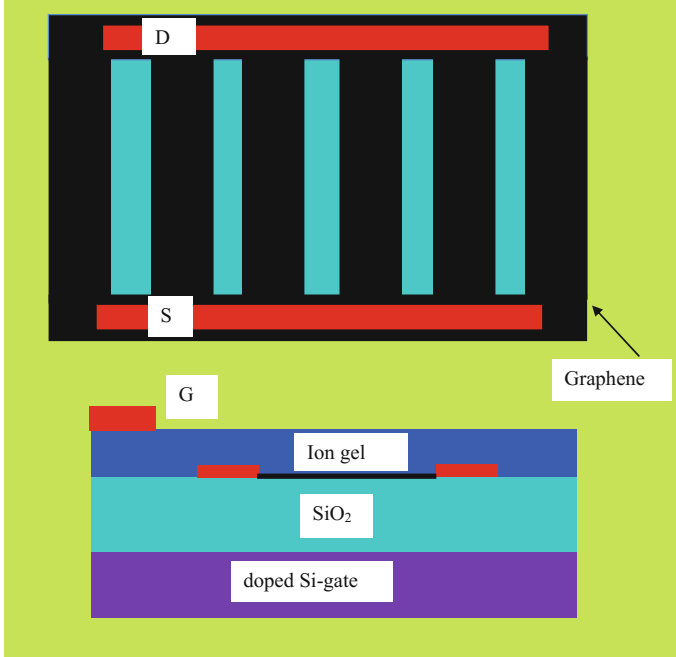


**Fig. 1.120** Graphene micro-ribbons array for tunable THz SPP generation: *top view* before ion gel deposition (*top*) and *side view* (*bottom*)

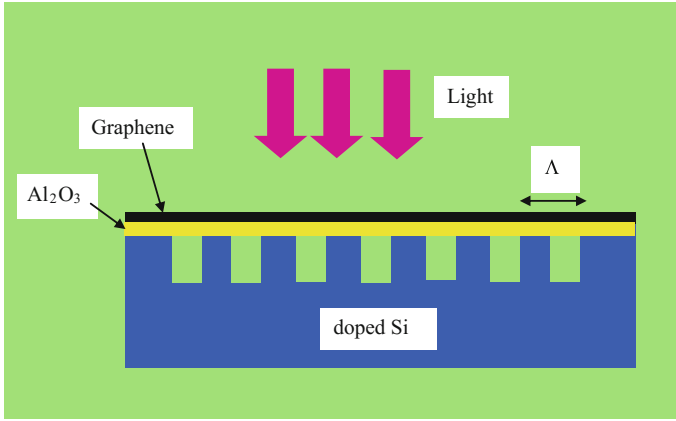


**Fig. 1.121** SPP generation in graphene using a Si grating

$$\omega_{SPP} = \sqrt{2e^2 E_F / [\hbar^2 \epsilon_0 (\epsilon_{r1} + \epsilon_{r2}) \Lambda]} \quad (1.140)$$

and can be tuned via  $\Lambda$  or  $E_F$ .

Also, a periodic structure formed from graphene nanodisks or nanorings, as depicted in Fig. 1.122 (Fang et al. 2013) is able to produce SPPs up to wavelengths of 3.7  $\mu\text{m}$ . The tuning of the SPP resonance frequency in this configuration is possible because of gate-induced electrical doping of graphene, the polarizability of graphene nanodisks of diameter  $D$  near a SPP resonance being

$$\alpha(\omega) = \frac{AD^3}{2B/(\epsilon_{r1} + \epsilon_{r2}) - i\omega D/\sigma(\omega)} \quad (1.141)$$

where  $A$  and  $B$  are constants. Formula (1.141) suggests that SPP tuning can be achieved either by modifying the nanodisks diameter, or by applying gate voltages that change the conductivity.

SPP biosensors are among the most sensitive to date. The propagation of SPPs is evidenced as a sharp minimum in the reflectivity curve as a function of the incident angle of the electromagnetic excitation of the periodic graphene geometry able to support plasmonics waves. As illustrated in Fig. 1.123, the reflectivity curve dependence on the incidence angle,  $R = f(\varphi)$  has a unique imprint—a resonant behaviour indicating SPP launching. This resonance angle is called SPP resonance.

The reflectivity change at the SPP resonance is one of the most common concept for label-free sensing in biomedical sciences (Englebienne et al. 2003). Free-label biosensing is based on the shift of the reflectivity minimum at SPP resonance when an additional molecular layer is deposited on graphene. This change in reflectivity is extremely sensitive to additional molecules deposited on graphene, making SPP

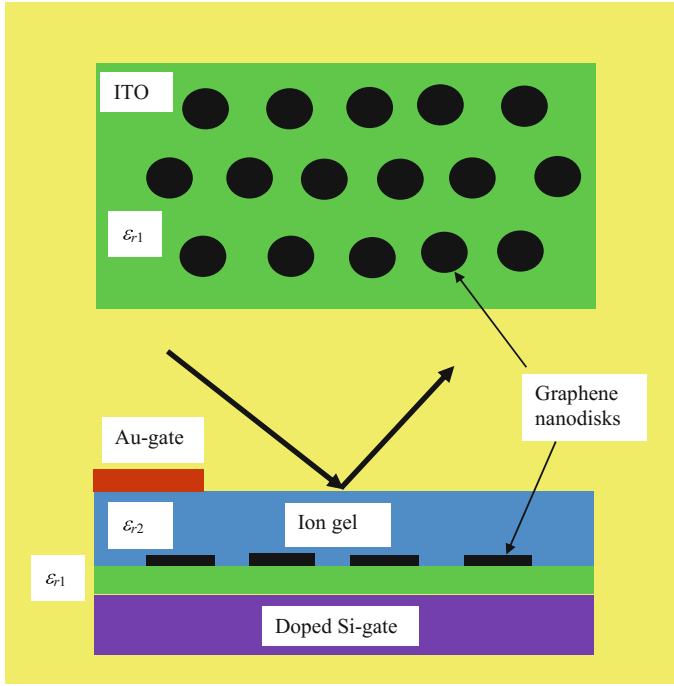


**Fig. 1.122** SPP generation using a periodic graphene nanodisk array: *top view* before ion gel deposition (*top*) and side view (*bottom*)

resonance monitoring one of the most advanced methods to measure, for example, DNA hybridization.

The configuration of a label-free SPP biosensor is represented in Fig. 1.124. As the thickness of the sensing layer (graphene+biomolecules) increases because biomolecules are deposited on graphene, the incident angle of the optical excitation in the prism,  $\varphi_0$ , for which the reflectivity is minimum is modified by even few molecules.

The simple model of a three-layer (prism, metal+graphene sensing layer) sensing configuration can provide a quantitative description of the label-free SPP sensor. More precisely, variations in the SPP resonance angle are given by

$$\Delta\varphi = \alpha_1 \Delta n + \alpha_2 \Delta t \quad (1.142)$$

where  $\alpha_1$  and  $\alpha_2$  are constants and  $\Delta t$  represents the change in the thickness of the protein layer. The corresponding variation of the index of refraction is

$$\Delta n = -\frac{(n^2 + 2)^2}{6n} \frac{\Delta t}{t} \left( \frac{n^2 - 1}{n^2 + 2} - \frac{n_w^2 - 1}{n_w^2 + 2} \frac{V}{V_{tot}} \right) \quad (1.143)$$

**Fig. 1.123** The plasmonic resonance

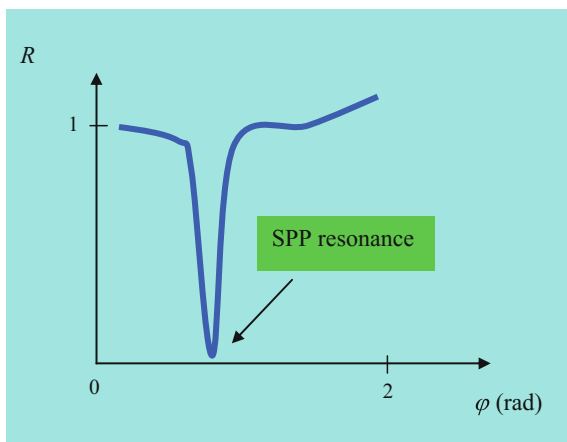
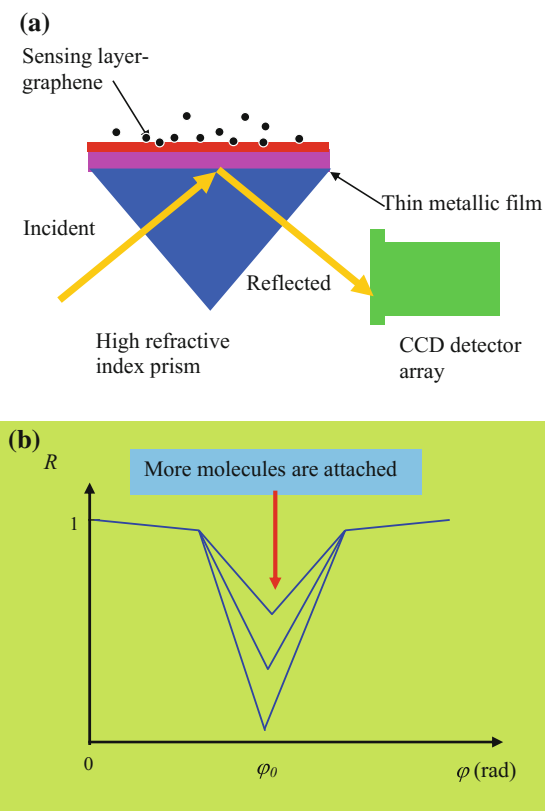


**Fig. 1.124** Principle of a SPP label-free biosensor: **a** measuring geometry, and **b** SPP resonance shift with attached molecules





where  $n$  is the refractive index of the biomolecule with volume  $V$  and  $n_w$  is the refractive index of water, with volume  $V_w$  such that  $V_{tot} = V + V_w$ .

The changes of the SPP resonance angle are measured in resonance units (RU).  $10^3$  RU represents a modification with  $0.1^\circ$  of the SPP resonance angle due to biomolecules with a distributed mass of  $1 \text{ ng/cm}^2$ .

The sensitivity of SPP sensors is defined as the first derivative of the parameter (angle, wavelength) with respect to the parameter to be measured (refractive index, thickness, concentration, etc.). The sensitivity is measured in RIU (refractive index unit). The typical RIU is of the order  $10^{-8}$ .

The SPP chip is in fact a gold film on glass or other dielectrics. In the case of SPP on graphene, the graphene monolayer acts as cover layer for the gold film. A graphene SPP biosensor having  $N$  graphene layers is  $g$  times more sensitive than SPP biosensors containing thin gold films (Wu et al. 2010a), where

$$g = (1 + 0.025 N) \times \gamma \quad (1.144)$$

and  $\gamma > 1$ . The enhanced sensitivity is due to the optical properties of graphene and the increased adsorption of biomolecules. For  $N = 10$ ,  $\gamma = 4$  and the sensitivity increases with 25%.

The simplest method to produce a graphene SPP sensor on the graphene-metal surface is illustrated in Fig. 1.125. This graphene SPP chip obtained via transfer printing has many applications (Salihoglu et al. 2012). For instance, such graphene SPP chips are able to detect DNA hybridization with attomolar concentration (Zagorodko et al. 2014). The conventional SPP instrumentation with nanomolar sensitivity is not sensitive enough to detect cancer markers or gene expressions, which require femto to attomolar level to detect DNA. To achieve such impressive sensitivities for DNA hybridization event detection, graphene, located on top of the SPP chip, must be noncovalently functionalized with gold nanostars carrying single stranded DNA. In this way, the SPP sensor attains a sensitivity of 500 aM for complementary DNA. The detection principle of DNA hybridization, shown in Fig. 1.126, is based on the significant change in the SPP resonance signal in the visible spectrum between non-hybridized and hybridized states of DNA.

Mid infrared is a special spectral region for biosensing because strong molecular vibrations of biomolecules (DNA, proteins, lipids) occur in this range. If this physical property is combined with the fact that SPPs in IR in graphene undergo an unprecedented spatial confinement, the result is a high sensitive SPP biosensor (Rodrigo et al. 2015). The biosensor consists of a graphene nanoribbon array (see Fig. 1.127) with  $W = 30 \text{ nm}$  and  $\Lambda = 80 \text{ nm}$ , placed on a Si/SiO<sub>2</sub> substrate, where the Si substrate is doped and serves as backgate. By changing the gate voltage between 0 and  $-100 \text{ V}$ , the resonance frequency of the sensor changes from  $1450$  to about  $1800 \text{ cm}^{-1}$ . The functionality of this sensor is demonstrated by the detection of protein A/G, which binds to a goat anti-mouse IgG antibody to form a protein

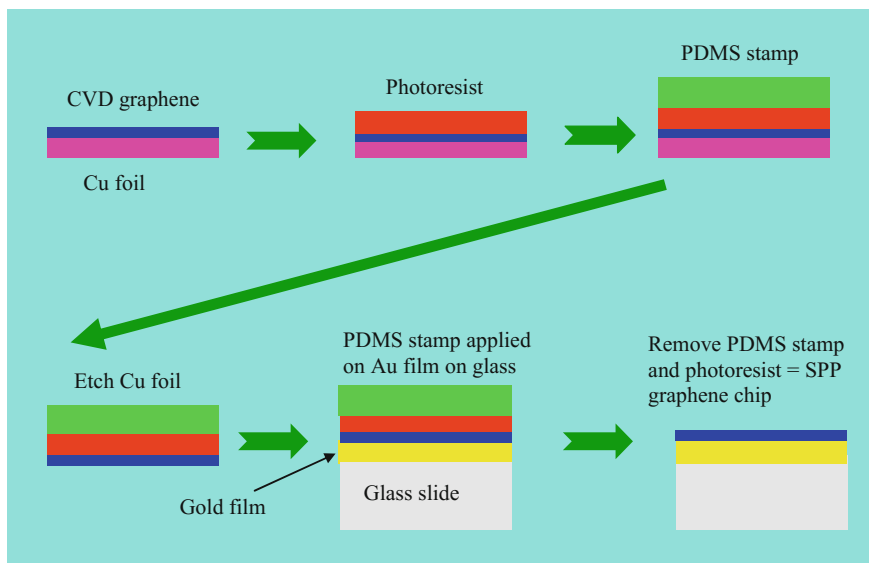


**Fig. 1.125** SPP graphene chip fabrication

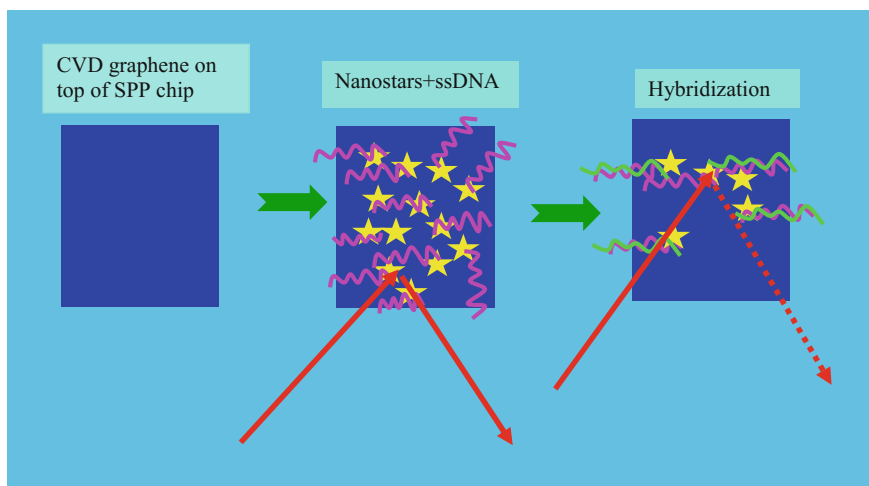


**Fig. 1.126** Principle of DNA hybridization detection using a graphene chip

bilayer. The resonance shift produced by the resulting bilayer, which has a thickness of 8 nm, is  $160\text{ cm}^{-1}$  in a graphene-based sensor, compared to  $27\text{ cm}^{-1}$  when gold is used instead. From such measurements it is possible to extract the index of refraction of the protein in mid-IR.

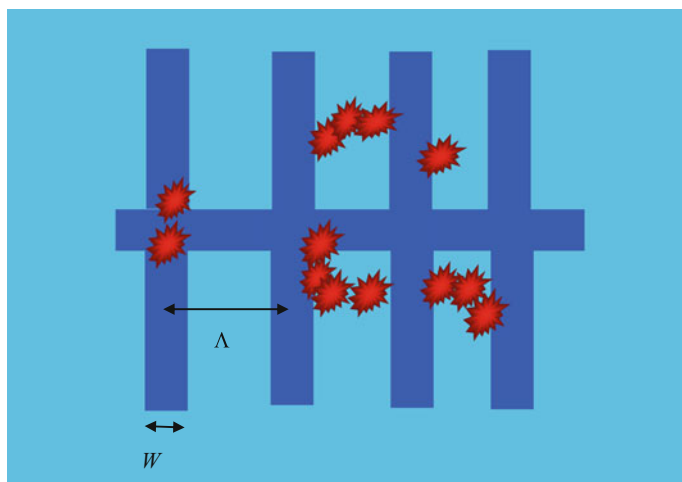


**Fig. 1.127** Graphene nanoribbon array as mid IR biosensor

## References

- Bae S-H, Lee Y, Sharma BK, Lee HJ, Kim JH, Ahn J-H (2013) Graphene-based transparent strain sensor. *Carbon* 51:236–242
- Balandin AA (2011) Thermal properties of graphene and nanostructured carbon materials. *Nat Mater* 10:569–581
- Balocco C, Halsall M, Vinh NQ, Song AM (2008) THz operation of asymmetric-nanochannels devices. *J Phys: Cond Matt* 20:384203
- Bao Q, Loh KP (2012) Graphene photonics, plasmonics, and broadband optoelectronic devices. *ACS Nano* 6:3677–3694
- Baringhaus J, Ruan M, Edler F, Tejeda A, Sicot M, Taleb-Ibrahimi A, Li A-P, Jiang Z, Conrad EH, Berger C, Tegenkamp C, de Heer WA (2014) Exceptional ballistic transport in epitaxial graphene nanoribbons. *Nature* 506:349–354
- Bekyarova E, Itkis ME, Ramesh P, Berger C, Spinkle M, de Heer WA, Hanaddon RC (2009) Chemical modification of epitaxial graphene: spontaneous grafting of aryl groups. *J Am Chem Soc* 131:1336–1337
- Boland CS, Khan U, Backes C, O'Neill A, McCauley J, Duane S, Shanker R, Liu Y, Jurewicz I, Dalton AB, Coleman JN (2014) Sensitive, high-strain, high-rate bodily motion sensors based on graphene-rubber composites. *ACS Nano* 8:8819–8830
- Bonaccorso F, Sun Z, Hasan T, Ferrari AC (2010) Graphene photonics and optoelectronics. *Nat Photonics* 4:611–622
- Britnell L, Gorbachev RV, Jalil R, Belle BD, Schedin F, Mishchenko A, Georgiou T, Katsnelson MI, Eaves L, Morozov SV, Peres NMR, Leist J, Geim AK, Novoselov KS, Ponomarenko LA (2012) Field-effect tunneling transistor based on vertical graphene heterostructures. *Science* 335:947–950
- Britnell L, Gorbachev RV, Geim AK, Ponomarenko LA, Mishchenko A, Greenaway MT, Fromhold TM, Novoselov KS, Eaves L (2013) Resonant tunneling and negative differential conductance in graphene transistors. *Nature Commun* 4:1794
- Bolotin KI, Sikes KJ, Jiang Z, Klima M, Fudenberg G, Hone J, Kim P, Stormer HL (2008) Ultrahigh electron mobility in suspended graphene. *Solid State Commun* 146:351–355

- Bruna M, Borini S (2009) Optical constants of graphene layers in the visible range. *Appl Phys Lett* 94:031901
- Cai X, Sushkov AB, Suess RJ, Jadidi MM, Jenkins GJ, Nyakiti LO, Myers-Ward RL, Li S, Yan J, Gaskill DK, Murphy TE, Drew HD, Fuhrer MS (2014) Sensitive room-temperature terahertz detection via the photothermoelectric effect in graphene. *Nat Nanotechnol* 9:814–819
- Castro Neto AH, Guinea F, Peres NMR, Novoselov KS, Geim AK (2009) The electronic properties of graphene. *Rev Mod Phys* 81:109–162
- Cavallo F, Delgado RR, Kelly MM, Sánchez Pérez JR, Schroeder DP, Xing HG, Eriksson MA, Lagally MG (2014) Exceptional charge transport properties of graphene on germanium. *ACS Nano* 8:10237–10245
- Chakraborty C, Beams R, Goodfellow KM, Wicks GM, Novotny L, Vamivakas AN (2014) Optical antenna enhanced graphene photodetector. *Appl Phys Lett* 105:241114
- Chen C-C, Aykol M, Chang C-C, Levi AFJ, Cronin SB (2011a) Graphene-silicon Schottky diodes. *Nano Lett* 11:1863–1867
- Chen C-F, Park C-H, Boudouris BW, Horng J, Geng B, Girit C, Zettl A, Crommie MF, Segalman RA, Louie SG, Wang F (2011b) Controlling inelastic light scattering quantum pathways in graphene. *Nature* 471:617–620
- Cheng R, Bai J, Liao L, Zhou H, Chen Y, Liu L, Lin Y-C, Jiang S, Huang Y, Duan X (2012) High-frequency self-aligned graphene transistors with transferred gate stacks. *Proc Nat Acad Sci* 109:11588–11592
- Deligeorgis G, Dragoman M, Neculoiu D, Dragoman D, Konstantinidis G, Cismaru A, Plana R (2010) Microwave switching of graphene field effect transistor at and far from the Dirac point. *Appl Phys Lett* 96:103105
- Dong X, Shi Y, Huang W, Chen P, Li L-J (2010) Electrical detection of DNA hybridization with single-base specificity using transistors based on CVD-grown graphene sheets. *Adv Mater* 22:1–5
- Dragoman D, Dragoman M (2007a) Negative differential resistance of electrons in graphene barrier. *Appl Phys Lett* 90:143111
- Dragoman D, Dragoman M (2007b) Giant thermoelectric effect in graphene. *Appl Phys Lett* 91:203116
- Dragoman D, Dragoman M (2008a) Terahertz Bloch oscillations in periodic graphene structures. *Appl Phys Lett* 93:103105
- Dragoman M, Dragoman D (2008b) Plasmonics: Applications to nanoscale terahertz and optical devices. *Prog Quantum Electron* 32:1–41
- Dragoman D (2009) Evidence against Klein paradox in graphene. *Phys Scr* 79:015003
- Dragoman M, Dragoman D (2009) Graphene-based quantum electronics. *Prog. Quantum Electron* 33:165–214
- Dragoman D (2010) Low-energy conductivity of single- and double-layer graphene from the uncertainty principle. *Phys Scr* 81:035702
- Dragoman D, Dragoman M, Plana R (2010) Graphene-based ultrafast diode. *Appl Phys Lett* 108:084316
- Dragoman D, Dragoman M (2012) *Bionanoelectronics*. Springer, Heidelberg
- Dragoman M, Konstantinidis G, Tsagaraki K, Kostopoulos T, Dragoman D, Neculoiu D (2012a) Graphene-like metal-on-silicon field-effect transistor. *Nanotechnology* 23:305201
- Dragoman M, Neculoiu D, Cismaru A, Deligeorgis G, Konstantinidis G, Dragoman D (2012b) Graphene radio: Detecting radiowaves with a single atom sheet. *Appl Phys Lett* 109:033109
- Dragoman D, Dragoman M (2013) Geometrically induced rectification in two-dimensional ballistic nanodevices. *J Phys D* 46:055306
- Dragoman D, Dragoman M (2014) Transport properties of carbon nanotubes and graphene. In: Tanaka K, Iijima S (eds) *Carbon nanotubes and graphene*, 2nd Edn. Elsevier, pp 151–164
- Dragoman M, Dinescu A, Dragoman D (2014a) Negative differential resistance in graphene-based ballistic field-effect transistor with oblique top gate. *Nanotechnology* 25:41520
- Dragoman M, Aldrigo M, Dinescu A, Dragoman D, Costanzo A (2014b) Towards a terahertz direct receiver based on graphene up to 10 THz. *J Appl Phys* 115:044307

- Du X, Skachko I, Barker A, Andrei EY (2008) Approaching ballistic transport in suspended graphene. *Nat Nanotechnol* 3:491–495
- Du X, Prober DE, Vora H, McKitterick CB (2014) Graphene-based bolometers. *Graphene 2D Mater* 1:1–22
- Englebienne P, Van Hoonacker A, Verhas M (2003) Surface plasmon resonance: principles, methods and applications in biomedical sciences. *Spectroscopy* 17:255–273
- Fang T, Konar A, Xing H, Jena D (2007) Carrier statistics and quantum capacitance of graphene sheets and ribbons. *Appl Phys Lett* 91:092109
- Fang Z, Thongrattanasiri S, Schlather A, Liu Z, Ma L, Wang Y, Ajayan PM, Nordlander P, Halas NJ, García de Abajo FJ (2013) Gated tunability and hybridization of localized plasmons in nanostructured graphene. *ACS Nano* 7:2388–2395
- Fu X-W, Liao Z-M, Zhou J-X, Zhou Y-B, Wu H-C, Zhang R, Jing G, Xu J, Wu X, Guo W, Yu D (2011) Strain dependent resistance in chemical vapor deposition grown graphene. *Appl Phys Lett* 99:213107
- Gao W, Shi G, Jin Z, Shu J, Zhang Q, Vajtai R, Ajayan PM, Kono J, Xu Q (2013) Excitation and active control of propagating surface plasmon polaritons in graphene. *Nano Lett* 13:3698–3702
- Geim AK (2011) Nobel lecture: Random walk to graphene. *Rev Mod Phys* 83:851–862
- Geim AK (2012) Graphene prehistory. *Phys Scr T146*:014003
- Georgakilas V, Otyepka M, Bourlinos AB, Chandra V, Kim N, Kemp KC, Hobza P, Zboril R, Kim KS (2012) Functionalization of graphene: covalent and non-covalent approaches, derivatives and applications. *Chem Rev* 112:6156–6214
- Green NS, Norton ML (2015) Interactions of DNA with graphene and sensing applications of graphene field-effect transistor devices: a review. *Anal Chimica Acta* 853:127–142
- Guo Z, Dong R, Chakraborty PS, Lourenco N, Palmer J, Hu Y, Ruan M, Hankinson J, Kunc J, Cressler JD, Berger C, de Heer WA (2013) Record maximum oscillation frequency in C-face epitaxial graphene transistors. *Nano Lett* 13:942–947
- Hähnlein B, Händel B, Pezoldt J, Töpfer H, Granzner R, Schwierz F (2012) Side-gate graphene field-effect transistors with high transconductance. *Appl Phys Lett* 101:093504
- Han MY, Özyilmaz B, Zhang Y, Kim P (2007) Energy band-gap engineering of graphene nanoribbons. *Phys Rev Lett* 98:206805
- Han S-J, Oida S, Jenkins KA, Lu D, Zhu Y (2013) Multifinger embedded T-shaped gate graphene RF transistors with high  $f_{\max}/f_T$  ratio. *IEEE Electron Dev Lett* 34:1340–1342
- Han S-J, Valdes Garcia A, Oida S, Jenkins KA, Haensch W (2014) Graphene radio frequency receiver integrated circuit. *Nat Commun* 5:3086
- Hanson GW (2008) Dyadic Green's functions and guided surface waves for a surface conductivity model of graphene. *J Appl Phys* 103:064302
- Hill EW, Vijayaraghavan A, Novoselov K (2011) Graphene sensors. *IEEE Sens J* 11:3161–3170
- Hou C, Wang H, Zhang Q, Li Y, Zhu M (2014) Highly conductive, flexible, and compressible all-graphene passive electronic skin for sensing human touch. *Adv Materials* 26:5018–5024
- Hu YT, Pantouvaki M, Brems S, Asselberghs I, Huyghebaert C, Geisler M, Alessandri C, Baets R, Absil P, Van Thourhout D, Van Campenhout J (2014) Broadband 10 Gb/s graphene electro-absorption modulator on silicon for chip-level optical interconnects. *IEEE Electron Devices Meet (IEDM)*, 15–17 Dec 2014:5.6.1–5.6.4
- Huang B-C, Zhang M, Wang Y, Woo J (2011a) Contact resistance in top-gated graphene field-effect transistors. *Appl Phys Lett* 99:032107
- Huang M, Pascal TA, Kim H, Goddard III WA, Greer JR (2011b) Electronic-mechanical coupling in graphene from in situ nanoindentation experiments and multiscale atomistic simulations. *Nano Lett*:1241–1246
- Jablan M, Soljačić M, Buljan H (2013) Plasmons in graphene: fundamental properties and potential applications. *Proc IEEE* 101:1689–1704
- Ju L, Geng B, Horng J, Girit C, Martin M, Hao Z, Bechtel HA, Liang X, Zettl A, Shen YR, Wang F (2011) Graphene plasmonics for tunable terahertz metamaterials. *Nat Nanotechnol* 6:630–634

- Jung M-H, Park G-H, Yoshida T, Fukidome H, Suemitsu T, Otsuji T, Suemitsu M (2013) High-performance graphene field-effect transistor with extremely small access length using self-aligned source and drain technique. *Proc IEEE* 101:1603–1608
- Jurewicz I, Fahimi A, Lyons PE, Smith RJ, Cann M, Large ML, Tian M, Coleman JN, Dalton AB (2014) Insulator-conductor type transitions in graphene-modified silver nanowire networks: a route to inexpensive transparent conductors. *Adv Funct Mat* 24:7580–7587
- Katsnelson MI (2012) Graphene. *Carbon in Two-Dimensions*. Cambridge University Press, Cambridge, UK:pp. 7–10
- Katsnelson MI, Novoselov KS, Geim AK (2006) Chiral tunneling and the Klein paradox in graphene. *Nat Phys* 2:620–625
- Kim KS, Zhao Y, Jang H, Lee SY, Kim JM, Kim KS, Ahn J-H, Kim P, Choi J-Y, Hong BH (2009) Large-scale pattern growth of graphene films for stretchable transparent electrodes. *Nature* 457:706–710
- Kim BJ, Jang H, Lee S-K, Hong BH, Ahn J-H, Cho JH (2010) High-performance flexible graphene field effect transistors with ion gel gate dielectrics. *Nano Lett* 10:3464–3466
- Kim D, Lee D, Lee Y, Jeon DY (2013a) Work-function engineering of graphene anode by bis (trifluoromethanesulphonyl)amide doping for efficient polymer light-emitting diodes. *Adv Funct Mater* 23:5049–5055
- Kim H-Y, Lee K, McEvoy N, Yim C, Duesberg GS (2013b) Chemically modulated graphene diodes. *Nano Lett* 13:2182–2188
- Kim U, Kang J, Lee C, Kwon HY, Hwang S, Moon H, Koo JC, Nam J-D, Hong BH, Choi J-B, Choi HR (2013c) A transparent and stretchable graphene-based actuator for tactile display. *Nanotechnology* 24:145501
- Koenig SP, Doganov RA, Schmidt H, Castro Neto AH, Özyilmaz B (2014) Electric field effect in ultrathin black phosphorous. *Appl Phys Lett* 104:103106
- Koppens FHL, Mueller T, Avouris Ph, Ferrari AC, Vitiello MS, Polini M (2014) Photodetectors based on graphene, other two-dimensional materials, and hybrid systems. *Nat Nanotechnol* 9:780–793
- Kuila T, Bose S, Khanra P, Mishra AK, Kim NH, Lee JH (2011) Recent advances in graphene-based biosensors. *Biosens Bioelectron* 26:4637–4648
- Kulkarni GS, Reddy K, Zhang Z, Fan X (2014) Graphene nanoelectronic heterodyne sensor for rapid and sensitive vapour detection. *Nat Commun* 5:4376
- Kumar M, Bhaskaran H (2015) Ultrasensitive room-temperature piezoresistive transduction in graphene-based nanoelectromechanical systems. *Nano Lett* 15:2562–2567
- Kumar S, Ahlawat W, Kumar R, Dilbaghi N (2015) Graphene, carbon nanotubes, zinc oxide and gold as elite nanomaterials for fabrication of biosensors for healthcare. *Biosens Bioelectron* 70:498–503
- Kunc J, Hu Y, Palmer J, Guo Z, Hankinson J, Gamal SH, Berger C, de Heer WA (2014) Planar edge Schottky barrier-tunneling transistors using epitaxial graphene/SiC junctions. *Nano Lett* 14:5170–5175
- Lee C, Wei X, Kysar JW, Hone J (2008) Measurement of the elastic properties and intrinsic strength of monolayer graphene. *Science* 321:385–388
- Lee J, Ha T-J, Li H, Parrish KN, Holt M, Dodabalapur A, Ruoff RS, Akinwande D (2013) 25 GHz embedded-gate graphene transistors with high-k dielectrics on extremely flexible plastic sheets. *ACS Nano* 7:7744–7750
- Lee J-H, Loya PE, Lou J, Thomas EL (2014) Dynamic mechanical behavior of multilayer graphene via supersonic projectile penetration. *Science* 346:1092–1096
- Leong WS, Nai CT, Thong JTL (2014) What does annealing do to metal-graphene contacts? *Nano Lett* 14:3840–3847
- Li J, Niu L, Zheng Z, Yan F (2014) Photosensitive graphene transistors. *Adv Mater* 26:5239–5273
- Liao L, Bai J, Cheng R, Liu Y-C, Jiang S, Qu Y, Huang Y, Duang X (2010) Sub-100 nm channel length graphene transistors. *Nano Lett* 10:3952–3956
- Liu M, Yin X, Ulin-Avila E, Geng B, Zentgraf T, Ju L, Wang F, Zhang X (2011) A graphene-based broadband optical modulator. *Nature* 474:64–67

- Liu M, Yin X, Zhang X (2012) Double-layer graphene optical modulator. *Nano Lett* 12:1482–1485
- Liu G, Ahsan S, Khitun AG, Lake RK, Balandin A (2013) Graphene-based non-Boolean logic circuits. *J Appl Phys* 114:154310
- Liu J, Liu Z, Barrow CJ, Yang W (2015a) Molecularly engineered graphene surfaces for sensing applications: a review. *Anal Chim Acta* 859:1–19
- Liu X, Sun J, Zhang X (2015b) Novel 3D graphene aerogel-ZnO composites as efficient detection for NO<sub>2</sub> at room temperature. *Sens Actuators B* 211:220–226
- Low T, Avouris Ph (2014) Graphene plasmonics for terahertz to mid-infrared applications. *ACS Nano* 8:1086–1101
- Lu C-C, Lin Y-C, Yeh C-H, Huang J-C, Chiu P-W (2012) High mobility flexible graphene field-effect transistors with self-healing gate dielectrics. *ACS Nano* 6:4469–4474
- Luo S, Wang Y, Tong X, Wang Z (2015) Graphene-based optical modulators. *Nanoscale Res Lett* 10:199
- Mayorov AS, Gorbachev RV, Morozov SV, Britnell L, Jalil R, Ponomarenko LA, Blake P, Novoselov KS, Watanabe K, Taniguchi T, Geim AK (2011) Micrometer-scale ballistic transport in encapsulated graphene at room temperature. *Nano Lett* 11:2396–2399
- Mehr W, Dabrowski J, Scheytt JC, Lippert G, Xie Y-H, Lemme MC, Ostling M, Lupina G (2012) Vertical graphene base transistor. *IEEE Electron Dev Lett* 33:691–693
- Merchant CA, Healy K, Wanunu M, Ray V, Peterman N, Bartel J, Fischbein MD, Venta K, Luo Z, Johnson ATC, Drndić M (2010) DNA translocation through graphene nanopores. *Nano Lett* 10:2915–2921
- Miao X, Tongay S, Petterson MK, Berke K, Rinzler AG, Appleton BR, Hebard AF (2012) High efficiency graphene solar cells by chemical doping. *Nano Lett* 12:2745–2750
- Mittendorff M, Winnerl S, Kamann J, Eröms J, Weiss D, Schneider H, Helm M (2013) Ultrafast graphene-based broadband THz detector. *Appl Phys Lett* 103:021113
- Novoselov KS, Geim AK, Morozov SV, Jiang D, Zhang Y, Dubonos SV, Grigorieva IV, Firsov AA (2004) Electric field effect in atomically thin carbon films. *Science* 306:666–669
- Novoselov KS, Geim AK, Morozov SV, Jiang D, Katsnelson MI, Grigorieva IV, Dubonos SV, Firsov AA (2005) Two-dimensional gas of massless Dirac fermions in graphene. *Nature* 438:197–200
- Nikitin AY, Guinea F, Garcia-Vidal FJ, Martin-Moreno L (2012) Surface-plasmon enhanced absorption and suppressed transmission in periodic arrays of graphene ribbons. *Phys Rev Lett B* 85:081405
- Park SJ, Kwon OS, Lee SH, Song HS, Park TH, Jang J (2012) Ultrasensitive flexible graphene based field-effect transistor (FET)-type bioelectronic nose. *Nano Lett* 12:5082–5090
- Park JJ, Hyun WJ, Mun SC, Park YT, Park OO (2015) Highly stretchable and wearable graphene strain sensors with controllable sensitivity for human motion monitoring. *ACS Appl Mater Interfaces* 7:6317–6324
- Parrish KN, Akinwande D (2012) An exact solvable model for the graphene transistor in the quantum capacitance limit. *Appl Phys Lett* 101:053501
- Petrone N, Meric I, Hone J, Shepard KL (2012) Graphene field-effect transistors with gigahertz-frequency power gain on flexible substrates. *Nano Lett* 12:121–125
- Phare CT, Lee Y-HD, Cardenas J, Lipson M (2015) Graphene electro-optic modulator with 30 GHz bandwidth. *Nat Photonics* 9:511–515
- Ponomarenko LA, Belle BD, Jalil R, Britnell L, Gorbachev RV, Geim AK, Novoselov KS, Castro Neto AH, Eaves L, Katsnelson MI (2013) Field-effect control of tunneling barrier height by exploiting graphene's low density of states. *J Appl Phys* 113:136502
- Prezioso S, Perrozzi F, Giancaterini L, Cantalini C, Treossi E, Palermo V, Nardone M, Santucci S, Ottaviano L (2013) Graphene oxide as a practical solution to high sensitivity gas sensing. *J Phys Chem C* 117:10683–10690
- Radoi A, Iordanescu A, Cismaru A, Dragoman M, Dragoman D (2010) Ultrabroadband photodetection based on graphene ink. *Nanotechnology* 21:455202

- Reddy D, Register LF, Carpenter GD, Banerjee SK (2011) Graphene field-effect transistors. *J Phys D* 44:313001
- Rodrigo D, Limaj O, Janner D, Etezadi D, Garcia de Abajo FJ, Pruneri V, Altug H (2015) Mid-infrared plasmonic biosensing with graphene. *Science* 349:165–169
- Sabri SS, Levesque LP, Aguirre CM, Guillemette J, Martel R, Szkopek T (2009) Graphene field transistor with parylene gate dielectric. *Appl Phys Lett* 95:242104
- Salihoglu O, Balci S, Kocabas C (2012) Plasmon-polaritons on graphene-metal surface and their use in biosensors. *Appl Phys Lett* 100:213110
- Schedin F, Geim AK, Morozov SM, Hill EW, Blake P, Katsnelson MI, Novoselov KS (2007) Detection of individual gas molecules adsorbed on graphene. *Nat Mater* 6:652–655
- Schneider GF, Kowalczyk SW, Calado VE, Pandraud G, Zandbergen HW, Vandersypen LMK, Dekker C (2010) DNA translocation through nanopores. *Nano Lett* 10:3163–3167
- Schwierz F (2013) Graphene transistors: status, prospects, and problems. *Proc IEEE* 101:1567–1584
- Sensale-Rodríguez B, Yan R, Rafique S, Zhu M, Li W, Liang X, Gundlach D, Protasenko V, Kelly MM, Jena D, Liu L, Xing HG (2012) Extraordinary control of terahertz beam reflectance in graphene electro-absorption modulators. *Nano Lett* 12:4518–4522
- Sensale-Rodríguez B, Yan R, Liu L, Jena D, Xiang HG (2013) Graphene for reconfigurable terahertz optoelectronics. *Proc IEEE* 101:1705–1716
- Sevinçli H, Cuniberti G (2010) Enhanced thermoelectric figure of merit in edge disordered zigzag graphene nanoribbons. *Phys Rev B* 81:113401
- Sharma BK, Ahn J-H (2013) Graphene based field effect transistors: efforts made towards flexible electronics. *Solid State Electron* 89:177–188
- Sharma P, Bernard LS, Bazigos A, Magrez A, Ionescu AM (2015) Room-temperature negative differential resistance in graphene field effect transistors: Experiments and theory. *ACS Nano* 15:620–625
- Sinha D, Lee JU (2014) Ideal graphene/silicon Schottky junction diodes. *Nano Lett* 14:4660–4664
- Smith AD, Niklaus F, Paussa A, Vaziri S, Fischer AC, Sterner M, Forsberg F, Delin A, Esseni D, Palestri P, Östling M, Lemme MC (2013) Electromechanical piezoresistive sensing in suspended graphene membranes. *Nano Lett* 13:3237–3242
- Song AM, Missous M, Omrling P, Peaker AR, Samuelson L, Seifert W (2003) Unidirectional electron flow in a nanometer-scale semiconductor channel: a self-switching device. *Appl Phys Lett* 83:1881–1883
- Stander N, Huard B, Goldhaber-Gordon D (2009) Evidence for Klein tunneling in graphene *p-n* junctions. *Phys Rev Lett* 102:026807
- Sun Q, Kim DH, Park SS, Lee NY, Zhang Y, Lee JH, Cho K, Cho JH (2014) Transparent, low-power pressure sensor matrix based on coplanar-gate graphene transistors. *Adv Mater* 26:4735–4740
- Sun Z, Chang H (2014) Graphene and graphene-like two-dimensional materials in photodetection: mechanisms and methodology. *ACS Nano* 8:4133–4156
- Sutar S, Comfort ES, Liu J, Taniguchi T, Watanabe K, Lee JU (2012) Angle- dependent carrier transmission in graphene *p-n* junctions. *Nano Lett* 12:4460–4464
- Tan Y-W, Zhang Y, Bolotin K, Zhao Y, Adam S, Hwang EH, Das Sarma S, Stormer HL, Kim P (2006) Measurement of scattering rate and minimum conductivity in graphene. *Phys Rev Lett* 99:246803
- Thiele SA, Schaefer JA, Schwierz F (2010) Modeling of graphene metal-oxide-semiconductor field-effect transistors with gapless large-area graphene channels. *J Appl Phys* 107:094505
- Tian H, Li C, Mohammad MA, Cui Y-L, Mi W-T, Yang Y, Xie D, Ren T-L (2014) Graphene earphones: entertainment for both humans and animals. *ACS Nano* 8:5883–5890
- Tian H, Shu Y, Wang X-F, Mohammad MA, Bie Z, Xie Q-Y, Li C, Mi W-T, Yang Y, Ren T-L (2015) A graphene-based resistive pressure sensor with record-high sensitivity in a wide pressure range. *Sci Rep* 5:8603
- Tongay S, Lamaitre M, Schumann T, Berke K, Appleton BR, Gila B, Hebard AF (2011) Graphene/GaN Schottky diodes: stability at elevated temperatures. *Appl Phys Lett* 99:102102



- Tongay S, Lemaitre M, Miao X, Gila B, Appleton BR, Hebard AF (2012) Rectification at graphene-semiconductor interfaces: zero-gap semiconductor-based diodes. *Phys Rev X* 2:011002
- Varghese SS, Lonkar S, Singh KK, Swaminathan S, Abdala A (2015) Recent advances in graphene based gas sensors. *Sens Actuators B* 218:160–183
- Vicarelli L, Vitiello MS, Coquillat D, Lombardo A, Ferrari AC, Knap W, Polini M, Pellegrini V, Tredicucci A (2012) Graphene field-effect transistors as room-temperature terahertz detectors. *Nat Mater* 11:865–871
- Vincenzi G, Deligeorgis G, Coccetti F, Dragoman M, Pierantoni L, Mencarelli D, Plana R (2012) Extending ballistic graphene FET lumped element models to diffusive devices. *Solid-State Electron* 76:8–12
- Wang Y, Wong D, Shytov AV, Brar VW, Choi S, Wu Q, Tsai H-Z, Regan W, Zettl A, Kawakami RK, Louie SG, Levitov LS, Crommie MF (2013) Observing atomic collapse resonances in artificial nuclei on graphene. *Science* 340:734–737
- Wei Z-J, Fu Y-Y, Liu J-B, Wang Z-D, Jia Y-H, Guo J, Ren L-M, Chen Y-F, Zhang H, Huang R, Zhang X (2014) Radio-frequency transistors from millimeter-scale graphene domains. *Chin Phys B* 23:117201
- Wen Q-Y, Tian W, Mao Q, Chen Z, Liu W-W, Yang Q-H, Sanderson M, Zhang H-W (2014) Graphene based all-optical spatial terahertz modulator. *Sci Rep* 4:7409
- Westlund A, Winters M, Ivanov IG, Hassan JU, Nilsson P-Å, Janzén E, Rorsman N, Grahn J (2015) Graphene self-switching diodes as zero-bias microwave detectors. *Appl Phys Lett* 106:093116
- Whitener KE Jr, Sheehan PE (2014) Graphene synthesis. *Diam Relat Mater* 46:25–34
- Wilmart Q, Berrada S, Torrin D, Nguyen VH, Fève G, Berroir J-M, Dollfus P, Plaçais B (2014) A Klein-tunneling transistor with ballistic graphene. *2D Mater* 1:011006
- Wu L, Chu HS, Koh S, Li EP (2010a) Highly sensitive graphene biosensors based on surface plasmon resonance. *Opt Express* 14:14395–14400
- Wu YH, Yu T, Shen ZX (2010b) Two-dimensional carbon nanostructures: fundamental properties, synthesis, characterization and potential applications. *J Appl Phys* 108:071301
- Xie B, Yang C, Zhang Z, Zou P, Lin Z, Shi G, Yang Q, Kang F, Wong C-P (2015) Shape-tailored graphene-based ultra-high-rate supercapacitor for wearable electronics. *ACS Nano* 9:5636–5645
- Xu H, Zhang Z, Wang Z, Wang S, Liang X, Peng L-M (2011) Quantum capacitance limited vertical scaling of graphene field-effect transistor. *ACS Nano* 5:2340–2347
- Xu H, Das S, Gong Y, Liu Q, Chien H-C, Chiu H-Y, Wu J, Hui R (2015) Complex refractive index tunability of graphene at 1550 nm wavelength. *Appl Phys Lett* 106:031109
- Yasaei P, Kumar B, Hantehzadeh R, Kayyalha M, Baskin A, Repnin N, Wang C, Klie RF, Chen YP, Král P, Salehi-Khojin A (2014) Chemical sensing with switchable transport channels in graphene grain boundaries. *Nat Commun* 5:4911
- Yao Y, Shankar R, Rauter P, Song Y, Kong J, Loncar M, Capasso F (2014) High-responsivity mid-infrared graphene detectors with antenna-enhanced photocarrier generation and collection. *Nano Lett* 14:3749–3754
- Yavari F, Koratkar N (2012) Graphene-based chemical sensors. *J Phys Chem Letter* 3:1746–1753
- Yeh C-H, Lain Y-W, Chiu Y-C, Liao C-H, Moyano DR, Hsu SSH, Chiu P-W (2014) Gigahertz flexible graphene transistors for microwave integrated circuits. *ACS Nano* 8:7663–7670
- Young AF, Kim P (2009) Quantum interference and Klein tunneling in graphene heterojunctions. *Nat Phys* 5:222–226
- Youngblood N, Anugrah Y, Ma R, Koester SJ, Li M (2014) Multifunctional graphene optical modular and photodetector integrated on silicon waveguides. *Nano Lett* 14:2741–2746
- Zagorodko O, Spadavecchia J, Serrano AY, Larroulet I, Pesquera A, Zurutuza A, Boukherroub R, Szunerits S (2014) Highly sensitive detection of DNA hybridization on commercialized graphene-coated surface plasmon resonance interfaces. *Anal Chem* 86:11211–11216

- Zak A, Andersson MA, Bauer M, Matukas J, Lisauskas A, Roskos HG, Stake J (2014) Antenna-integrated 0.6 THz FET direct detectors based on CVD graphene. *Nano Lett* 14:5834–5838
- Zhang Y, Liu T, Meng B, Li X, Liang G, Hu X, Wang QJ (2013) Broadband high photoresponse from pure monolayer graphene photodetector. *Nat Commun* 4:1811
- Zhao J, Zhang G-Y, Shi D-X (2013) Review of graphene-based strain sensors. *Chin Phys B* 522:057701
- Zheng Q, Kim J-K (2015) *Graphene for transparent conductors*. Springer, New York
- Zhu S-E, Ghatkesar MK, Zhang C, Janssen GCAM (2013a) Graphene based piezoresistive pressure sensor. *Appl Phys Lett* 102:161904
- Zhu Z, Joshi S, Grover S, Moddel G (2013b) Graphene geometric diodes for terahertz rectennas. *J Phys D* 46:185101
- Zubarev A, Dragoman D (2012) Tunable energy filtering of ballistic electrons in graphene. *J Phys D* 45:075301
- Zurutuza A, Marinelli C (2014) Challenges and opportunities in graphene commercialization. *Nat Nanotechnol* 9:730–734
- Zwolak M, Di Ventra M (2008) Physical approaches to DNA sequencing and detection. *Rev Mod Phys* 80:141–165

2D Nanoelectronics

Physics and Devices of Atomically Thin Materials

Dragoman, M.; Dragoman, D.

2017, XII, 199 p. 220 illus., 131 illus. in color.,

Hardcover

ISBN: 978-3-319-48435-8